JOURNAL OF GEOPHYSICAL RESEARCH, VOL. 105, NO. B6, PAGES 13,303–13,338, JUNE 10, 2000

Exhumation of the ultrahigh-pressure continental crust in east central China: Cretaceous and Cenozoic unroofing and the Tan-Lu fault

Lothar Ratschbacher,[1,2] Bradley R. Hacker,[3] Laura E. Webb,[4,5]
Michael McWilliams,[4] Trevor Ireland,[4] Shuwen Dong,[6]
Andrew Calvert,[3] Daniel Chateigner,[7,8]
and Hans-Rudolf Wenk [7]

Abstract. The orogenic architecture of the world's largest ultrahigh-pressure exposure, the Hong'an-Dabie Mountains of the Triassic Qinling-Dabie orogenic belt, is dominated by Cretaceous and Cenozoic structures that contributed to its exhumation from ≤30 km depth. Cretaceous magmatic crustal recycling (≥50% for the entire Dabie) and heating (>250° to >700°C) were most prominent in Dabie, and exhumation, magmatism, and cooling were all controlled by Cretaceous transtension. Exhumation was accomplished principally by an asymmetric Cordilleran-type extensional complex in the northern Dabie (Northern Orthogneiss unit) between 140 and 120 Ma, at rates as fast as 2 mm/yr and average horizontal stretching rates of up to 6 mm/yr. Cretaceous reactivation occurred within a regional transtensional strain field as a result of far-field collisions and Pacific subduction. The onset of crustal extension was preceded and possibly facilitated by a reheating of the Hong'an-Dabie crust (~140 Ma) coeval with the onset of voluminous magmatism in eastern China (~145 Ma), which resulted from a change in Pacific subduction from highly oblique to orthogonal. The Tan-Lu continental-scale fault was a normal fault zone in the mid-Cretaceous (~110-90 Ma) and underwent ≥5.4 km dip slip and ≥4 km throw in the Cenozoic. During the India-Asia collision the Qinling-Dabie belt acted as the structural discontinuity between the strike-slip-dominated escape tectonics south of the Qilian-Qinling-Dabie belt and the rifting-dominated tectonism north of it. The most prominent Cretaceous and Cenozoic structures of the Hong'an-Dabie, the Xiaotian-Mozitang and the Jinzhai fault zones, respectively, reactivated major lithospheric structures of the Triassic orogen, i.e., the Huwan detachment zone and the suture.

1. Introduction

The Hong'an-Dabie Shan ultrahigh-pressure (UHP) area is part of the 2000 km long Qinling-Dabie orogen and formed by attempted subduction of the Yangtze (or South China) craton beneath the Sino-Korean (or North China) craton in the Triassic (Figure 1) [e.g., *Hacker et al.*, 1996; *Ames et al.*, 1996; *Rowley et al.*, 1997]. The orogen comprises a penetratively deformed gneissic core and is subdivided from south to north into the Yangtze foreland fold-and-thrust belt, the blueschist, high-pressure amphibolite, quartz eclogite, coesite eclogite, and "Northern Orthogneiss" units, the Luzhenguang and Foziling "Groups" in the Dabie Shan, and additionally a variety of groups of proven or presumed Paleozoic and Proterozoic age along the northern rim of the Hong'an and Tongbai Shan (see *Hacker et al.* [1996] for a review and a discussion of stratigraphy and age data, Figure 1). At its margins the orogen is covered by Late Jurassic and younger volcanosedimentary strata. The blueschist through eclogite units constitute a prograde metamorphic sequence, with the diamond- and coesite-bearing eclogites and paragneisses indicating subduction of continental crust to >120 km [e.g., *Okay*, 1993; *Liou et al.*, 1996]. *Webb et al.* [1996], *Rowley and Xue* [1996], and *Hacker et al.* [1998, this issue] interpreted these units as a subducted slab exhumed by vertical extrusion (tectonic denudation) and contemporaneous erosion in Triassic-Early Jurassic time.

Cretaceous igneous rocks comprise 47% of the surface exposure of the Dabie Mountains (digitized from 1:500,000 geological maps, Figure 1), and almost the entire northern Dabie consists of Cretaceous igneous rocks and orthogneisses (*Hacker et al.* [1998] and section 3.), constituting the "Northern Orthogneiss unit" (NOU; Figure 1; *Hacker et al.* [1995]). The Cretaceous igneous signature diminishes westward into the Hong'an Shan, where Cretaceous igneous rocks are concentrated along the northern boundary (20% of surface exposure; Figure 1). The ubiquitous Cretaceous magmatic and metamorphic overprint (also see section 3.), i.e., the widespread outcrop of Cretaceous igneous rocks and gneisses, implies a considerable role of Cretaceous unroofing in the exhumation of the Hong'an-Dabie UHP rocks. In particular, it bears on the potential preservation of the lithospheric structure of the Triassic UHP orogen.

[1]Institut für Geologie, Universität Würzburg, Würzburg, Germany.
[2]Now at Institut für Geologie, Technische Universität Bergakademie Freiberg, Freiberg, Germany.
[3]Department of Geology, University of California, Santa Barbara.
[4]Department of Geology and Environmental Sciences, Stanford University, Stanford, California.
[5]Now at Department of Mineralogy, University of Geneva, Geneva, Switzerland.
[6]Chinese Academy of Geological Sciences, Beijing
[7]Department of Geology, University of California, Berkeley.
[8]Now at Laboratoire de Physique de l'Etat Condensé, Université du Maine, Le Mans, France.

Copyright 2000 by the American Geophysical Union.

Paper number 2000JB900040.
0148-0227/00/2000JB900040$09.00

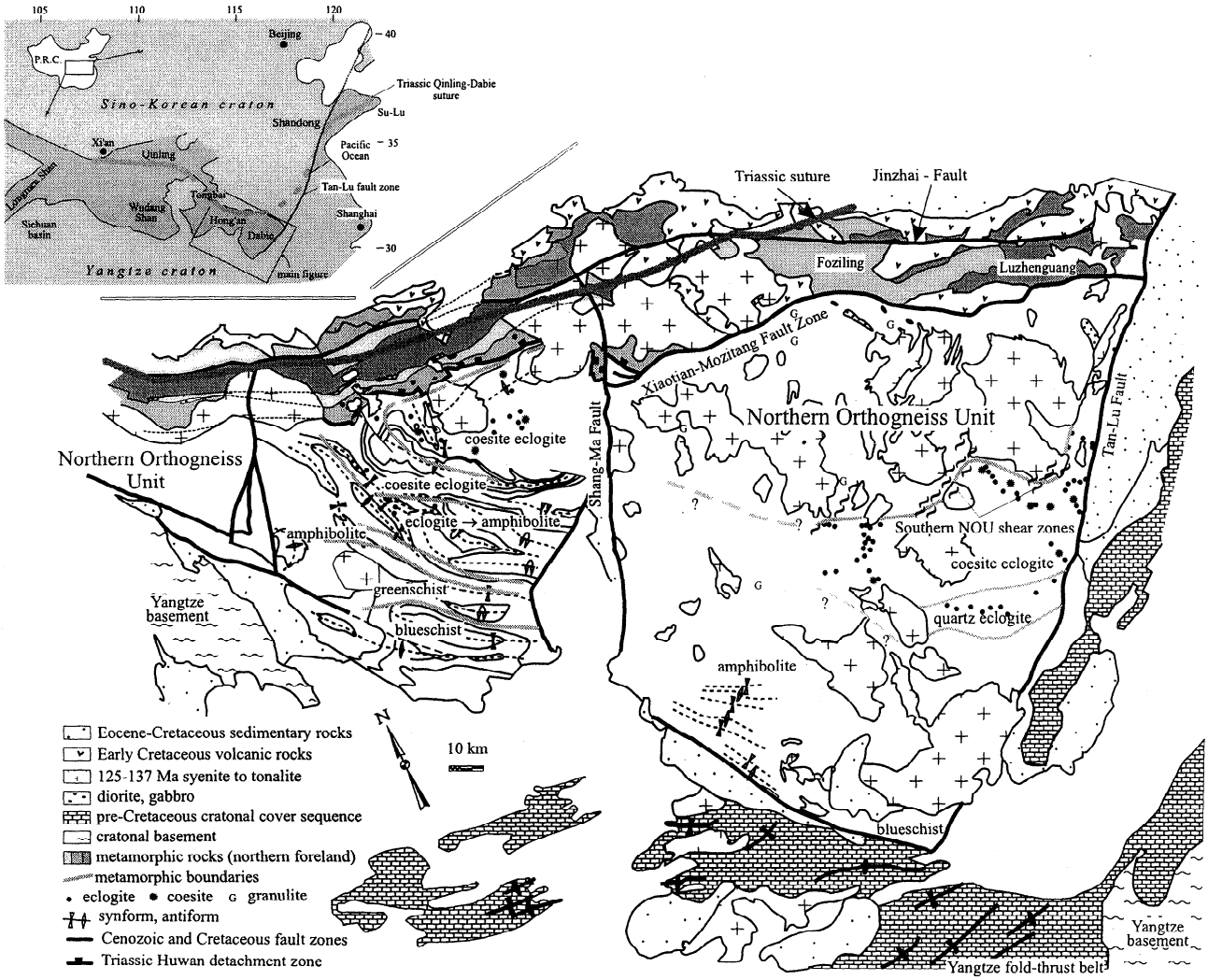

Figure 1. Dabie Shan and Hong'an areas, drawn from *Regional Geological Survey of Anhui* [1987], *Regional Geological Survey of Henan* [1989], *Regional Geological Survey of Hubei* [1990], *Okay et al.* [1993], and *Hacker et al.* [1995, 1996, 1998]. Location of major faults and units discussed in text are shown. Inset shows the Triassic collisional orogen in central China. NOU, Northern Orthogneiss unit.

The NOU is an asymmetric magmatic-structural dome that formed during Cretaceous NW–SE subhorizontal extension (*Hacker et al.* [1995] and see section 4.), overprinting a Triassic(?) granulite facies basement sequence [*Li et al.*, 1989, 1993; *Zhang et al.*, 1996; *Jahn et al.*, 1999]. Although apparently concentrated in the Dabie Mountains, Cretaceous extension and magmatism were widespread throughout eastern China [e.g., *Davis et al.*, 1996; *Yin and Nie*, 1996; *Faure et al.*, 1996] and are traditionally associated with the Yinshanian orogeny [e.g., *Yang et al.*, 1986]. The plate tectonic setting of this distributed and long-lasting event has been ascribed to Pacific subduction [e.g., *Yin and Nie*, 1996], although magmatism reached >1000 km into the continental interior and the structural evolution encompassed both contractional and extensional periods. A modern geodynamic understanding clearly requires more regional, geochronologic, and kinematic studies of the deformation field [e.g., *Davis et al.*, 1996].

The Cenozoic evolution of eastern Asia has been interpreted as the result of the combined effects of the India-Asia collision and Pacific subduction [e.g., *Molnar and Tapponnier*, 1975]. *Peltzer et al.* [1985] and *Zhang et al.* [1995] documented cumulative sinistral slip rates of 7.2 ± 2.2 mm/yr for active faulting in the Qinling-Dabie orogen and speculated that several tens of kilometers of post-Eocene sinistral displacement occurred along the northern margin of the mountain belt.

The Tan-Lu fault in eastern China is considered to be one of the largest continental faults and has been assigned key significance in several tectonic models of eastern Asia. *Yin and Nie* [1993], for example, predicted that the Tan-Lu accommodated ~500 km of sinistral strike-slip faulting in the Triassic during postulated north directed indentation of South China into North China in the Shandong region of northeastern China. Dating motion along the Tan-Lu has been difficult, and there are Proterozoic ages for ductilely deformed gneisses and mylonites (2.3-0.5 Ga, Shandong province [*Fletcher et al.*, 1995]), Cretaceous ages for fault gouge (90-110 Ma, Shandong province [*Chen et al.*, 1989]), and late Cenozoic ages for dextral, transtensional faulting (active faulting, Anhui province [*Zhang et al.*, 1995]; Shandong

province [*Lin et al.*, 1998]). Subsidence analysis in the Yitong graben, northeastern China, documents twofold transtensional activity in the Paleocene and Oligocene [*Lu et al.*, 2000].

This paper summarizes new and published structural/ geochronologic/petrologic data to address the contribution of late Mesozoic and Cenozoic tectonics to the exhumation of the UHP-HP complex in the Hong'an-Dabie section of the Triassic-Jurassic Qinling-Dabie orogen and to tie these reactivations into the geodynamic assembly of eastern Asia. In particular, we address the following questions: (1) What are the degree, extent, age, and kinematics of the reactivations of the Qinling-Dabie belt? (2) What is the proportion of Cretaceous plutons (undeformed rocks) and orthogneisses (deformed rocks), i.e., the Cretaceous magmatic crustal recycling of pre-Cretaceous rocks, in the Hong'an-Dabie section? (3) What are the intrusion depths of these Cretaceous igneous rocks, as they quantify the extent of Cretaceous exhumation? (4) What is the age range of the igneous rocks, and when have they been deformed? (5) What is the Northern Orthogneiss unit, and how does it relate to other Cretaceous contractional and extensional deformation of the Yinshanian orogeny in eastern China? (6) What is the age of movement on the Tan-Lu fault, what are its kinematics, and how is it related to the deformation and magmatism in the Hong'an-Dabie area?

This paper documents the Cretaceous and Cenozoic overprint that dominates the orogenic architecture of the world's largest exposure of UHP rocks and shows that exhumation from midcrustal depth occurred between 140 and 120 Ma. It concentrates on the Dabie Shan, showing that exhumation was accomplished principally by a Cordilleran-type extensional complex within a regional transtensional strain field and as a result of far-field collisions and Pacific subduction. The paper is a companion to a synthesis of the Triassic exhumation of the Hong'an-Dabie area [*Hacker et al.*, this issue] and incorporates results from studies in the Hong'an area [*Webb et al.*, 1999a; 2000].

2. Cenozoic Faulting in the Hong'an-Dabie Mountains

The Qinling-Dabie orogen is sliced by several WNW trending, >100 km long faults. The active Qinling fault system is the eastward extension of the Haiyuan and Kunlun fault systems (Figure 2a) and is interpreted to accommodate the eastward escape of the Yangtze block caused by the India-Asia collision [*Tapponnier and Molnar*, 1977]. The onset of sinistral displacement is poorly constrained; it is thought to be Pliocene by *Bellier et al.* [1991], but the Eocene basins lined up along the Qinling fault system point to significant early Tertiary activity [e.g., *Peltzer et al.*, 1985]. Although to a first approximation the existence, sense, and slip rates of the Quaternary strike-slip faults along the Qinling-Dabie have been established [*Peltzer et al.*, 1985; *Zhang et al.*, 1995], much is unknown about the regional distribution of Tertiary and Quaternary faulting and the associated regional stress fields. In the course of our fieldwork on the Mesozoic orogeny, we collected microtectonic data to determine the extent to which the Triassic orogenic architecture was reactivated during the Cenozoic. Our study builds on the fieldwork and satellite image interpretation of *Zhang et al.* [1995].

On the basis of historical seismicity several of the NE and WNW trending faults slicing the Hong'an-Dabie are active (Figure 2b; *Ma* [1986]). On the basis of geomorphologic features, historic seismicity in the vicinity of faults traceable in the field, and, in particular, traces of zones of weakly consolidated cataclastic rocks affecting Cretaceous and Cenozoic rocks, the Cenozoic deformation is partitioned into three major fault zones: (1) the Jinzhai fault zone (also Jinzhai-Guishan or Jin-Gui fault in the Chinese literature), crossing the northern margin of the Hong'an and Dabie Mountains (Figures 2b-2e); (2) the Tan-Lu fault zone, terminating the Dabie Shan at its eastern edge (Figures 2b-2d); and (3) a little-studied fault zone in the southern Tongbai and Hong'an Mountains (Figure 2e). On the basis of observations from 36 stations, we obtained regionally consistent stress trajectories (Figure 2b) and calculated a 134° ± 34° trend for σ_3 for the major Cenozoic deformation (34 stations); this stress field overprinted an older, also Cenozoic field in which σ_3 trends 070° ± 28° (8 stations; Figure 2b and Table 1).

On the basis of piercing points identifiable on the 1:500,000 Chinese province maps [*Regional Geological Survey of Henan* (R.G.S. Henan), 1989] (e.g., offsets in Cretaceous plutonic and Late Jurassic–Early Cretaceous volcanic rocks, Figure 2c), cumulative horizontal displacement along the Jinzhai fault in the northwestern Dabie does not exceed 5 km. Offset seems to die out in the eastern Dabie, where no large offsets are apparent and the Jinzhai fault apparently terminates against a strand of the Tan-Lu fault zone. The fault pattern at the eastern termination of the Jinzhan fault is complex (Figure 2c, D216-D217), indicating either local block rotations or a variable stress field. Overall, the Jinzhai fault is a strike-slip fault with an average angle of 31° between σ_1 and the trend of the fault.

The Tan-Lu fault zone constitutes a set of subparallel fault strands with a morphologically well-expressed segment at the eastern edge of the northern and central Dabie (Figures 2c and 2d). South of the Yangtze river one Tan-Lu-parallel fault forms the morphologically pronounced boundary of the Lushan basement complex (Figure 2d). At the eastern edge of Dabie, thick cataclasite marks the fault in both crystalline basement and Tertiary strata. Although the mesoscale fault data are complex (Figures 2c and 2d), the studied segments overall depict an early, probably Tertiary, transpression (e.g., D78-1) and thereafter evolved from dextral transtension to normal. In contrast to the apparent termination of the Jinzhai fault against the Tan-Lu fault at mapscale, left-lateral faulting along about NW trending, cataclastic faults was found throughout the northeastern foreland of the Dabie Mountains (e.g. D200-D201, Figure 2d, *Schmid et al.* [2000]).

Overall, the Tan-Lu fault in eastern Dabie is a normal fault with an average of 90° between σ_3 and the fault trend. Conjugate mesoscale strike-slip faults at several stations indicate a component of NE-SW contraction coeval with half-graben formation east of the Dabie. NE trending, mostly normal faults record weak, distributed deformation across most of the Hong'an and Dabie Mountains; although this deformation constitutes the relatively youngest faulting, no absolute age criteria exist.

Chinese maps (e.g., 1:200,000; *Regional Geological Survey of Anhui* (R.G.S. Anhui) [1975]) depict thicknesses of up to 4.8 km, uniformly 8°-33° NW dipping, mostly Quaternary covered, Eocene sediments east of Dabie. A minimum extension of 18% (≥5.4 km dip slip along and ≥4 km throw across the Tan-Lu) across the Cenozoic foreland basin east of the Dabie is obtained employing the model of rotating planar normal faults. Calculation parameters are (1) a 50° dip for the morphologically

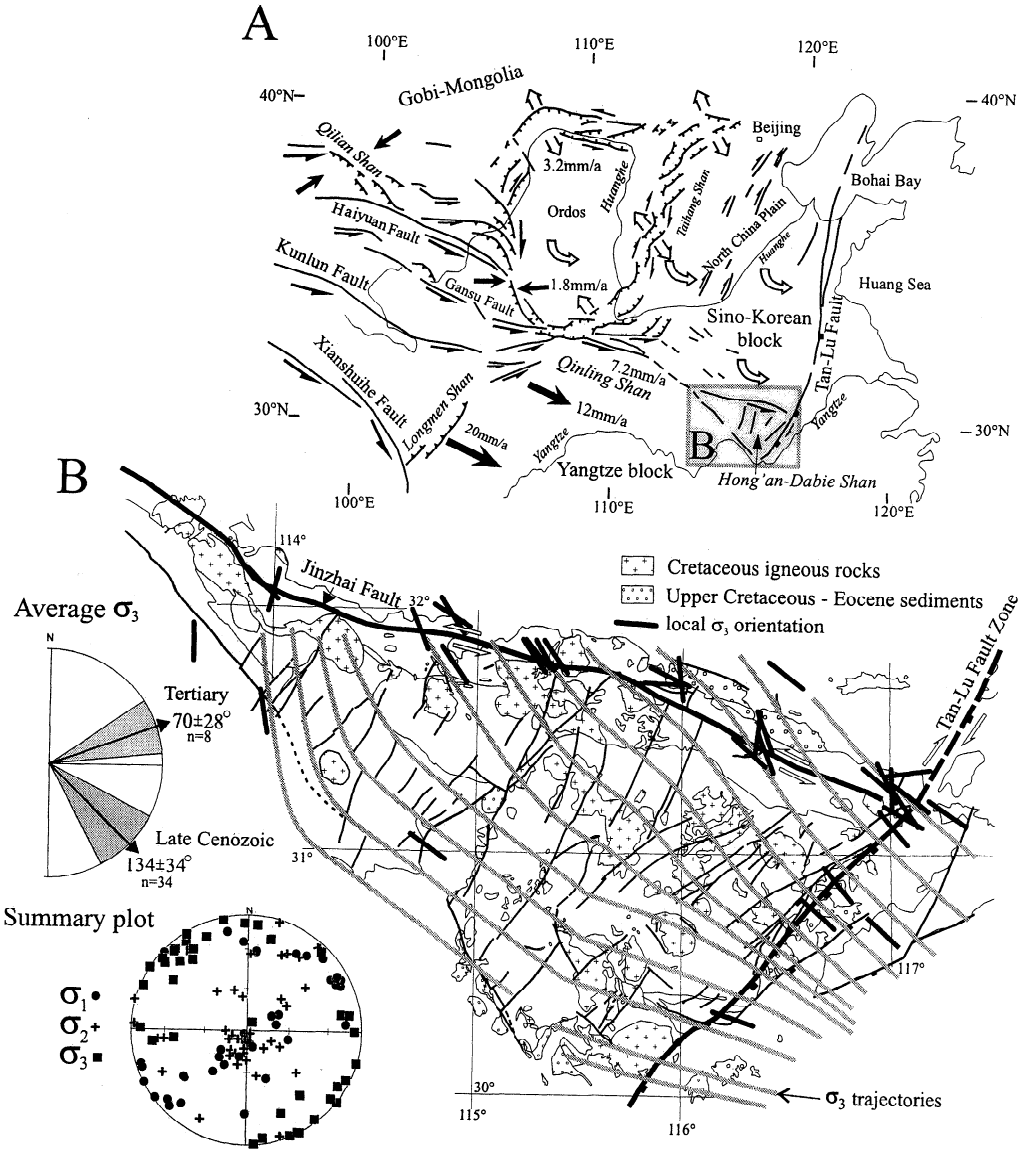

Figure 2. (a) Simplified map of late Cenozoic extensional and strike-slip tectonics in north and central China, modified from *Zhang et al.* [1995, and references therein]. (b) The σ_3 trajectories of late Cenozoic strike slip–extensional deformation are superimposed on a neotectonic fault map of the Hong'an-Dabie Mountains; trajectories are calculated based on the results of local stress orientation determinations. Bars show data used for trajectory calculation (a few data are off the southern and northeastern margin of Figure 2b and are not shown, but used for calculation). Inset, upper left, suggests separation into two distinct stress fields, based on consistent overprinting criteria and neotectonic features associated with the "late Cenozoic" fault sets. Lower hemisphere, equal-area stereogram, lower left, summarizes principal stress orientations attributed to Cenozoic deformation. (c) Fault slip data and principal stress orientations 1-3 plotted around simplified geological map of the northern Dabie showing active faulting along the easternmost Jinzhai fault and a portion of the Tan-Lu fault zone. Stereograms (lower hemisphere, equal-area stereograms) are as follows: Faults are drawn as great circles and striae are drawn as arrows pointing in the direction of displacement of the hanging wall. Confidence level of slip sense determination is expressed in the arrow head style: solid, certain; open, reliable; half, unreliable; without head, very poor. Station 23M is from *Zhang et al.* [1995]. Double-headed arrows and attached numbers give location and amount of offset of Jurassic and Cretaceous lithological markers (estimated from *R.G.S. Hubai* [1990]). Station D516t is located north of the map area. (d) As in Figure 2c, but showing the southeastern section of the Tan-Lu fault zone. (e) As in Figure 2c but showing the Tongbai-Hong'an Mountains and active (solid lines) and possibly active faults (dashed lines). (f) NW-SE cross section (line A-B in Figure 2d) interpreted from *R.G.S. Anhui* [1975], our own field data, and calculation of minimum slip along the Tan-Lu.

spectacular Tan-Lu master normal fault east of the Dabie, constrained by the average dip of the mesoscale normal faults measured in outcrops (e.g., D77-D78) and a shallow (~0.8 km) tomographic profile across the Tan-Lu [*Oberhänsli et al.*, 1998], and (2) a 15° average dip of the Eocene sediments east of the Dabie (Figure 2f).

The apparent eastward decrease in the amount of displacement and the termination of the Jinzhai fault as a distinct morphologic feature suggests that the strike slip is taken up by another faulting mode and that the kinematics of the Tan-Lu fault changes at the intersection of the two faults. NE trending faults that parallel the Tan-Lu, particularly in the Dabie Shan (see Figure 2b and *Zhang*

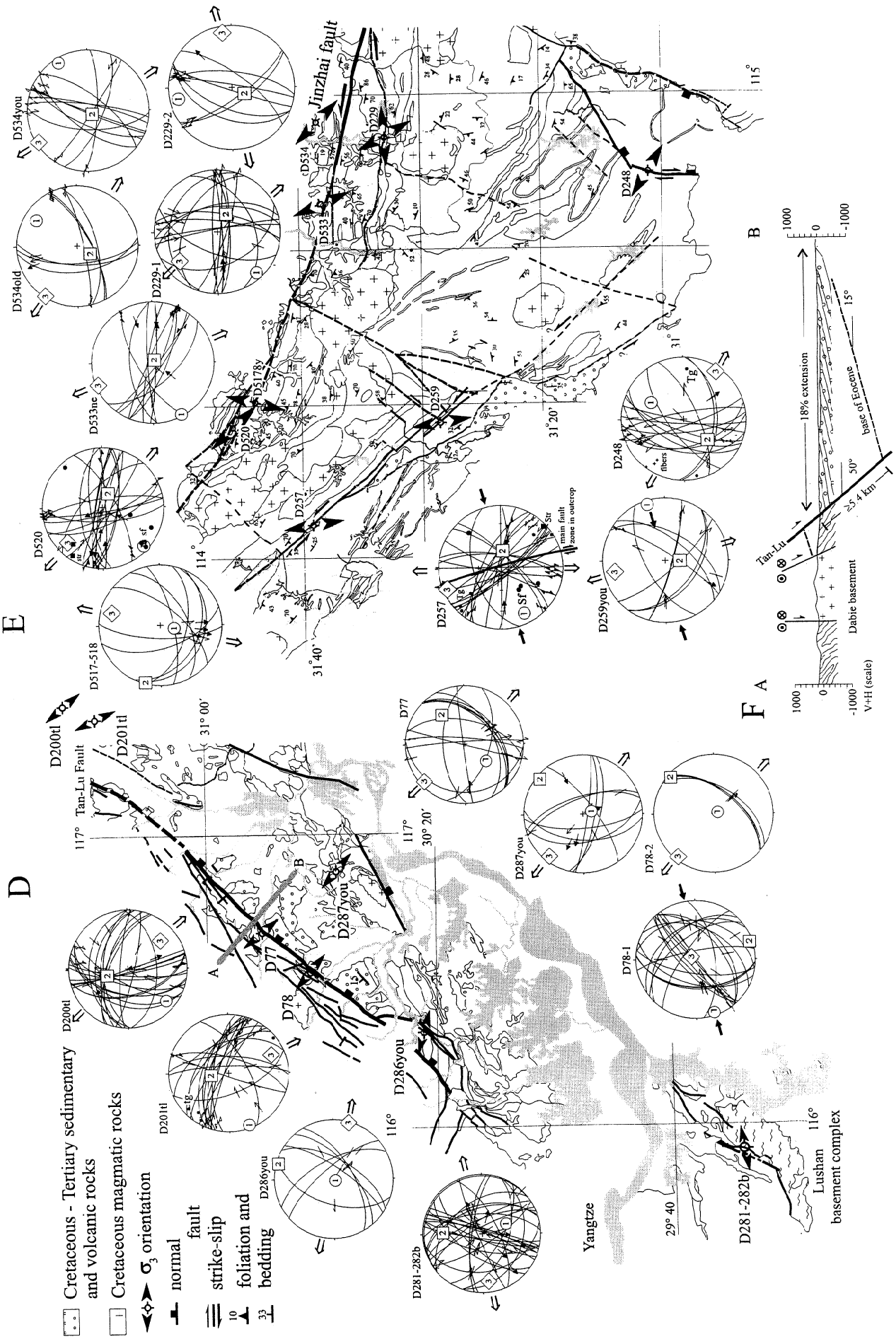

Figure 2. (continued)

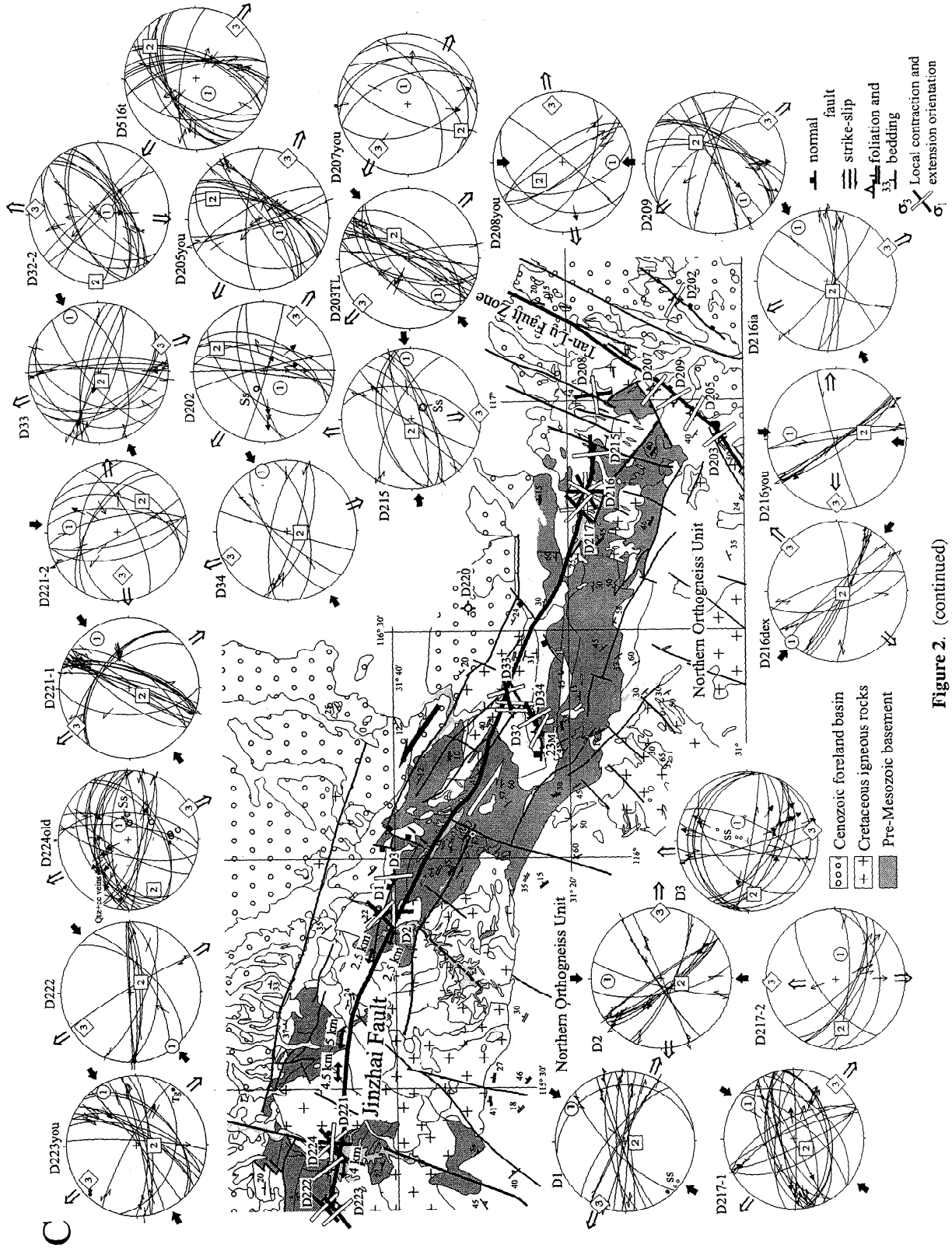

Figure 2. (continued)

Table 1. Location of Stations and Parameters of the Deviatoric Stress Tensor: Cenozoic Stress Field

Site	Lithology	Latitude	Longitude	Method	n	σ_1	σ_2	σ_3	F	R
D1	conglomerates (K)	37° 25.61'	122° 10.52'	P-B-T	13 13	046 10	190 77	293 03		
D2*	volcanics (J?)	37° 25.58'	122° 10.5'	NDA	15 15	357 24	195 65	090 07	17°	0.5
D3	Maishan quartzite (pre-K)	31° 39.93'	115° 57.93'	P-B-T	20 20	063 65	264 24	171 06		
D32-2*	red beds (K)	31° 24.57'	116° 21.22'	grid	17 16	166 80	273 03	005 09	20°	0.4
D33	volcanics, conglomerate	31° 26.4'	116° 23.23'	P-B-T	18 18	064 11	250 79	157 01		
D34	red beds (K)	31° 23.67'	116° 19.58'	NDA	9 9	061 08	188 74	336 13	14°	0.6
D77	paragneiss (pre-K)	30° 49.72'	116° 39.47'	NDA	13 13	219 52	053 37	318 07	15°	0.8
D78-1	conglomerate (E)	30°43.77'	116° 34.78'	grid	21 19	252 05	162 04	031 83	14°	0.3
D78-2				P-B-T	4 4	177 83	041 05	310 05		
D200tl	orthogneiss (K)	31° 47.69'	117° 33.27'	P-B-T	25 25	221 16	342 60	140 28		
D201tl	orthogneiss (K)†	31° 28.4'	117° 22.69'	NDA	22 21	250 05	352 66	157 23	19°	0.3
D202	red beds (K)	31° 07.59'	117° 12.84'	NDA	12 11	226 63	027 26	121 08	14°	0.6
D203TL	orthogneiss (K)	31° 03.43'	116° 56.21'	P-B-T	17 17	232 33	058 57	317 08		
D205you	granitoid (K)	31° 0.79'	116° 57.51'	NDA	17 17	213 61	024 29	116 04	23°	0.9
D207you	syenite (K)	31° 09.44'	117° 00.86'	P-B-T	8 8	078 69	207 14	304 24		
D208you*	volcanics	31° 16.25'	117° 00.39'	NDA	8 8	181 28	322 55	080 18	11°	0.5
D209	granitoid (K)	31° 08.46'	117° 00.51'	NDA	14 13	233 33	047 57	142 03	13°	0.7
D215	volcanics (J?)	31° 17.25'	116° 52.33'	NDA	11 11	086 15	269 75	176 01	12°	0.6
D216dex	volcanics (K)‡	31° 17.75'	116° 48.19'	NDA	10 10	313 02	208 83	043 07	12°	0.6
D216you*				NDA	10 10	006 32	168 57	271 09	15°	0.5
D216ia*				NDA	7 6	062 14	243 76	152 00	10°	0.5
D217-1	volcanics (J?)	31° 18.49'	116° 46.65'	NDA	23 22	038 18	219 72	128 00	24°	0.9
D217-2				NDA	8 8	102 60	264 29	358 08	19°	0.5
D221-1	granitoid (K)†	31° 47.83'	115° 21.22'	NDA	21 20	058 16	209 72	325 08	15°	0.4
D221-2*				P-T	11 11	006 31	130 43	264 37		
D222	Maishan metamorphics	31° 48.45'	115° 15.15'	NDA	10 09	233 02	136 73	324 17	16°	0.7
D223you	granitoid (K)	31° 47.33'	115° 14.84'	NDA	17 17	059 11	181 69	326 17	17°	0.6
D224	Maishan metamorphics	31° 48.17'	115° 18.05'	NDA	22 21	059 70	243 20	153 01	24°	0.9
D229-1	volcanics (K?)	31° 46.65'	114° 53.53'	P-B-T	18 17	228 10	116 64	322 24		
D229-2*				NDA	8 8	348 14	207 72	081 11	12°	0.5
D248	red beds (K+Ter?)	31° 02.99'	114° 44.68'	NDA	16 16	028 41	222 48	124 07	16°	0.7
D257	red beds (K+Ter?)	31° 58.12'	113° 36.52'	P-B-T	22 22	254 21	098 67	358 04		
D259you	blueschist-marble (pre-K)	31° 36.59'	113° 57.08'	P-B-T	9 9	073 06	180 71	348 18		
D281-282b*	limestone	29° 27.41'	115° 52.84'	P-B-T	29 27	158 53	002 34	263 19		
D286you	basement (pre-K)	30° 22.38'	116° 18.63'	NDA	7 7	220 87	016 03	106 01	16°	0.5
D287you	basement (pre-K)	30° 37.36'	117° 51.72'	P-B-T	9 9	161 78	040 06	309 09		
D516t	volcanic agglomerate (K)	31° 43.14'	116° 30.58'	NDA	19 18	231 68	036 22	128 05	19°	0.6
D5178y	marble (pre-K)	32° 07.46'	114° 00.30'	NDA	8 8	193 71	285 01	015 19	9°	0.4
D520	greenschist (pre-K)	32° 11.70'	113° 55.80'	NDA	21 20	224 08	112 70	316 19	20°	0.3
D533ne	marble (pre-K)	31° 56.97'	114° 38.55'	P-B-T	12 12	242 02	123 86	348 03		
D534o	volcanics (J)	31° 57.23'	114° 55.03'	NDA	7 7	033 21	211 69	303 01	13°	0.5
D534y				NDA	11 11	059 08	219 82	328 03	10°	0.5

For methods used to calculate stress tensors, see appendix 2. P-B-T, pressure-tension method; NDA, numeric dynamic analysis technique; grid, grid search technique. In the measurement column, n, the first number is number of measurements, and the second number is number of measurements used for calculation. For σ_1-σ_3, azimuth (first number) and plunge (second number) of the principal stress axes are given. The stress ratio R is $(\sigma_2-\sigma_3)(\sigma_1-\sigma_3)^{-1}$ (where 1 is uniaxial confined extension and 0 is uniaxial confined compression). The fluctuation F gives the average angle between the measured slip and the orientation of the calculated theoretical shear stress. J, Jurassic; K, Cretaceous; E, Eocene; Ter, Tertiary.

*Possibly Tertiary stress field; the rest of the stations probably record late Cenozoic faulting.

†Radiometric dating available (see Table 2).

‡Unpublished K/Ar age of ~130 Ma, R.G.S. Hubei staff, personal communication.

et al. [1995]), are probably normal faults and suggest that sinistral faulting is taken up by wholesale NW-SE stretching within Dabie, along the Tan-Lu, and within the eastern Dabie foreland. Our mesoscale fault data north of the intersection of the Jinzhai and Tan-Lu faults record a more prominent strike-slip component, whereas pure normal faults seem to be confined to south of the intersection; this change in mesoscale fault kinematics coincides with a change in the fault character, with a morphologically well defined, single strand at the eastern edge of the basement rocks south of the intersection and shorter, more northerly trending, and morphologically less well expressed strands north of the intersection (Figures 2c and 2d). Altogether these features may indicate higher extension rates within the Dabie and its eastern foreland south of the Jinzhai fault than north of it.

The average NW-SE (134°) extension direction obtained for the Dabie area is similar to active NW-SE stretching imposed by the India-Asia collision onto Asian crust south of and along the major sinistral central Asian strike-slip faults (Altyn Tagh, Kunlun, and Qinling); it is grossly similar albeit more E-W than Cenozoic extension in northern China (≥140°, e.g., grabens along the northern margin of the Ordos block; *Zhang et al.* [1995, 1998]; Figure 2a). The documented faulting emphasizes the difference between strike-slip-dominated tectonics along the Qilian-Qinling-Dabie belt and dominant rifting north of it.

Cenozoic faulting is accompanied by cataclasis and/or

dilational, predominantly calcite veining indicative of low-temperature (low-T), upper crustal deformation. Taking the vertical throw on the Tan-Lu fault and the thickness of Tertiary sediments at the eastern edge of the Dabie as extreme values, Cenozoic denudation of the Dabie Shan amounted to ≤5 km.

3. Cretaceous Plutons and Orthogneisses in the Hong'an-Dabie Mountains: Distribution, Age, Cooling History, and Crystallization Depth

3.1. Distribution and Age

The Triassic UHP-HP units of Hong'an-Dabie comprise white-mica-rich paragneiss, containing blocks of eclogite, marble layers, hornblende-rich orthogneiss, and intermediate to acid meta-igneous rocks [*Liou et al.*, 1996; *Hacker et al.*, 1996]. These rocks are confined to the southern half of Dabie and to Hong'an. The UHP-HP rocks contrast with a rock assemblage in the northern half of Dabie and a similar unit in eastern Tongbai which so far has poorly defined boundaries (Figure 1). We have combined these rocks into the NOU [*Hacker et al.*, 1995] and characterize it by the following.

1. Rock assemblage. The NOU contains pyroxenite, gabbro, diorite, tonalite, trondhjemite, granodiorite, granite, syenite, and their deformed equivalents (orthogneisses); intermediate-composition rocks predominate over mafic and rare ultramafic rocks [e.g., *Jahn et al.*, 1999]. The massive migmatitic and magmatic rocks lack white mica. They intrude an ultramafic + mafic + carbonate basement sequence which comprises <5% of the NOU. Multiple intrusion sequences are common.

2. Structural setting. In Dabie the plutonic system of the NOU is delimited along its northern boundary by the Xiaotian-Mozitang fault (XMF, Figure 1); its southern boundary is a less well defined, deformed intrusive zone. There, rocks are commonly migmatitic, injected by multiple dike and stock sequences, and are overprinted by synmagmatic to postmagmatic normal shear. Penetrative deformation of the NOU was by subhorizontal extension and wrenching (*Hacker et al.* [1995] and section 4.).

3. Age. Undeformed igneous rocks of the NOU have zircon ages of 129.1 ± 2.6 to 125.6 ± 0.3 Ma (number of dates, n=3), and orthogneisses yielded slightly older zircon ages of 136.8 ± 5.1 to 128.2 ± 2.2 Ma (n=7, Figure 3a; *Hacker et al.* [1998], *Xue et al.* [1997], and *Zhang and Sun* [1990]). Cooling ages are Cretaceous as well. We dated four plutons and one orthogneiss of the NOU suite using the $^{40}Ar/^{39}Ar$ method on hornblende and biotite (Tables 2 and 3, Figures 3b and 4a; $^{40}Ar/^{39}Ar$ data are available from the World Wide Web server for the Department of Geology University of California, Santa Barbara, node http://www. geol.ucsb.edu/~hacker/suppleData/UHPCret). The ages range from 130 ± 3 to 120.5 ± 1.2 Ma. DS25, a common tonalitic orthogneiss, yielded a weighted mean hornblende age of 124 ± 1 Ma for the high-T degassing increments comprising most of the ^{39}Ar released. DS58, a partly mylonitized gabbro at the immediate footwall of the XMF near Mozitang, shows an internally discordant, humped-shaped spectrum for hornblende and a 120.5 ± 1.5 Ma plateau age for biotite; a subset of contiguous steps from the hornblende shows a well-fit inverse isochron with an $^{40}Ar/^{36}Ar$ intercept at 846 ± 2, indicating excess ^{40}Ar, and an age of 120.7 ± 1.2 Ma. DS72, the Yuexi tonalite, shows hornblende and biotite weighted mean ages of 130 ± 3 and 124 ± 2 Ma, respectively. DS81, a weakly deformed tonalite along the southern margin of the NOU, yielded a hornblende plateau age of 126.7 ± 1.2 Ma. Biotite from a granite near Shuihou (DS95), again from the southern edge of the NOU, has a plateau age of 126.4 ± 1.2 Ma. Published hornblende and biotite K/Ar and Ar/Ar ages (19 dates) cover 133 to 121 Ma (for regional distribution see *Hacker et al.* [1996, 1998] and *Hacker and Wang* [1995]). Late Proterozoic (~650-800 Ma) sensitive high-resolution ion microprobe (SHRIMP) zircon core and upper intercept thermal ionisation mass spectrometry (TIMS) ages indicate magma contamination by Yangtze craton crust [*Hacker et al.*, 1998; *Rowley et al.*, 1997; *Ames et al.*, 1996]. The 245-220 Ma Sm/Nd ages of the rare basement rocks record a relict Triassic metamorphism [*Li et al.*, 1993; *Okay et al.*, 1993] of probable UHP [*Tsai and Liou*, 2000]. *Jahn et al.* [1999], however, showed that some of these ages may have to be revised and that the majority of the ultramafic/mafic rocks were most probably emplaced over the same Early Cretaceous time period as the more felsic rocks. Negative $\varepsilon_{Nd}(T)$ values, unradiogenic feldspar Pb isotopic compositions, and a tight range of moderately radiogenic I_{Sr} values of the late Mesozoic igneous rocks (from ultramafic to granitic) from Dabie suggest that they are most likely derived by remelting of ancient lower continental, probably Yangtze crust [*Chen and Jahn*, 1998], or lower crustal contamination of a mantle melt [*Jahn et al.*, 1999].

4. Intrusion-deformation relationship. Orthogneisses, granitoids, and aplite dikes are widespread in the NOU, whereas migmatites are relatively rare despite frequent assertions to the contrary. Because of the intensity of gneissification, in particular along the XMF, it is difficult to unambiguously distinguish syntectonic from pretectonic intrusions. Figure 3c depicts schematically the metamorphism-intrusion-deformation relationships of the NOU. Plutons interpreted as syntectonic show one or several of the following criteria: (1) At outcrop scale, crystal-plastic structures at the pluton margin grade into hypersolidus

Figure 3. (a) Reliable Cretaceous U/Pb zircon and $^{40}Ar/^{39}Ar$ hornblende ages from orthogneisses and plutons of the Dabie-Hong'an-Tongbai area. Data are from *Hacker et al.* [1998], *Xue et al.* [1997], *Ames et al.* [1996], *Zhang and Sun* [1990], *Jahn et al.* [1999], and this study. b) Summary of new $^{40}Ar/^{39}Ar$ ages of the Dabie Shan. Ages are from this study (Tables 2 and 3) and those summarized by *Hacker et al.* [1998] and *Jahn et al.* [1999]. (c) Schematic metamorphism-intrusion-deformation relationship of the Northern Orthogneiss unit. (d) Intrusion depths and isobar contours of intermediate calc-alkaline plutons and orthogneisses of the Dabie Shan, calculated using the calibration of *Schmid* [1992] of the Al-in-hornblende geobarometer (Table 4 of this study and data of *Ma et al.* [2000]) combined with P estimates by *Zhang et al.* [1996] using the amphibole-plagioclase method of *Blundy and Holland* [1990]. Foliation trajectories are drawn after data from *R.G.S. Anhui* [1975, 1987] and *R.G.S. Hubei* [1990] and our own observations. Principal extension direction is from data summarized in Figure 6. (e) Cretaceous thermal evolution of the Dabie–Hong'an–Tongbai area. Each map shows a particular time slice and includes the raw U/Pb and Ar/Ar data, as well as isotherms that are drawn to represent roughly 600°C (between zircon and hornblende), 400°C (between hornblende and mica), 275°C (between mica and K-feldspar cooling), and 250°C (between K-feldspar cooling and K-feldspar reheating ages). For K-feldspars we show initial cooling to <275°C with a normal symbol, later reheating to 200°–250°C with solid circles, and K-feldspars below 200°C at a given time slice with open circles. Ages used are those of Figures 3a and 3b and of *Webb et al.* [1999a] and *Zhai et al.* [1998].

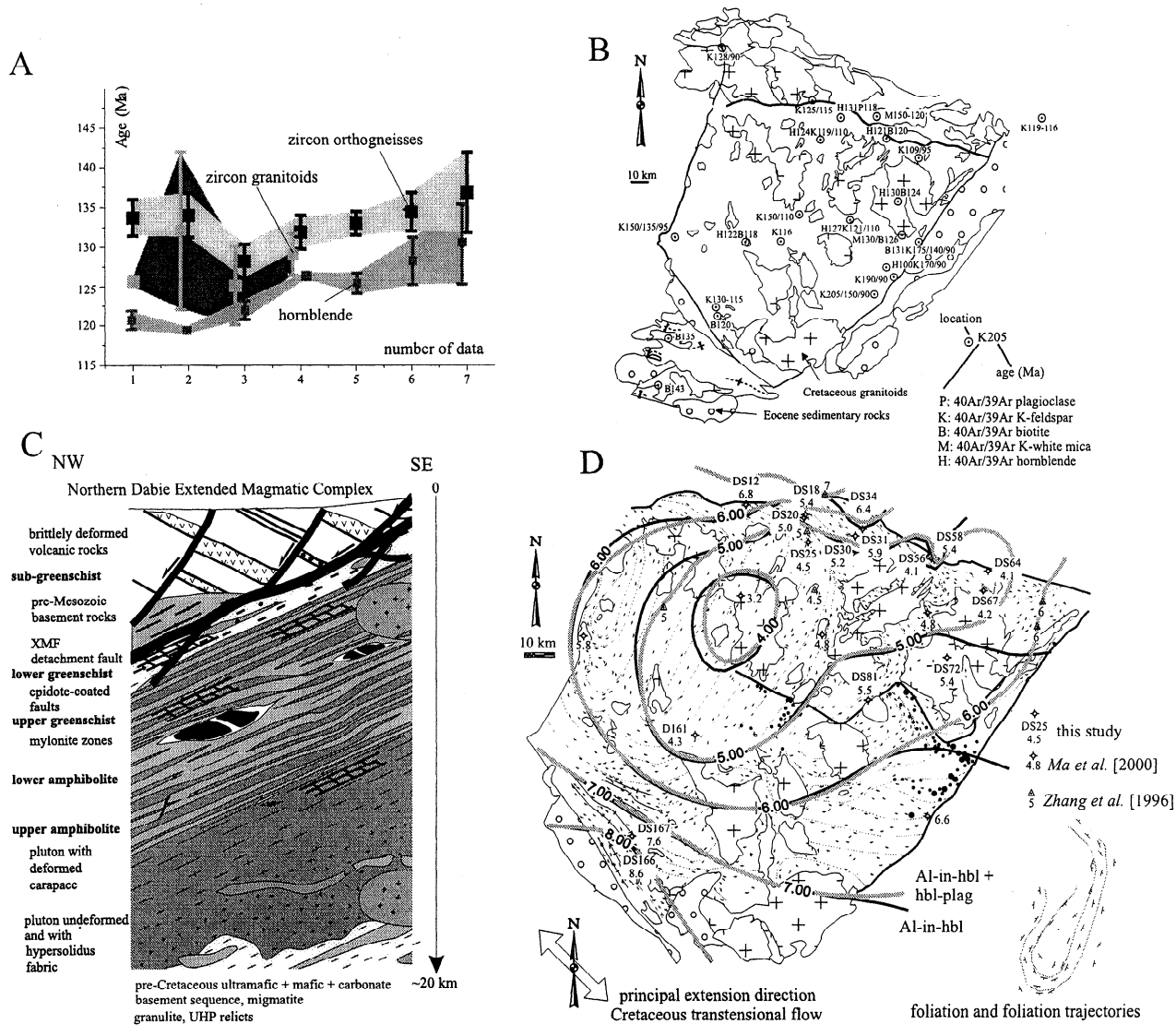
A
Age (Ma)
zircon orthogneisses
zircon granitoids
hornblende
number of data
B
N
10 km
location
K205
age (Ma)
Cretaceous granitoids
Eocene sedimentary rocks
P: 40Ar/39Ar plagioclase
K: 40Ar/39Ar K-feldspar
B: 40Ar/39Ar biotite
M: 40Ar/39Ar K-white mica
H: 40Ar/39Ar hornblende
C
NW
SE
Northern Dabie Extended Magmatic Complex
brittlely deformed volcanic rocks
sub-greenschist
pre-Mesozoic basement rocks
XMF detachment fault
lower greenschist
epidote-coated faults
upper greenschist
mylonite zones
lower amphibolite
upper amphibolite
pluton with deformed carapace
pluton undeformed and with hypersolidus fabric
~20 km
pre-Cretaceous ultramafic + mafic + carbonate basement sequence, migmatite granulite, UHP relicts
D
N
10 km
this study
Ma et al. [2000]
Zhang et al. [1996]
Al-in-hbl + hbl-plag
Al-in-hbl
principal extension direction
Cretaceous transtensional flow
foliation and foliation trajectories
E
o extant K-feldspar < 200°C
• K-feldspar reheated to 200-250°C
137-130 Ma
130-125 Ma
125-120 Ma
120-116 Ma
Z: zircon
H: hornblende (Ar/Ar)
M: muscovite (Ar/Ar)
B: biotite (Ar/Ar)
h: hornblende (K/Ar)
m: muscovite (K/Ar)
b: biotite (K/Ar)
K: K-feldspar (Ar/Ar)
p: plagioclase (Ar/Ar)
principal extension direction
Cretaceous transtensional flow

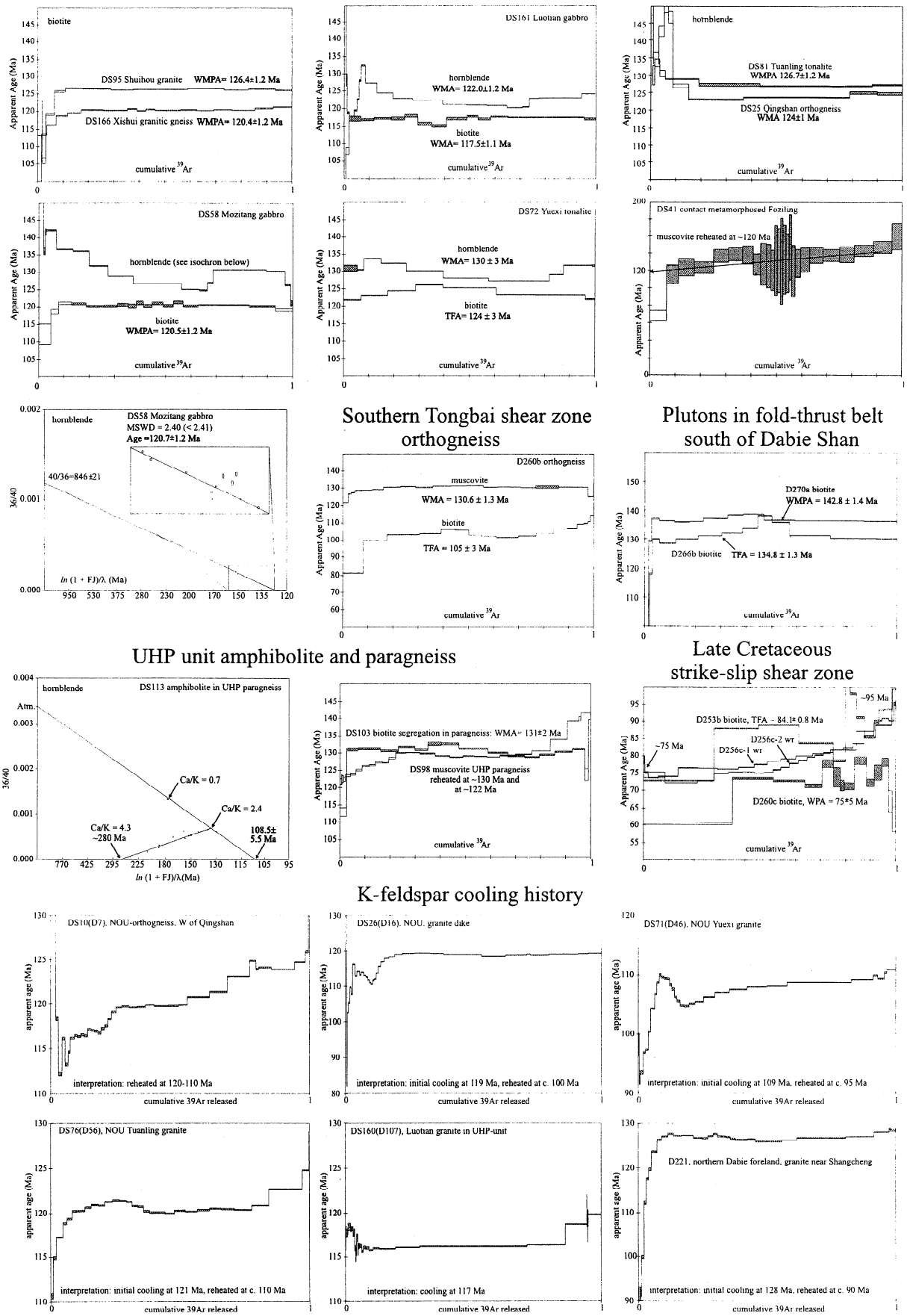

Figure 4. (a) New $^{40}Ar/^{39}Ar$ spectra. See Table 2 for sample location and Table 3 for age data and interpretations. Weighted mean ages (WMA) and weighted mean plateau ages (WMPA) were calculated using shaded steps. TFA, total fusion age. Uncertainities are 1σ. "Atm." in the inverse isochron diagrams is the $^{36}Ar/^{40}Ar$ of the atmosphere (1/295.5). K-feldspars are interpreted semi-quantitatively after the multi-diffusion-domain concept [*Lovera et al.* 1997]. MSWD, mean square weighted deviation. (b) Diffusion-domain analysis of metamorphic K-feldspars: spectra and quantitative analyses.

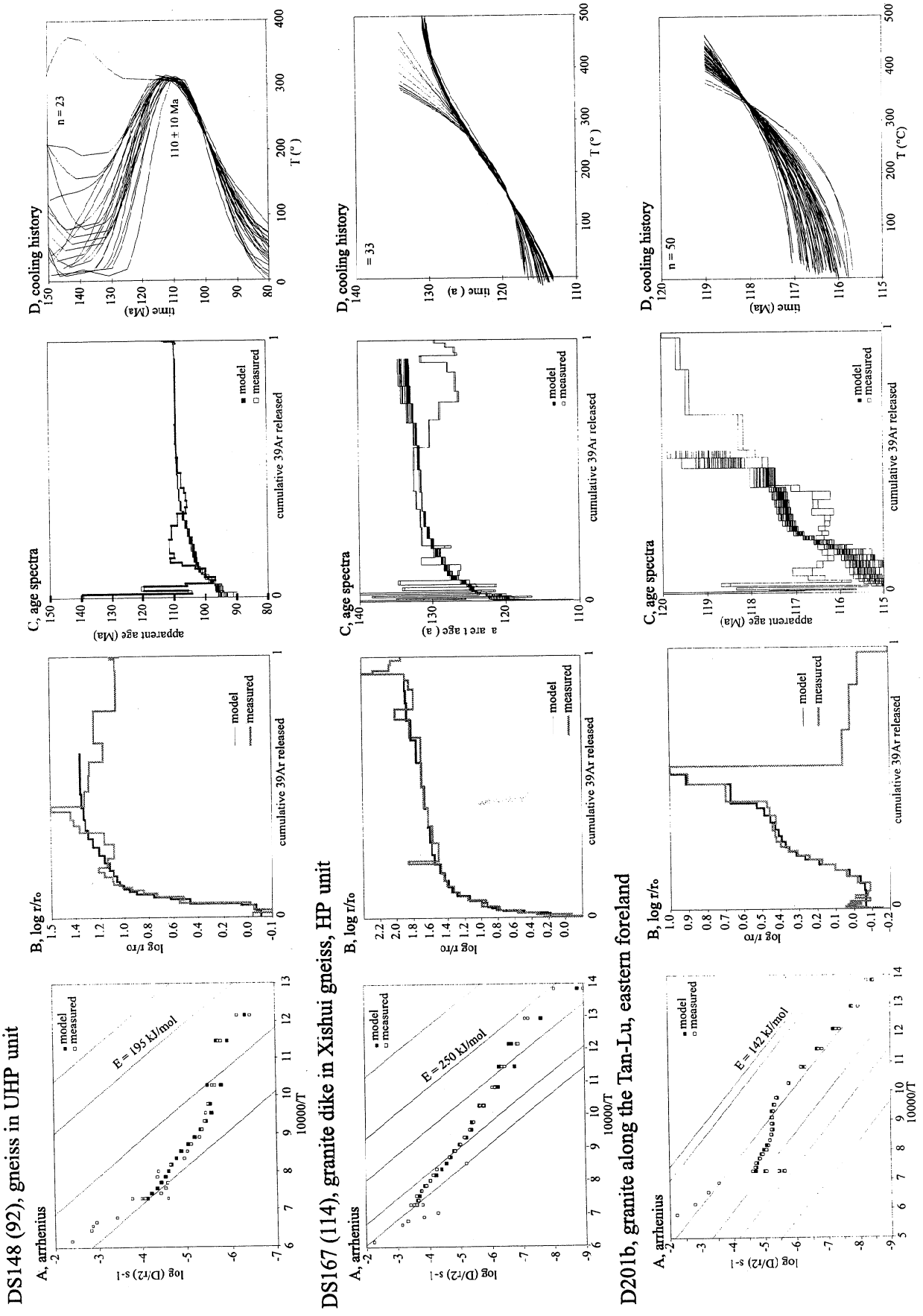

Figure 4. (continued)

Table 2. Sample Descriptions and Locations

Sample	Stop	Rock	N Latitude	E Longitude
DS10	D7	orthogneiss west of Qingshan, NOU	31°27.85'	115°54.70'
DS25	D16	grey gneiss, NOU	31°18.03'	115°56.09'
DS26	D16	granitic layer in NOU	31°18.03'	115°56.09'
D32	D32	detrital K-feldspar Upper Cretaceous K_2x (Xiafuqiao Formation) red bed	31°21.53'	116°22.17'
DS41	D28	contact metamorphosed Foziling	31°47.85'	115°14.75
DS58	D37	hornblende biotite gabbro near Mozitang, NOU	31°14.34'	116°20.39'
DS71	D46	granite with weak foliation near Yuexi, NOU	31°04.48'	116°30.04'
DS72	D47	biotite hornblende tonalite near Yuexi, NOU	30°55.18'	116°22.11'
DS76	D56	weakly foliated granitoid near Tuanling, NOU	30°48.37'	116°04.47'
DS81	D57	weakly deformed hbl-bio tonalite near Tuanling, NOU	30°49.23'	116°04.42'
DS95	D71	biotite granite along Yuexi–Shuihou transect, NOU	30°42.47'	116°23.26'
DS98	D71	UHP paragneiss along Yuexi–Shuihou transect	30°42.47'	116°23.26'
DS101	D74	qtz-bio-ksp vein in UHP paragneiss west of Qianshan	30°40.04'	116°29.13'
DS103	D74	biotite segregation in UHP paragneiss west of Qianshan	30°40.04'	116°29.13'
DS106	D75	bio-ksp-qtz segregation in UHP gneiss NW of Shima	30°32.48'	116°17.01'
DS113	D75	amphibolite in paragneiss NW of Shima, UHP unit	30°32.48'	116°17.01'
DS120	D76	bio-ksp-qtz-sph-ep vein in UHP gneiss	30°29.33'	116°18.14'
DS123	D79	granitic orthogneiss south of Queyeling, HP unit	30°24.18'	116°07.16'
DS148	D92	orthogneiss in UHP unit	30°53.98'	115°45.15'
DS160	D107	ksp granite near Luotian, UHP-HP unit	30°47.21'	115°37.55'
DS161	D109	gabbro near Luotian, UHP-HP unit	30°46.75'	115°25.45'
DS166	D113	granitic gneiss, HP unit	30°23.40'	115°11.01'
DS167	D114	late brittlely deformed granitic dike, HP unit	30°26.01'	115°11.48'
D201b	D201	granitic orthogneiss along Tan-Lu, eastern foreland	31°28.42'	117°22.69'
D220a	D220	detrital K-feldspar Paleocene E_1h (Hongqiao Formation) red beds	31°28.38'	116°34.75'
D221	D221	granite near Shangcheng, northern foreland	31°47.78'	115°21.52'
D266b	D266	metadiorite, southern foreland	30°13.13'	114°54.33'
D270a	D270	alkalic pluton, southern foreland	29°59.91'	114°50.25'

NOU, Northern Orthogneiss unit; UHP, ultrahigh pressure; HP, high pressure; hbl, hornblende; bio, biotite; qtz, quartz; ksp, K-feldspar; sph, sphene; ep, epidote.

fabrics within its core. Gneissic tectonites, mylonites, and ultramylonites are absent in the core; there is, however, a geometric concordance between the structures in the marginal orthogneiss and those in the oriented core intrusion. (2) Foliation is defined by shape preferred orientation of plagioclase, K-feldspar, biotite clots, and hornblende (if present). Quartz aggregates are weakly elongate, and deformation bands and undulose extinction are rare despite their locally strong preferred orientation. Isohedral triple junctions and plane boundaries suggest high-T deformation. (3) Automorphic perthitic orthoclase is surrounded by a fine-grained matrix of xenomorphic quartz and albite/orthoclase and sometimes cracks and strain shadows are filled with the matrix material. Those associations have been described as crystal mush [*Hibbard,* 1987; *Bouchez et al.* 1992]. These observations suggest that the fabric of at least some plutons at the core of the NOU were formed before complete solidification.

Cretaceous plutons and Cretaceous metamorphism do occur outside the NOU, e.g., within the UHP and HP units both in the Dabie and Hong'an Mountains and within the foreland [e.g., *Eide et al.,* 1994; *Hacker et al.,* 1996, this issue; *Hacker and Wang,* 1995]. Zircons of undeformed granites gave ages of 130 ± 3 Ma (UHP unit; *Hacker et al.* [1998]) and 132 ± 10 Ma (eastern Tongbai; *Ames et al.* [1996]). We dated a granitic gneiss and one gabbro from within the Dabie HP amphibolite unit using the $^{40}Ar/^{39}Ar$ method on hornblende and biotite (Figures 3b and 4a and Tables 2 and 3). Gabbroic xenoliths in a catazonal granite (DS161) yielded weighted mean ages of 122 ± 1.2 Ma and 117.5 ± 1.1 Ma for hornblende and biotite, respectively. Biotite from a granitic gneiss (DS166) from the southern margin of Dabie gave a 120.4 ± 1.2 plateau age. Biotite from a granite in the central Hong'an yielded 128.3 ± 0.3 Ma [*Eide et al.,* 1994]. Two samples from paragneisses of the UHP unit gave biotite and muscovite ages indicating Cretaceous cooling, as did a hornblende age from a HP amphibolite (Tables 2 and 3 and Figures 3b and 4a). The phengite spectrum from DS98 includes a plateau age of 129.4 ± 1.3 Ma, bounded by low-T steps decreasing toward 122 Ma and high-T steps that point toward ~145 Ma. We interpret this spectrum to be compatible with the other data: initial closure at >145 Ma, long-term Ar loss at 129 Ma, and short-term reheating at ~122 Ma. DS103 comprises a biotite from a segregation vein close to the Tan-Lu fault at the eastern age of the Dabie Shan; it yielded a weighted mean age of 131 ± 2 Ma. DS113 hornblende yielded a crankshaft-shaped spectrum suggesting excess Ar. An isotope correlation diagram suggests mixing among three components: an old, higher Ca/K component with an apparent age of ~280 Ma; a young, lower Ca/K component of ~108.5 Ma; and atmosphere. We propose that the 108.5 ± 5.5 Ma age reflects reheating of pre-Cretaceous hornblende in this HP amphibolite.

A belt of Cretaceous magmatic rocks straddles the northern margin of both the Dabie and Hong'an Shan [*Hacker et al.,* 1996; *Webb et al.,* 1999a]. Randomly oriented muscovite from a contact metamorphic gneiss (Foziling Group) yielded an Ar loss (?) profile from ~150 to 120 Ma (DS41, Tables 2 and 3 and Figure 4a). In addition, plutons dot the foreland fold-thrust belt south and east of the Dabie Shan [*Hacker et al.,* 1996]. We dated biotite from two plutons from the fold-thrust belt south of Dabie (Tables 2 and 3 and Figure 4a). The spectra are discordant, with weighted mean ages of 142.8 ± 2 and 134.8 ± 1.3 Ma (D266b and D270a). These foreland cooling ages are thus similar to or older than the oldest zircon ages from the NOU.

Table 3. Summary of $^{40}Ar/^{39}Ar$ Data

K-Feldspar

Sample	Mineral	J	Weight mg	Grain Size μm	Interpretation
DS10	ksp	0.003635	5.9	400	initial cooling prior to 125 Ma; reheating and cooling at 115 ± 10 Ma
DS26	ksp	0.003683	9.7	400	initial cooling at 119 ± 1 Ma; reheating and cooling at 100 ± 10 Ma
DS71	ksp	0.004614	7.2	400	initial cooling at 109 ± 1 Ma; reheating and cooling at 95 ± 10 Ma
DS76	ksp	0.003648	8.9	400	initial cooling at 120.6 ± 1.2 Ma; reheating and cooling at 110 ± 10 Ma
DS101*					initial cooling prior to 175 Ma; reheating and cooling at 140 ± 10 and 90 ± 10 Ma
DS106*					initial cooling prior to 170 Ma; reheating and cooling at 90 ± 20 Ma
DS120*					initial cooling prior to 190 Ma; reheating and cooling at 90 ± 10 Ma
DS123*					initial cooling at ~205 Ma; reheating at 150 ± 10 Ma and cooling at 90 ± 10 Ma
DS148	ksp	0.003622	9.5	400	intial cooling prior to 150 Ma; reheating and cooling at 110 ± 10 Ma
DS160	ksp	0.004468	7.1	400	cooling at 116 Ma
DS167	ksp	0.003583	10.1	400	cooling from 130 ± 5 Ma to 115 ± 5 Ma
D201b	ksp	0.004586	10.9	400	cooling from 119 ± 1 Ma to 116 ± 1 Ma
D221	ksp	0.004589	5.0	400	intial cooling from 128 ± 1 Ma; reheating and cooling at 90 ± 10 Ma
D244b*					initial cooling prior to 175 Ma; reheating and cooling at 150 ± 20 and 120 ± 10 Ma
D247a*					initial cooling prior to 150 Ma; reheating and cooling at 135 ± 15 and 95 ± 10 Ma
D249c*					initial cooling prior to 170 Ma; reheating and cooling at 130 ± 5 Ma
D256A†	ksp	0.004591	4.8	400	initial cooling prior to 90 Ma; reheating and cooling at 75 ± 10 Ma
D260C†	ksp	0.004572	7.7	400	initial cooling prior to 120 Ma; reheating and cooling 80 ± 10 Ma

Mica and Hornblende

Sample	Mineral	J	Weight mg	Grain Size μm	Total Fusion Age, Ma	Isochron Age, Ma	MSWD	$^{40}Ar/^{36}Ar$	Weighted Mean Age, Ma	Steps Used	^{39}Ar Used
DS25	hbl	0.003408	5.9	250	125.7 ± 1.2	122.5 ± 2.2	12	397 ± 256	124 ± 1‡	7–10/11	85
DS41	mus	0.004143	1	200	130.7 ± 2.4	¶					
DS58	hbl	0.004482	15	350	132.7 ± 1.3	120.7 ± 1.2‡	2.4	846 ± 21	na	7–12/18	57
	bio	0.004603	1.0	150	120.0 ± 1.2	120.4 ± 1.2	1.0	323 ± 25	120.5 ± 1.2‡§	4–16/17	80
DS72	bio	0.004615	2.0	250	123.9 ± 1.2	na	na	na	124 ± 2‡§	1–7/7	100
	hbl	0.004506	38	400	129.6 ± 1.3	na	na	na	130 ± 3‡	1–11/11	100
DS81	hbl	0.003415	9.5	250	127.6 ± 1.2	126.7 ± 1.2	2.0	300 ± 22	126.7 ± 1.2‡§	6–10/10	81
DS95	bio	0.004603	2.3	350	125.7 ± 1.2	126.3 ± 1.2	3.4	310±15	126.4 ± 1.2‡§	5–11/12	82
DS98	mus	0.004596	2.1	175	130.0 ± 1.3	‖					
DS103	bio	0.004606	1.7	250	130.3 ± 1.3	na	na	na	131 ± 2‡	2–15/17	95
DS113	hbl	0.003725	37	400	194.7 ± 1.9	~100 ± 10	na	na	na	na	na
DS161	hbl	0.004537	42	400	123.2 ± 1.2	na	na	na	122 ± 2‡	11–22/22	81
	bio	0.004607	2.5	350	117.0 ± 1.1	117.7 ± 1.1	2.6	292.3 ± 0.8	117.5 ± 1.1‡	3–17/17	98
DS166	bio	0.003676	3.6	200	120.9 ± 1.2	120.4 ± 1.2	1.3	284 ± 40	120.4 ± 1.2‡§	8–20/22	68
D253b	bio	0.004004	2.5	400	84.1 ± 0.8	na	na	na	na		
D256c-1†	wr	0.004572	5.5	na	79.6 ± 0.8‡	76.3 ± 0.8	1.0	799 ± 27	na	5–12/19	45
D256c-2†	wr	0.004582	14.3	na	78.4 ± 0.8‡	74.9 ± 0.8	1.6	1155 ± 38	na	7–16/23	35
D260b2	mus	0.004000	2.4	300	130.1 ± 1.3	na	na	na	130.6 ± 1.3‡§	7–19/21	84
	bio	0.003993	4.1	300	102.1 ± 1.0	na	na	na	104.5 ± 1.0‡§	3–14/17	79
D260c†	bio	0.004569	1.8	400	68.9 ± 0.7	na	na	na	75 ± 5‡§	2–12/14	62
D266b	bio	0.004022	4.1	200	134.8 ± 1.3‡	na	na	na	137.5 ± 5	3–13/13	97
D270a	bio	0.004027	2.0	400	142.2 ± 1.4	141.5 ± 1.9	2.3	703 ± 361	142.8 ± 2‡§	11–13/13	53

J is the irradiation parameter; MSWD is the mean square weighted deviation [*Wendt and Carl*, 1991], which expresses the goodness of fit of the isochron [*Roddick*, 1978]; isochron and weighted mean plateau ages are based on temperature steps and fraction (in percent) of ^{39}Ar listed in the last two columns. Abbreviations are as follows: hbl, hornblende; bio, biotite; mus, K-white mica; wr, whole rock pseudotachylite; na, not analysed. Complete tabulated $^{40}Ar/^{39}Ar$ data are available from the Department of Geological Sciences, University of California, Santa Barbara, at http://www.geol.ucsb.edu/~hacker/suppleData/UHPCret.

*Reported by *Hacker et al.* [this issue].

†Reported by *Webb et al.* [1999a].

¶"loss" profile from ~150 to 120 Ma.

‖"loss" profile from ~140 to 120 Ma.

§Weighted mean plateau age, rather than weighted mean age.

‡Preferred age.

3.2. Cooling History

We derived regional cooling patterns by contouring closure temperatures of various minerals (Figure 3e). In Figure 5a we relate the cooling pattern to the structural geometry. Dating of several minerals from the same outcrop (Figure 5b) and $^{40}Ar/^{39}Ar$ multi-diffusion-domain modeling in K-feldspar (Figure 4; *Lovera et al.*, [1997]; see appendix 1 for analytical details) provided local cooling histories. Only three K-feldspar samples yielded spectra suitable for full diffusion-domain analysis (Tables 2 and 3 and Figure 4b). DS148, an orthogneiss within the UHP unit, though probably affected by excess ^{40}Ar in the intermediate temperature steps, was fit by histories with cooling to near-surface conditions from pre-Cretaceous ages at 140 ± 10 Ma, followed by reheating at 110 ± 5 Ma. DS167, a late, brittlely deformed granitic dike within the HP unit in the southern Dabie, also did

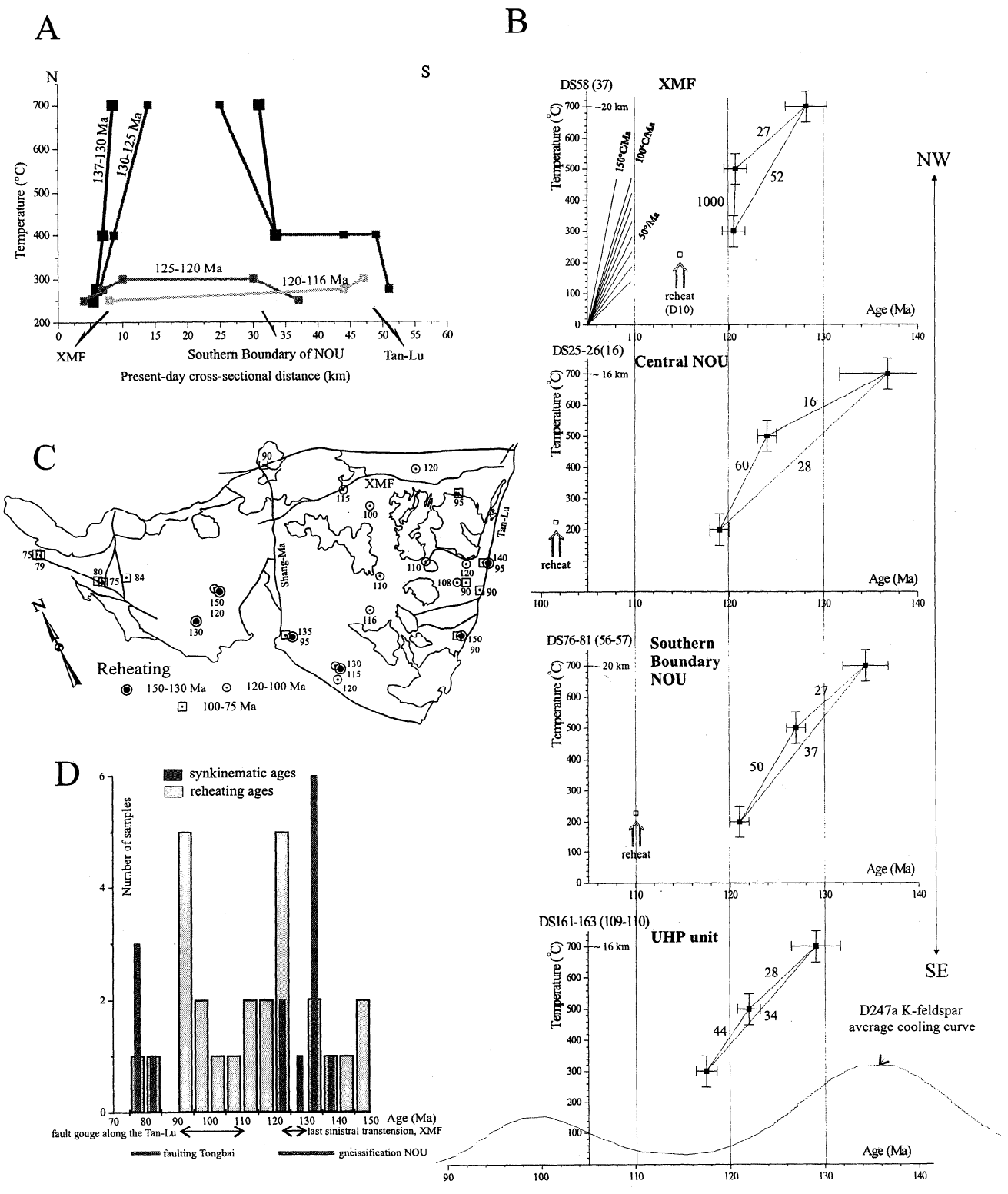

Figure 5. (a) Relationship of cooling ages to the structural geometry along a N-S profile across the Dabie Shan derived from Figure 3e. (b) Local cooling and reheating of samples arranged along a N-S profile across the Dabie Shan. Data (see Table 3, this study, and zircon ages from Hacker et al. [1998]) are from several minerals from the same or nearby outcrops. (c) Summary of reheating ages mostly based on $^{40}Ar/^{39}Ar$ diffusion-domain modeling in K-feldspar, see Table 3 and Figure 4 for data. (d) Histogram of reheating ages (see Figure 5c and Table 3, including Cretaceous ages from pre-Cretaceous UHP-HP rocks) compared with synkinematic ages (U/Pb zircon ages of the NOU gneisses; ages from pseudotachylites and low-T shear/fault zones). For interpretation of age range see text.

not yield a simple spectrum, but was fit by monotonic cooling from 130 ± 5 Ma to 115 ± 5 Ma. The fit to the spectrum for DS201, a granitic orthogneiss from the eastern Dabie foreland, appears to be poor, but the range of ages is small, 120 to 115 Ma, implying cooling at this time. The remaining eight K-feldspars were modeled qualitatively (Figure 4a and Table 3). They can be broken into two groups: samples depicting an initial cooling followed by reheating and samples for which the spectra are compatible with monotonic cooling.

From the zircon through K-feldspar data we derive the following cooling history: (1) Plutonism began in the central northern Dabie at 137–134 Ma as indicated by zircon ages; it continued in roughly the same area through 125–127 Ma. The $^{40}Ar/^{39}Ar$ ages define a thermal dome around these zircon ages. At this time the northern and southern margins of the Dabie–Hong'an area were at temperatures <250°C, and this was the last time that the UHP rocks were at temperatures >300°C (Figure 3e). (2) The post-125 Ma time slices of Figure 3e show subsequent decay of the thermal dome, with no major changes through ~115 Ma, at which time final cooling from the 140-125 Ma thermal event was recorded by K-feldspars (Figure 3a and Table 3). (3) The isotherms trend at high angle to the principal extension direction of Cretaceous crustal extension (see section 4.); thus magmatism and cooling were controlled by deformation (Figure 3e). (4) The XMF imposed the major control on cooling, but the zone of normal shear at the southern boundary of the NOU (see section 4.1.) and the Tan-Lu also affected cooling. The structural effect vanished after 120 Ma (Figure 5a). The cooling along the XMF started late (<128 Ma), and was rapid (≥50°C/Ma) and particularly pronounced at 120 Ma (DS58). Cooling in the central NOU started early (~135 Ma), was slow (~30°C/Ma), and lasted a long time (>25 Ma); it was earliest along the southern border of the NOU (Figure 5b). (5) Low-T thermochronometers, particularly K-feldspars, indicate regional reheating to ≤300°C throughout the Hong'an-Dabie (Figures 5c and d). Reheating can be broken into several events: (1) The UHP-HP units of the Hong'an-Dabie were reheated at 130-150 Ma; this event peaked within the NOU as the 140-125 Ma thermal event. Figure 5b (lowermost plot: UHP unit) shows for the southeastern Dabie that intrusion of a Cretaceous granite and cooling of its roof was preceded by reheating of a UHP-HP paragneiss. Assuming that a regional increase in thermal gradient is crucial for the initiation of large-scale crustal extension in the Dabie (see section 4.) and that crustal extension focused magmatism within the NOU, the time of reheating in the UHP units provides an estimate of the onset of Cretaceous deformation. *Hacker et al.*'s [this issue] diffusion-domain modeling of five K-feldspar samples from the UHP-HP unit (see summary in Table 3) suggests an upper bound of 140 ± 10 Ma. (2) The UHP/HP units and the NOU were reheated at 120-110 Ma; no deformation has specifically been tied to this time frame (Figure 5d). (3) At 90-100 Ma, reheating was localized in the eastern and western Dabie, particularly along the Tan-Lu and probably also along the Shang-Ma fault. This time corresponds to a major faulting episode along the Tan-Lu (90-110 Ma, mean 98 Ma, dating on fault gouge illite, Shandong province [*Chen et al.*, 1989]). (4) The southern Tongbai shows initial cooling prior to 90 and 120 Ma, followed by an event at 75-84 Ma (Table 3 and *Webb et al.* [1999a]). The latter event was probably deformation related, as pseudotachylites occur along a NW trending fault zone.

3.3. Crystallization Depths

Intrusion depths of 16 intermediate calcalkaline plutons and orthogneisses of the Dabie Shan were calculated using the calibrations of *Hollister et al.* [1987] and *Schmidt* [1992] of the Al-in-hornblende (Al-in-hbl) geobarometer (Table 4). Figure 3d shows the regional distribution of our data and those of *Ma et al.* [2000], also derived using *Schmidt*'s [1992] calibration, and pressure (P) contours obtained using a kriging technique; separate contours combine these data with P estimates by *Zhang et al.* [1996] using the amphibole-plagioclase method of *Blundy and Holland* [1990]. Because of the limited availability of suitable rocks and the regionally uneven sampling, only trends can be specified: (1) Pressures decrease toward the center and the northeastern margin of the NOU. (2) The rocks of the NOU were exhumed from an average depth of 18 km (5.1 kbar, assuming a rock density of 2800 kg/m^3 and using the Al-in-hbl data only). Assuming that the NOU rocks reached ~5 km depth (~200°C) at ~115 Ma, they were exhumed by an average of ~1.0 mm/yr since

Table 4. Hornblende Barometry of Cretaceous Orthogneisses and Granitoids

DS	Analyses	Al Atoms pfu	P*	P†	i/e Presence	Rock
12	15	2.05 ± 0.04	6.8	6.8	i	partial melt
18	20	1.76 ± 0.04	5.4	5.2		mafic block
20	21	1.68 ± 0.04	5.0	4.7	i	dioritic gneiss
25	28	1.58 ± 0.03	4.5	4.2	i	generic grey gneiss
30	14	1.73 ± 0.03	5.2	5.0	i	foliated tonalite
31	21	1.88 ± 0.02	5.9	5.8	i	Yanzihe tonalite
34	11	1.97 ± 0.06	6.4	6.3		partial melt
56	14	1.49 ± 0.06	4.1	3.7		Mozitang augen gneiss
58	19	1.76 ± 0.05	5.4	5.2		Mozitang tonalite
64	9	1.50 ± 0.04	4.1	3.7		tonalite
67	13	1.51 ± 0.05	4.2	3.8		gneiss
72	9	1.76 ± 0.07	5.4	5.2		Yuexi granite
81	20	1.79 ± 0.03	5.5	5.3	i	tonalite
161	16	1.52 ± 0.02	4.3	3.9	i	Luotian tonalite
166	14	2.44 ± 0.02	8.6	9.0	e	tonalite
167	16	2.22 ± 0.06	7.6	7.8	e	granitic dike

DS, sample name; Analyses, number of analyses; Al Atoms pfu, Al atoms per formula unit. All samples contain K-feldspar, plagioclase, quartz, biotite, sphene, and magnetite. Here i, ilmenite present; e, igneous epidote present.

*Pressure (P) in kbar after *Schmidt* [1992].

†Pressure (P) in kbar after *Hollister et al.* [1987].

peak intrusion activity at 133 Ma. (3) The orientation of the isobars (Figure 3d) corresponds well to that of the isotherms, especially to those of the 130-125 Ma frame (Figure 3e), and the isobars trend subparallel to the XMF. (4) Cretaceous plutons in the UHP/HP units were intruded up to 15 km deeper than in the NOU. Maximum Cretaceous exhumation is ~30 km. As the bulk of the UHP units in which the plutons intruded had cooled to <300°C at 170 Ma (after the Triassic exhumation; *Hacker et al.* [this issue]), a subduction-type geothermal gradient of ~10°C/km must have prevailed after the UHP orogenesis. (5) The trend of the isobars is at high angle to the principal extension direction of Cretaceous crustal extension. Exhumation, magmatism, and cooling (see also sections 3.1. and 3.2.) were thus controlled by Cretaceous deformation.

3.4. Cooling of the Dabie Shan from Detrital Grains in the Northern Foreland Basin

The extensional Hehuai basin along the northern margin of the Hong'an-Dabie contains up to 5 km of Cretaceous and up to 3 km of Eocene sedimentary rocks [*Han et al.*, 1989]. At its southern margin these rocks comprise nonmetamorphic alluvial fan and fluvial deposits with partly well-rounded pebbles of >1 m maximum diameter. Detrital K-feldspars from two localities (D32 and D220, Cretaceous and Eocene, respectively; Figure 2c; 10 and 30 km north of the present XMF outcrop), both comprising poorly sorted conglomerates with moderately rounded marble, gneiss, and granite pebbles, were dated by the $^{40}Ar/^{39}Ar$ method [*Hacker et al.*, this issue]. The source terrane was dominated by rocks that cooled to <200°C between 123 and 119 Ma. These ages are only slightly older than the initial K-feldspar cooling ages from the NOU (~118 Ma, Table 3) and overlap with rapid cooling along the XMF (~121 Ma, Figure 5b, first plot). The ages suggest that major exhumation along the XMF was over at ~120 Ma, as otherwise we would expect younger detrital grains; although we dated a large number of detrital grains, the latter statement needs corroboration by additional dating. Both the narrow age range of the detrital grains and the coeval rapid cooling along the XMF imply a causal link between exhumation of the NOU and motion along the XMF and, more specifically, suggest that rapid cooling is related to heat advection by normal faulting along the XMF and not merely to conductive cooling of the NOU.

4. Cretaceous Reactivation of the Hong'an-Dabie Belt: Structural Geometry and Deformation Kinematics

The Hong'an-Dabie belt shows Cretaceous reactivation, with penetrative fabrics restricted to the NOU and discrete fault/shear zones elsewhere within the orogen. Regionally, structures and related kinematics outline consecutive, mostly continuous events, which are interpreted as a regionally consistent sequence of ductile to brittle deformation events active during regional cooling or, more rarely, heating. Our geometric, kinematic, and dynamic data are summarized in Figures 6-13 and Table 5 and are based on fieldwork and reevaluation of existing geological maps. Penetrative, crystal-plastic structures and their regional tracing enable us to analyze the orientation of strain associated with the formation of the major structural features. Information on the noncoaxial component of the strain history was obtained from shear criteria in the *XZ* plane of finite strain ($X \geq Y \geq Z$, principal axes): schistosité-cisaillement (S-C) and shear band fabrics, asymmetric boudinage and strain shadows, rotated remnants of fractured minerals, and sheared minerals [e.g., *Simpson and Schmid*, 1983]. Deformation path and flow temperature interpretations of quartz crystallographic preferred orientations (textures) are based on comparisons with textures from other deformation zones where the path and the temperature have been established by independent criteria [e.g., *Schmid and Casey*, 1986; *Blumenfeld et al.*, 1986] and with textures derived from polycrystal-plasticity models and experimental data [e.g., *Wenk et al.*, 1989; *Tullis et al.*, 1973; *Dell'Angelo and Tullis*, 1989]. Appendix 2 summarizes our approach to fault slip analysis and definition of stress tensor groups in the brittle crust and reviews the applied calculation techniques.

Figure 6 plots stretching trajectories of regional ductile flow and extension (σ_3) trajectories for the two most penetrative regional faulting events, together with summary plots of principal stress orientations ($\sigma_1 \geq \sigma_2 \geq \sigma_3$) calculated from homogeneous, single-outcrop fault striae sets (Table 5). The "relative chronology matrix" [*Angelier*, 1994] diagram at the center of Figure 6 summarizes the number of subsets for which geologic overprinting criteria constrain a relative age sequence and thus documents a deformation history in terms of superposed regional stress fields. The upper right triangle of the matrix contains all field-determined chronologies consistent with the classification adopted, whereas the lower left triangle is the domain of incompatibility. For example, in 11 cases the field data show that homogeneous subsets, representing the regionally consistent stress orientations of event 2, are relatively younger than homogeneous subsets collected in the same outcrops and representing the regionally consistent stress orientations of event 1; there are, however, three inconsistent observations in this case.

Cretaceous structures are dominantly normal and strike-slip shear zones and faults; by far the highest strain was accommodated during the ductile flow event. The major crust-shaping event was the formation of the magmatic-metamorphic-structural dome of the NOU under general NW-SE subhorizontal extension and subvertical and subordinate NE-SW contraction, with activation of the XMF detachment fault. The characteristic regional feature is a general clockwise change in the orientation of the subhorizontal strain/stress axes; that is, extension changed from early NW-SE to intermediate N-S to late, subordinately developed, NE-SW (Figure 6). Below, our description follows the major structural subdivisions.

4. 1. Xiaotian-Mozitang Fault Zone

The XMF separates the NOU from the northern foreland, comprising the Luzhenguang, Foziling, and Meishan formations [*Hacker et al.*, 1996], and Jurassic and Cretaceous igneous rocks. It begins in the westernmost Dabie as a wide, NW trending zone of sinistral transpression, grades eastward into a generally 30°-50°-dipping, west trending sinistral transtensional zone, and accommodates mostly sinistral strike-slip shear in its eastern, WNW trending segment (Figure 7). In the east it is covered by Eocene sediments or, locally, interacts with NE striking, retrograde chlorite + epidote + quartz + albite tectonites, mylonites, thin chlorite-rich ultramylonites, and brittle-ductile faults, older than the cataclasites of the Cenozoic Tan-Lu (Figure 8). This complex strike-slip deformation was active during the Cretaceous cooling (Figures 7b and 8, D203, D205, D207 and D209); however, no well-defined, Cretaceous Tan-Lu exists here.

We studied three sections across the XMF (Figures 7 and 8); they show the following common features: (1) The detachment

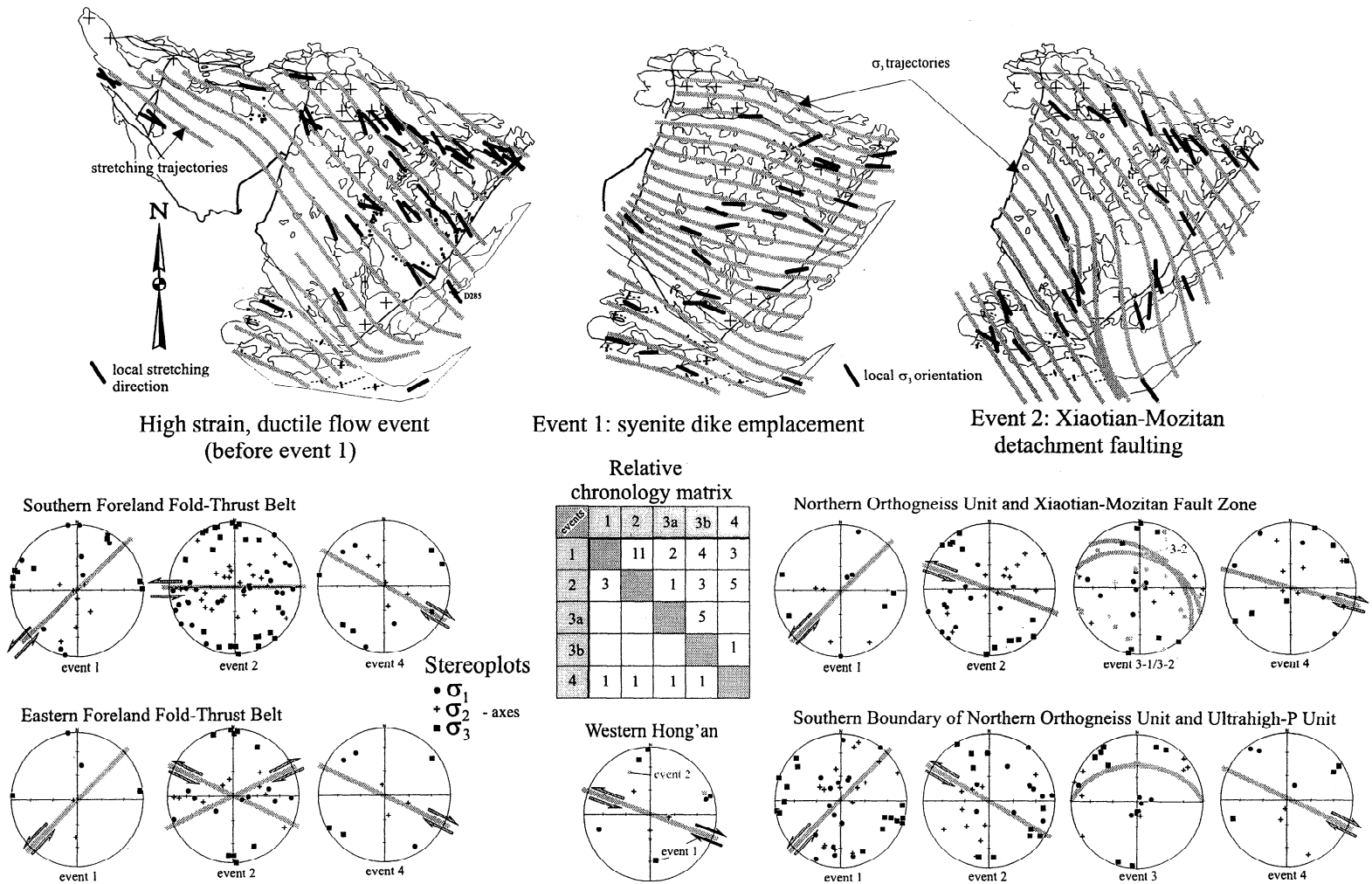

Figure 6. Stretching trajectories of regional ductile flow and extension (σ_3) trajectories for the two most penetrative regional faulting events together with summary plots of principal stress orientations ($\sigma_1 \geq \sigma_2 \geq \sigma_3$) calculated from homogeneous, single-outcrop fault striae sets (Table 5). See Figures 7-13 for the orientation of foliation, stretching lineation, and shear zone/shear band structures of the ductile flow event; this event accommodated by far the highest strain in the Hong'an-Dabie region. The "relative chronology matrix" at the center summarizes the number of subsets for which geologic overprinting criteria constrain a relative age sequence and thus sets up the deformation history plotted as "events" in terms of superposed regional stress fields. In this matrix, rows correspond to the older event, and columns correspond to the younger one. The upper right triangle of the matrix contains all chronologies consistent with the classification adopted, whereas the lower left triangle is the domain of incompatibility.

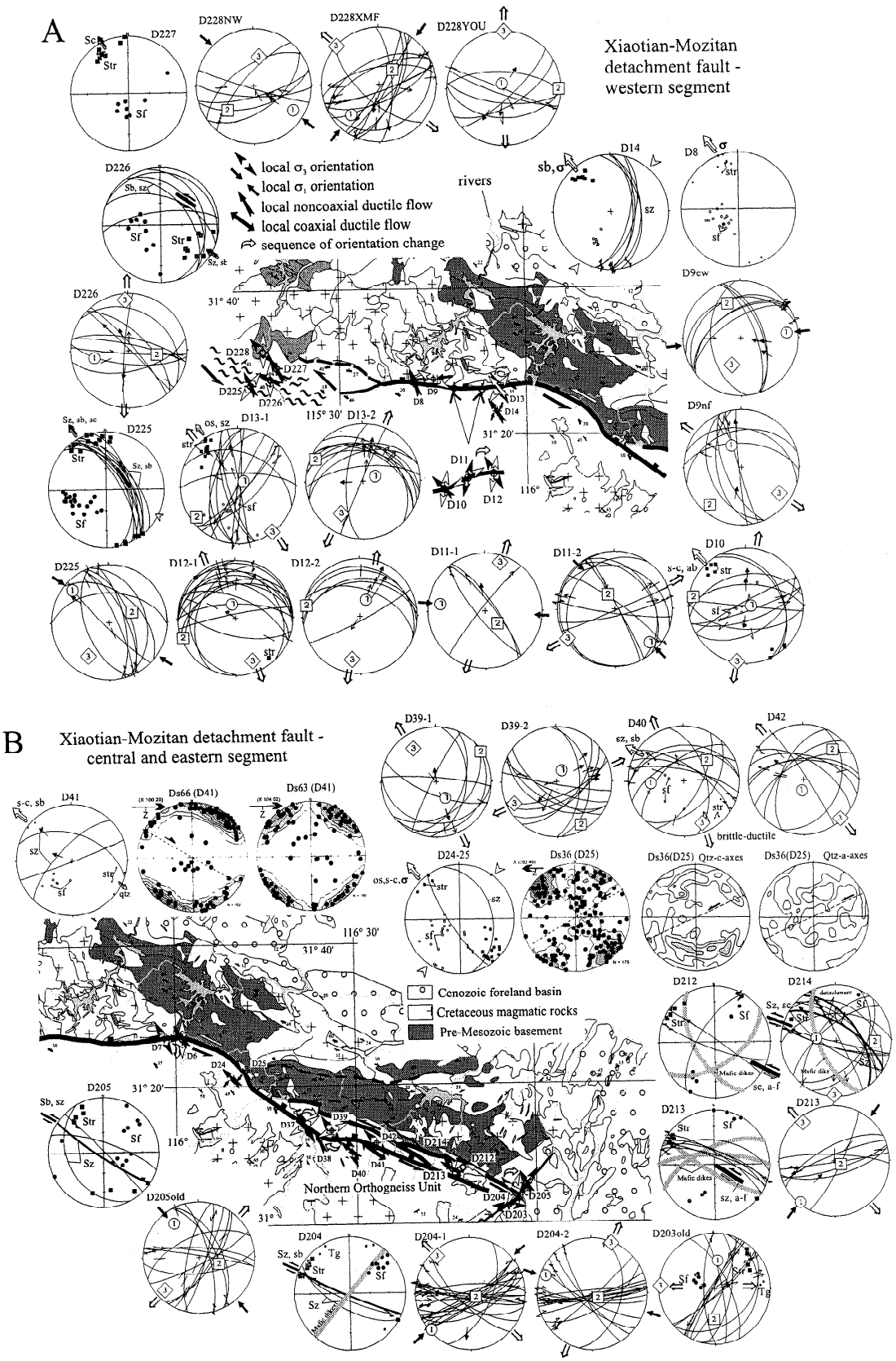

Figure 7. Cretaceous structural data from the Xiaotian-Mozitang detachment fault (northern Dabie). Sf, foliation; str, stretching lineation; *B*, fold axis; sb, shear band; sc, schistosité-cisaillement fabric; sz, shear zone; s, sigma clast; d, delta clast; *X*, *Y*, and *Z*, principal axes of finite strain; ab, asymmetric boudinage; 1 and 2, first and second deformation fabric element; tg, tension gash or fracture; ss, bedding; qtz, quartz. All diagrams are lower hemisphere, equal-area diagrams. U-stage data show single *c* axes and distribution contoured with Kamb's method; x-ray texture goniometer *c* and *a* axes data (*c* axes orientations are orientation distribution function derived) are contoured in multiples of random distribution. Double arrows with some plots give the sense-of-shear (hanging wall displacement) interpretation. Fault striae data are as in Figure 2c (see Figure 2 caption); arrows around the plots give calculated local orientation of subhorizontal principal contraction and extension.

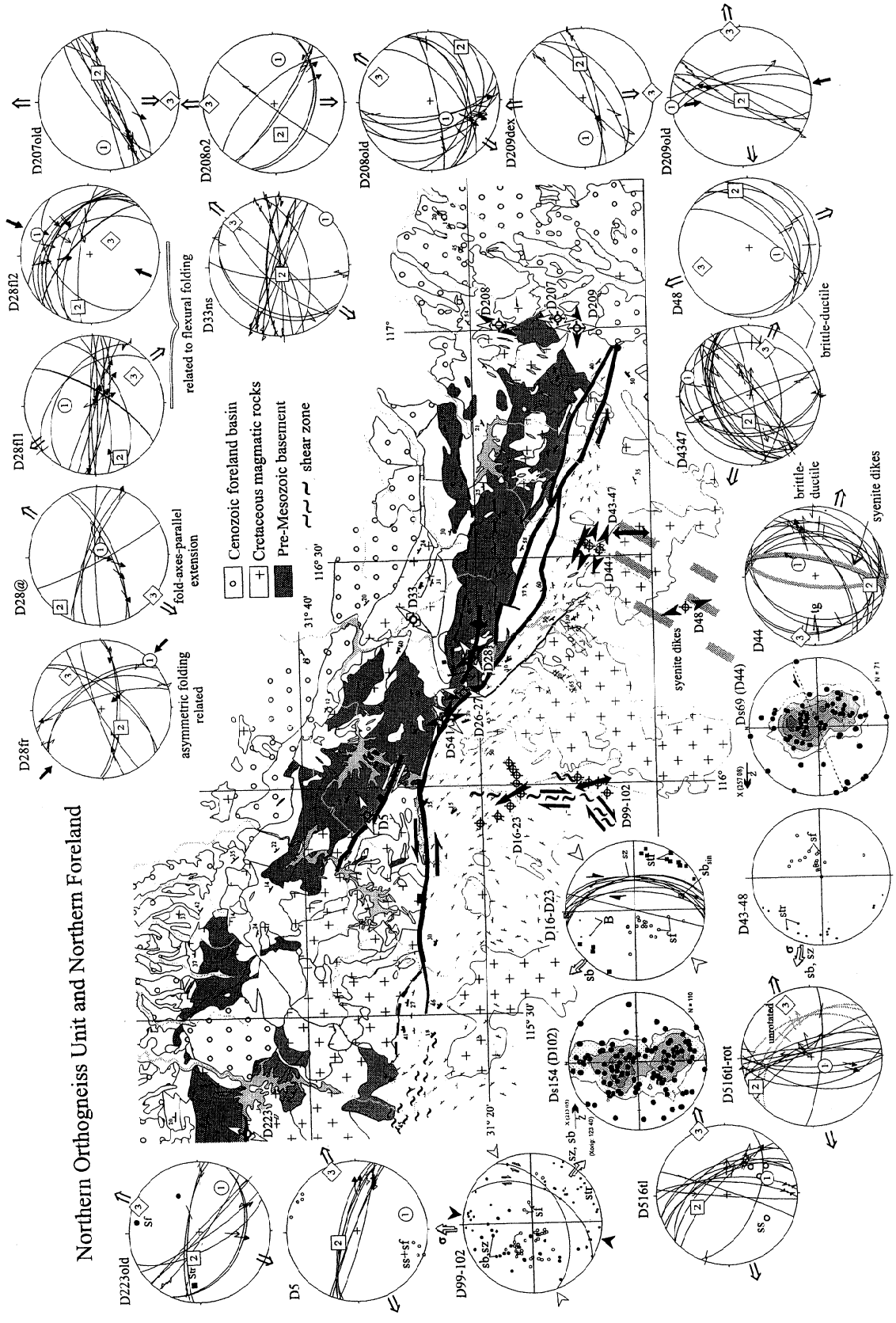

Figure 8. Cretaceous structural data from the Northern Orthogneiss unit and the northern Dabie foreland. See Figure 7.

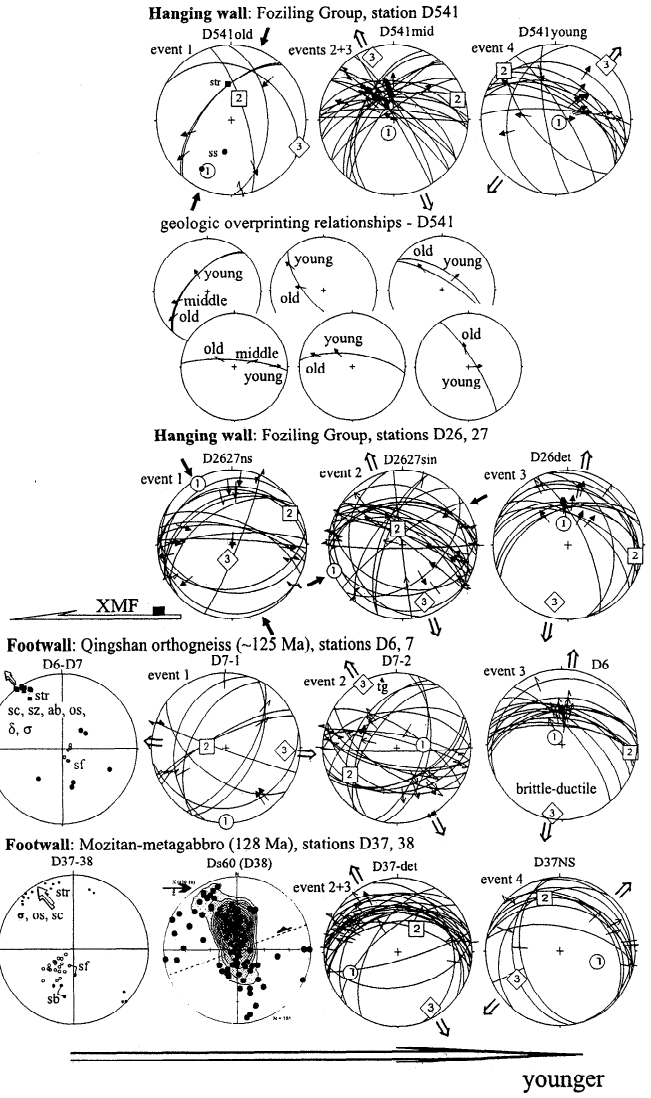

Figure 9. Type examples for the observed Cretaceous kinematic history from locations immediately above and below the Xiaotian-Mozitang detachment fault (XMF, northern Dabie), illustrating, as an example, the overprinting relationships observed on six different faults in station D541. For location of stations see Figure 7.

separates a hanging wall of Early Cretaceous volcanic rocks lacking ductile deformation and metamorphism or pre-Mesozoic basement from a footwall of Cretaceous orthogneisses. (2) During cooling, brittle deformation migrated into the footwall, causing retrograde shear/fault zones anastomosing around lozenge-shaped boudins. Epidote, hematite, and chlorite coatings on faults and their growth behind steps testify to extensive fluid activity during cooling of the footwall intrusions and tie high-level faulting and deep-level flow temporally. (3) The detachment comprises a zone of chloritized breccia, locally involving pseudotachylite (e.g., station D214). (4) Figure 9 plots type examples for the observed kinematic history from locations immediately above and below the XMF and illustrates, as an example, the overprinting relationships observed on six different faults at station D541. The history started with top-to-NW, amphibolite-grade noncoaxial flow (dominant prismatic <a> glide in quartz, e.g., DS60, Figure 9, and ductile flow event of Figure 6). Greenschist-grade flow had a significant coaxial component (dominant basal <a> slip in quartz and mostly symmetric texture skeletons; DS36, DS63, and DS66, Figure 7b). E-W to SW-NE extension followed, clearly associated with NW-SE to N-S shortening by conjugate strike-slip, local thrust, and reverse faults (event 1 of Figure 6); the sinistral set strikes subparallel to the Cenozoic Tan-Lu fault zone (e.g., stations D203old and D205old, Figure 7b). A set of late, weakly ductile to undeformed syenite plutons (see, e.g., the finger-like stock, Figure 8 center), and a generally NE trending dike swarm of syenitic and more mafic dikes, intruded sinistral transtensive faults related to this stress field (e.g., D44, D204, and D212-D214, Figures 7b and 8). Top-to-NW to top-to-north shear accompanied the major, 30°-45°-dipping detachment faults of the XMF (events 2 and 3 of Figure 6 and field data in Figure 7). Dextral transtensive to dextral strike-slip faulting reactivated the XMF in a late stage (event 4 of Figure 6).

Using the 30° dip of the major ductile XMF shear zone and a ~20 km differential exhumation between the footwall orthogneisses (e.g., D37, Mozitang gabbro, crystallization depth at 19.6 km, Table 4) and the nonmetamorphic hanging wall

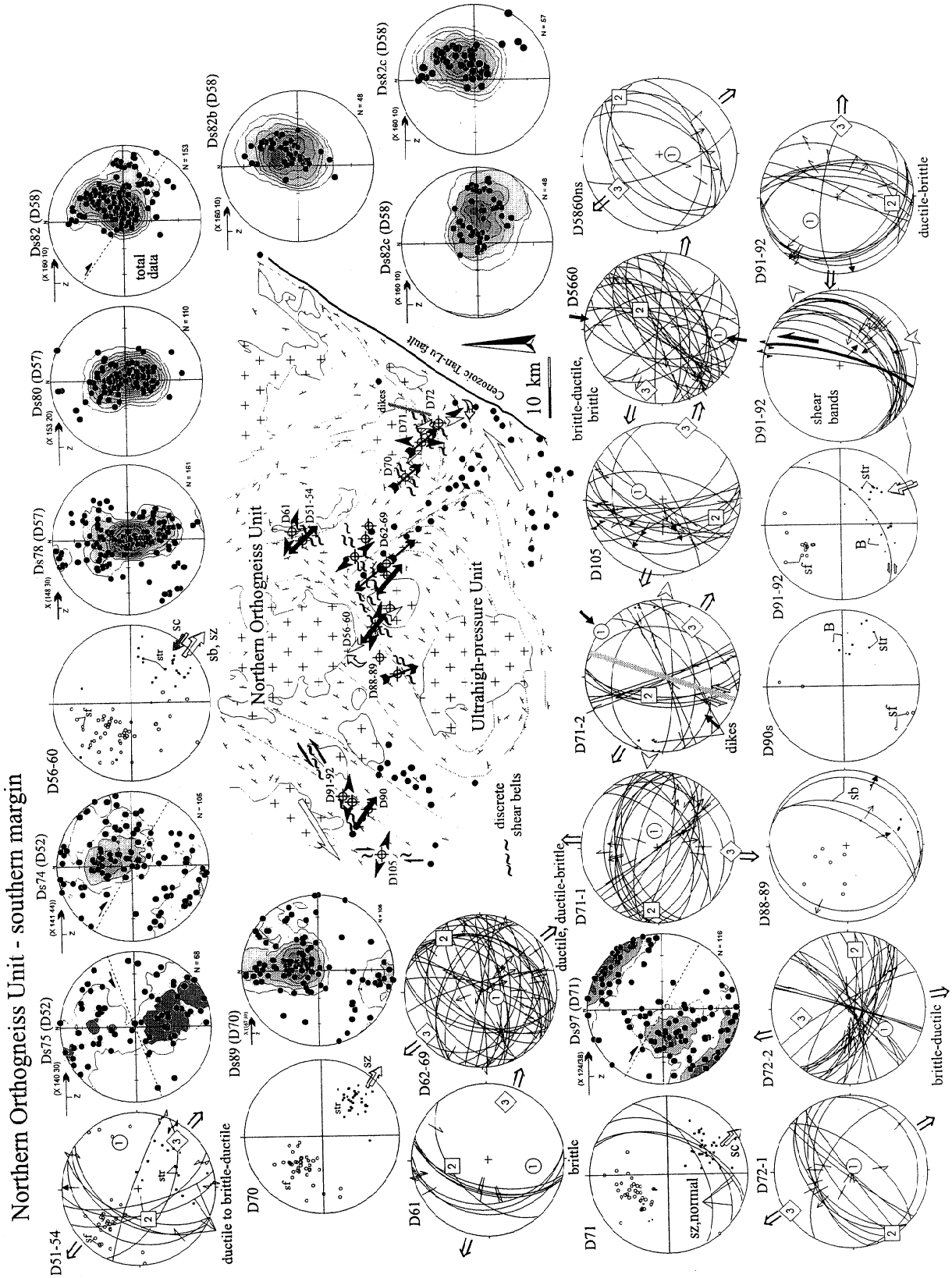

Figure 10. Cretaceous structural data from the southern margin of the Northern Orthogneiss Unit. Measurements in sample DS82 (station D58) comprise different parts of the same hand sample and distinct grains; see text for explanantion. See Figure 7.

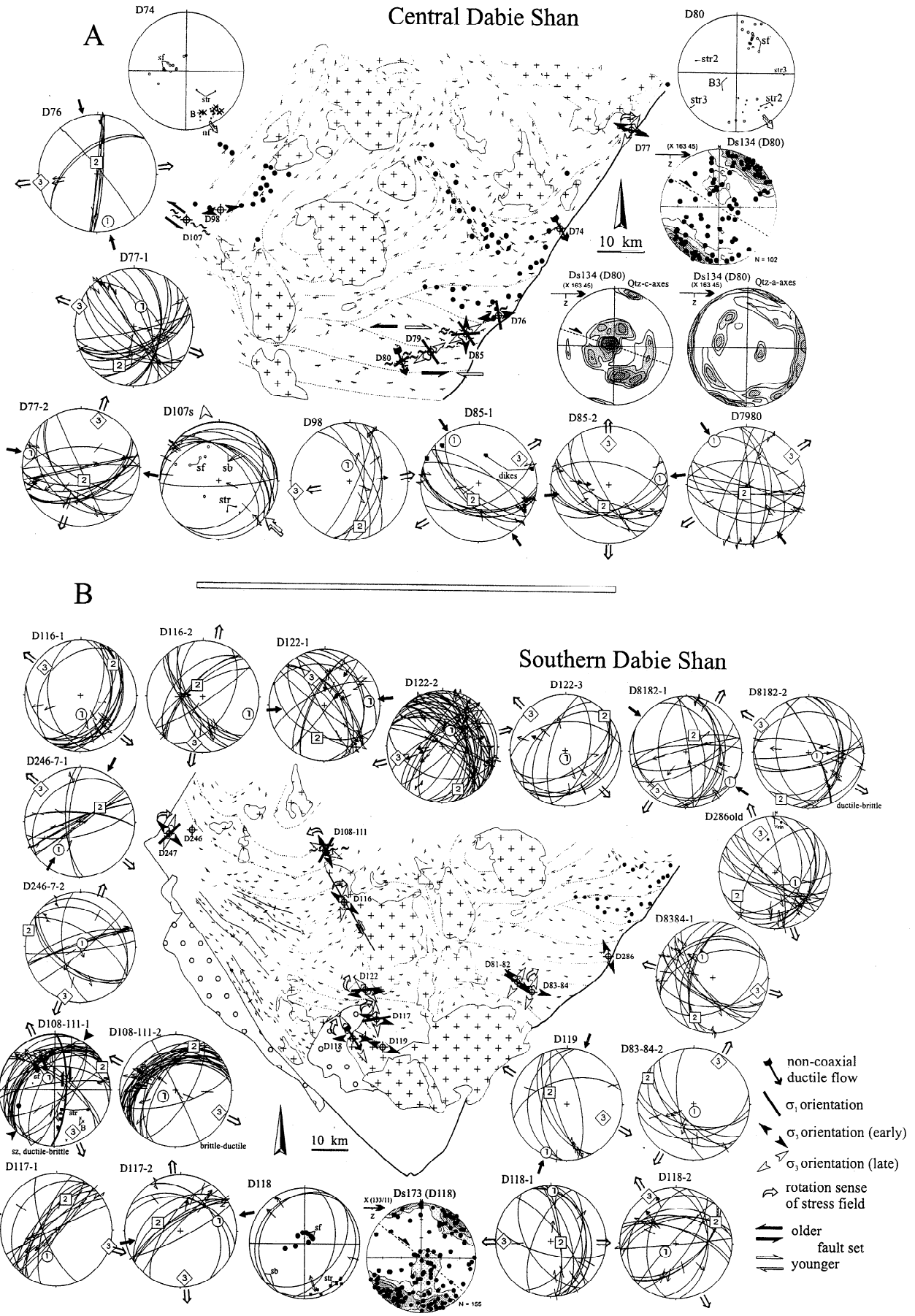

Figure 11. Cretaceous structural data from the central and southern Dabie Shan, comprising the Triassic UHP and HP units. See Figure 7.

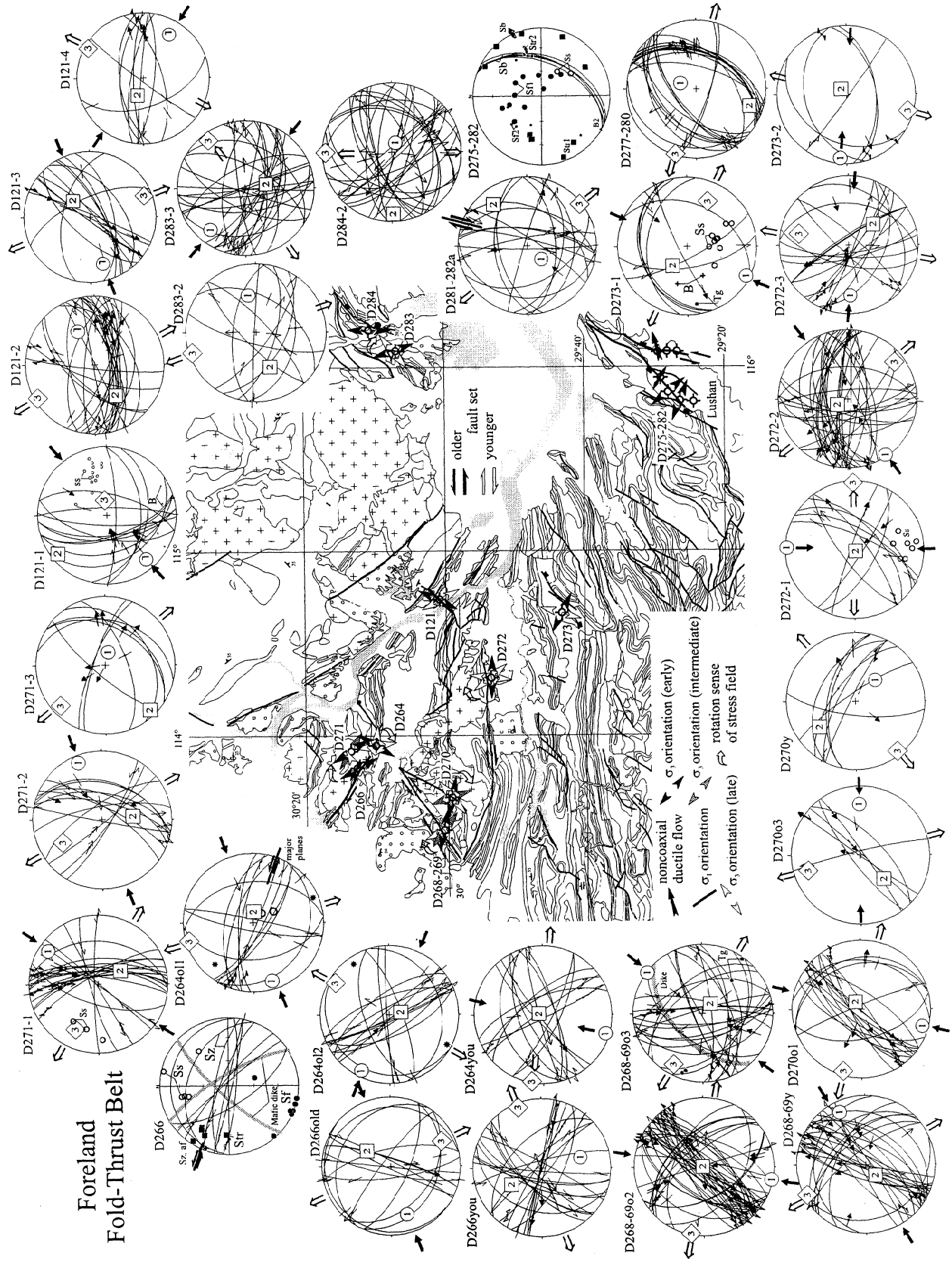

Figure 12. Cretaceous structural data from the southern and southeastern foreland of the Dabie Shan. The Yangtze river is in the center of the figure. See Figure 7.

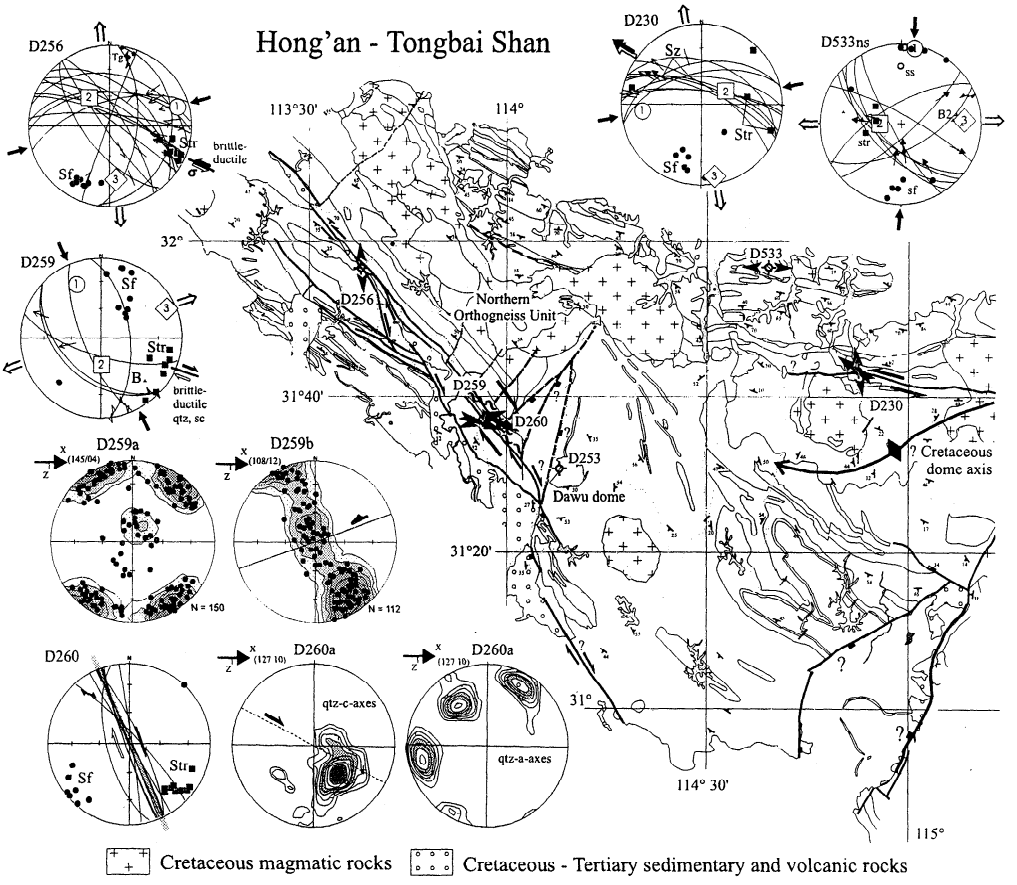

Figure 13. Cretaceous structural data from the Hong'an and Tongbai Shan with the UHP and HP units of the Hong'an Shan in the lower center of the figure. See Figure 7.

volcanics, we calculate ~40 km (heave 35 km) normal displacement along the XMF. This translates into ~80 km sinistral oblique slip, assuming that the ~30° pitch of the stretching lineation on the mylonitic foliation traces the displacement vector during ductile simple shear flow and that all the exhumation was accommodated within this structural geometry; brittle-ductile to brittle deformation was, however, mostly normal (Figure 9).

4.2. Northern Orthogneiss Unit

The core of the complex shows in situ melting (cpx + hbl + gar ⇒ qtz + ksp + plag + melt) in rare basement gabbro, the local formation of migmatites (with cpx + hbl restites), and multiple intrusion sequences. U/Pb zircon dating [*Xue et al.*, 1997; *Hacker et al.*, 1998] proved that the intrusion sequence observed at several localities (D43-D47, eastern NOU, Figure 8), (1) gabbro, (2) differentiated plagioclase-rich gabbro, (3) potassium feldspar + hornblende granodiorite, (4) aplite dikes and potassium-feldspar granite stocks and dikes, was not valid regionally: A partly mylonitized gabbro and an undeformed granodiorite have so far provided the youngest ages from the NOU, and a tonalitic orthogneiss provided the oldest age. Locally up to 60% of the central complex is made up of potassium feldspar granite dikes; small dikes often intruded parallel to the foliation.

Variation in foliation attitude in the center of the NOU is mostly the result of batholith intrusion (Figure 3d). The kinematics of high-grade deformation was in general top-to-(W)NW, although during cooling toward lower amphibolite facies a coaxial component was expressed by additional top-to-SE shear bands (e.g., Figure 8, stations within the NOU). In the core of the NOU dome, static annealing due to late-stage intrusions veiled earlier deformation structures.

Syenite dikes are common, particularly in the eastern Dabie. Intrusion followed NE trending, sinistral, strongly transtensional shear/fault zones, and the dikes themselves reflect sinistral transtensive shear; these shear zones parallel the trace of the Tan-Lu (Figure 8, D43-D48). Quench fabrics show that the country rock was relatively cool during dike intrusion. A qtz *c* axis texture in the sheared syenite dike of station D44 (DS69) shows dominant prism and rhomb <a> slip indicative of upper greenschist-grade flow [e.g., *Schmid and Casey*, 1986]. Deformation continued with hornblende + epidote + chlorite-coated ductile-brittle and brittle faults (event 1 of Figure 6) with the same sinistral-transtensive kinematics. The dikes were overprinted by N(W)-S(E) extension (events 2 and 3, Figure 6).

North to NE trending dextral shear zones were encountered throughout the northeastern Dabie (e.g., D16-D23 and D99-D102, Figure 8); together with conjugate sinistral shears and <a> folds they manifest significant NE-SW shortening accompanying NW-SE extension. This is in accord with constrictional strain, qualitatively evaluated from linear mineral fabrics in a number of outcrops, implying both NE-SW and vertical shortening during

Table 5. Location of Stations and Parameters of the Deviatoric Stress Tensor: Cretaceous Stress Field

Site	Lithology	Latitude†	Longitude†	Method	n	σ_1	σ_2	σ_3	F	R
D5	shale, volcanics	31°32.5'	115°56.35'	P-B-T	7 7	15 29	32 60	064 05		
D6	orthogneiss (K)			NDA	14 14	315 79	097 08	188 07	7°	0.5
D7-1	orthogneiss (K)*			P-B-T	9 9	180 01	273 69	093 21		
D7-2				P-B-T	20 20	084 60	240 27	332 04		
D9nf	granitoid (K)			NDA	8 8	335 56	221 15	125 21		
D9ew				NDA	9 9	084 20	340 34	199 49	11°	0.4
D10	orthogneiss (K)			NDA	10 10	091 83	280 07	190 01	17°	0.5
D11-1	volcanics			P-B-T	4 4	279 21	135 65	018 12		
D11-2				P-B-T	11 11	109 16	336 67	239 03		
D12-1	orthogneiss (K)			grid	15 13	346 70	250 02	159 20	17°	0.6
D12-2				NDA	7 7	021 65	282 04	191 24	10°	0.5
D13-1	granitoid (K)			grid	14 11	051 80	234 10	144 00	10°	0.5
D13-2				grid	13 13	051 85	158 01	248 05	5°	0.2
D26det	shale, limestone	31°22.66'	116°11.83'	NDA	13 13	349 66	099 09	193 22	18°	0.4
D26-27sin				NDA	26 25	250 01	343 72	159 18	28°	0.5
D26-27ns				P-B-T	16 16	331 06	062 12	197 73		
D28fr	shale, limestone (pre-K)*			grid	10 10	136 00	226 58	046 32	14°	0.1
D28@				grid	8 8	111 82	308 08	217 02	19°	0.2
D28fl1				grid	14 11	000 55	245 16	146 30	10°	0.6
D28fl2				grid	12 12	022 19	284 22	149 60	15°	0.1
D33ns	volcanics, conglomerate	31°26.4'	116°23.23'	NDA	18 17	136 04	251 80	045 09	18°	0.5
D37-det	orthogneiss (K)*	31°14.57'	116°20.65'	grid	22 19	247 30	039 57	150 13	10°	0.6
D37NS				NDA	11 10	106 47	344 26	237 31	18°	0.7
D39-1	volcanics	31°13.73'	116°25.07'	NDA	8 7	151 63	057 02	326 27	18°	0.5
D39-2				NDA	14 14	026 72	151 11	244 14	17°	0.2
D40	orthogneiss (K)	31°10.07'	116°30.13'	P-B-T	10 10	267 40	049 43	157 17		
D42	volcanics			P-B-T	9 9	243 64	045 25	137 03		
D43-47	orthogneiss (K)*	31°07.8'	116°31.52'	P-B-T	21 21	017 08	274 59	110 30		
D44	syenite (K)	31°06.05'	116°31.2'	NDA	15 15	036 66	191 22	285 09	12°	0.6
D48	granitoid (K)			P-B-T	6 6	194 56	078 16	339 28		
D51-54	orthogneiss			P-B-T	9 7	070 35	252 55	130 20		
D56-60	orthogneiss (K)*	30°47'	116°05'	P-B-T	32 32	186 19	052 64	284 17		
D58-60	orthogneiss (K)			P-B-T	10 10	181 76	056 08	321 31		
D61	orthogneiss (K)	30°49.14'	116°04.25'	P-B-T	9 9	189 31	351 50	108 21		
D62-69	orthogneisses (K)	30°49'	116°14.25'	NDA	36 32	202 72	056 16	323 10	21°	0.4
D71-1	granitoid (K)*	30°42.78'	116°23.43'	NDA	24 24	082 72	276 17	184 04	19°	0.5
D71-2				P-B-T	17 17	037 01	304 65	123 25		
D72-1	granitoid (K)	30°41.1'	116°26.42'	NDA	12 12	114 84	238 03	328 05	10°	0.4
D72-2				P-B-T	14 14	082 06	182 60	346 29		
D76	paragneiss (K-reheat)*	30°29.55'	116°18.25'	P-B-T	8 8	167 16	356 74	261 02		
D77-1	paragneiss	30°49.72'	116°39.47'	grid	23 18	020 60	200 30	290 00	19°	0.7
D77-2				P-B-T	18 18	285 09	166 72	020 15		
D79-80	ortho/paragneiss (K-reheat)*	30°24'	116°07'	P-B-T	15 15	324 07	191 79	057 07		
D83-84-1	orthogneiss (K-reheat)*	30°21'	116°00.47'	NDA	16 15	323 65	193 16	098 18	21°	0.5
D83-84-2				P-B-T	8 8	171 78	299 07	030 12		
D85-1	paragneiss	30°27.65'	116°14.98'	P-B-T	12 12	330 17	198 65	059 19		
D85-2				P-B-T	11 11	085 05	190 60	358 30		
D91-92	granitoid (K)*	30°53.45'	115°45.45'	P-B-T	16 16	319 52	187 28	094 07		
D98	ortho+paragneiss	30°45.88'	115°39.82'	P-B-T	7 7	352 68	167 21	259 06		
D105	orthogneiss (pre-K)	30°49.52'	115°38.12'	P-B-T	19 19	019 63	200 27	109 01		
D108-111-1	orthogneiss (K)*	30°47'	115°28'	NDA	25 23	320 70	064 05	156 19	15°	0.4
D108-111-2				grid	26 26	246 75	017 10	109 11	12°	0.4
D116-1	granitoid (K)	30°36.13'	115°26.68'	NDA	14 14	177 63	045 19	308 18	7°	0.4
D116-2				P-B-T	14 14	110 14	334 71	190 16		
D117-1	phyllite, shale	30°17.17'	115°31.25'	NDA	18 18	205 71	014 19	105 03	17°	0.9
D117-2				NDA	11 11	075 31	289 54	175 16	17°	0.7
D118-1	granitoid (K)	30°14.13'	115°26.6'	grid	13 10	002 10	098 75	269 15	16°	0.2
D118-2				grid	16 15	230 70	061 20	330 03	13°	0.6
D119	para+orthogneiss	30°10.83'	115°30.87'	NDA	7 7	203 06	303 59	110 30	9°	0.6
D121-1	limestone (Pe)	30°01.18'	115°21.75'	NDA	13 13	229 15	322 10	083 72	17°	0.3
D121-2				NDA	25 25	064 45	236 45	330 04	14°	0.7
D121-3				P-B-T	14 14	253 26	057 63	158 05		
D121-4				NDA	9 9	221 23	288 67	029 05	16°	0.6
D122-1	serpentinite	30°21.48'	115°30.02'	grid	19 16	085 20	192 39	334 44	23°	0.2
D122-2				grid	43 35	028 70	158 13	251 15	22°	0.6
D122-3				NDA	11 11	180 78	048 05	316 09	14°	0.5
D200old	orthogneiss (K)	31°47.69'	117°33.27'	NDA	21 20	092 13	315 72	184 12	17°	0.5
D200you	red beds (K)			NDA	13 13	093 71	268 19	358 02	17°	0.4

Table 5. (continued)

Site	Lithology	Latitude†	Longitude†	Method	n	σ_1	σ_2	σ_3	*F*	*R*
D201you	orthogneiss (K)*	31°28.4'	117°22.69'	NDA	10 10	118 19	346 63	215 19	24°	0.4
D201ys	volcanics			NDA	13 12	149 12	347 77	240 04	21°	0.6
D203old	orthogneiss (K)	31°03.43'	116°56.21'	NDA	13 12	007 47	182 43	274 02	16°	0.9
D204-1	orthogneiss (K)	31°04.4'	116°55.86'	NDA	22 21	228 03	212 80	319 10	09°	0.5
D204-2				NDA	17 16	292 10	123 79	022 02	10°	0.5
D205old	granitoid (K)	31°0.79'	116°57.51'	NDA	14 14	325 25	109 59	227 16	18°	0.6
D207old	syenite (K)	31°09.44'	117°00.86'	NDA	14 14	277 32	071 55	179 12	14°	0.6
D208o2	volcanics	31°16.25'	117°00.39'	NDA	6 6	097 36	259 52	001 08	11°	0.4
D208old				P-B-T	12 12	229 62	121 10	027 20		
D209dex	granitoid (K)	31°08.46'	117°00.51'	NDA	6 6	267 41	087 49	177 00	17°	0.6
D209old				NDA	8 8	352 00	261 85	082 05	16°	0.8
D213	orthogneiss (K)	31°08.67'	116°45.9'	P-B-T	7 7	220 03	116 79	322 10		
D214	subvolcanics	31°09.53'	116°46.25'	NDA	13 12	277 60	092 30	183 02	18°	0.7
D223old	granitoid (K)	31°47.33'	115°14.84'	NDA	11 11	118 30	283 59	024 07	19°	0.6
D225	basement (K)	31°27.52'	115°16.38'	grid	9 8	312 16	066 54	212 31	5°	0.3
D226	granitoid (K)	31°28.01'	115°18.90'	NDA	10 09	258 39	099 49	357 11	21°	0.5
D228XMF	*para/orthogneiss (pre-K)**	31°29 19'	115°19'	NDA	16 15	222 24	047 66	313 02	21°	0.6
D228YOU				NDA	7 6	243 85	091 04	001 02	09°	0.6
D228NW				NDA	7 7	122 20	228 38	011 46	17°	0.7
D230	orthogneiss (pre-K)	31°43.15'	114°52.95'	P-B-T	7 7	251 28	060 61	175 13		
D246-7-1	para/orthogneiss (K-reheat)*	30°49.16'	115°01.66'	NDA	12 12	217 37	054 52	313 08	19°	0.5
D246-7-2				NDA	12 12	029 84	287 01	197 06	22°	0.9
D256	granitoid (K)*	31°56.62'	113°38.56'	NDA	17 17	075 14	324 55	173 31	15°	0.4
D259	blueschist-marble (pre-K)	31°36.59'	113°57.08'	P-B-T	5 5	336 27	178 62	066 11		
D264o11	limestone (T)	30°10.47'	114°58.18'	NDA	13 13	253 12	093 77	344 04	15°	0.3
D264o12				NDA	18 18	299 05	181 79	030 10	24°	0.5
D264you				P-B-T	14 14	197 05	019 85	280 01		
D266old	granitoid(K)* - marble	30°13.13'	114°54.33'	P-B-T	15 15	252 27	033 56	154 19		
D266you				P-B-T	25 25	165 41	332 48	069 06	29°	0.8
D268-69o2	volcanoclastics	30°00.4'	114°43.08'	NDA	50 47	191 01	053 89	281 01	23°	0.5
D268-69o3				P-B-T	25 25	037 00	129 75	300 15		
D268-69you				NDA	29 29	064 16	228 73	333 04	19°	0.4
D270o1	granitoid (K)* - marble	29°59.91'	114°50.25'	NDA	19 18	196 09	053 79	287 06	20°	0.8
D270o3				P-B-T	6 6	097 28	226 50	344 21		
D270y				NDA	10 10	165 41	332 48	069 06	18°	0.6
D271-1	granitoid (K)-marble	30°04.86'	114°56.11'	NDA	24 24	034 14	149 59	297 27	18°	0.5
D271-2				NDA	14 13	068 11	174 53	330 34	25°	0.6
D271-3				NDA	9 9	103 74	226 09	318 13	17°	0.4
D272-1	limestone (T)	29°53.61'	115°10.63'	P-B-T	10 10	002 01	238 88	089 02		
D272-2				P-B-T	37 36	236 02	332 76	142 14		
D272-3				NDA	22 21	269 27	140 51	013 26	17°	0.4
D273-1	limestone (S)	29°43.5'	115°19.15'	P-B-T	8 8	207 05	307 61	115 28		
D273-2				P-B-T	5 5	267 07	046 81	195 08		
D277-280	basement (pre-K)	29°31.21'	116°03.01'	NDA	23 23	020 70	198 20	288 01	19°	0.6
D281-282a	basement-limestone	29°27.41'	115°52.84'	P-B-T	16 16	224 67	051 23	142 02		
D283-2	limestone	30°06.91'	116°02.99'	P-B-T	10 10	079 44	249 45	342 04		
D283-3				P-B-T	28 28	310 20	169 65	053 11		
D284-2	limestone	30°11.71'	116°06.39'	NDA	29 27	111 78	269 11	004 04	20°	0.6
D285you	limestone (Pe)	30°15.66'	115°23.34'	NDA	27 26	249 04	348 69	157 20	19°	0.3
D286old	basement (pre-K)	30°22.38'	116°18.63'	NDA	19 17	115 56	238 21	339 26	19°	0.7
D516tl	volcanics (K1)	31°43.140'	116°30.58'	NDA	12 12	159 38	338 52	068 00	19°	0.8
D516tlrot				P-B-T	12 12	216 71	333 09	065 18		
D533ns	basement (pre-K)	31°56.971"	114°38.55'	P-B-T	9 9	010 04	270 68	087 22		
D541old	Foziling (pre-K)	31°23.514'	116°09.66'	NDA	5 5	205 25	020 65	112 01	14°	0.4
D541middle				NDA	22 22	255 77	083 13	345 02	12°	0.2
D541young				NDA	15 15	135 85	313 05	043 00	16°	0.6

See Table 1 for explanation. Pe, Permian; S, Sinian.

* Radiometric dating available.

†No Global Positioning System (GPS) location data available for blank sites; see Figures 7-8 and 10-13 for locations.

subhorizontal NW-SE extension. At one locality, boudinaged amphibolite layers in a felsic gneiss record ~70% elongation along the stretching lineation.

Mafic dikes have not been studied in detail. They seem to be related to late stages in the deformation history, are not ductilely deformed, and probably intruded large-scale tension gashes of the ductile-brittle to brittle deformation (events 3 and 4 of Figure 6; D212-D214, Figure 7).

4.3. Southern Boundary of the Northern Orthogneiss Unit

NOU plutons intruded the UHP unit and show synmagmatic to postmagmatic deformation within distributed, generally NE trending shear zones (Figure 10). The regional confinement and en-échelon separation of the shear zones indicates that they are local boundaries, in contrast to the well-defined northern boundary of the NOU, the XMF. Locally, sills parallel the foliation and are extremely sheared. Overall, shear was normal or sinistral transtensive. As along the XMF, the strain/stress field shows clockwise rotation in time.

Along the eastern Yuexi-Shuihou transect (D70-D72, Figure 10), structures in the UHP paragneiss record early, Triassic top-to-NW shear [*Hacker et al.*, this issue] and discrete, Cretaceous normal shear and faulting, locally with cataclastic breccia. The Tuanling profile (D56-D60, D62-D69, and D88-D98) shows three zones of synmagmatic, high-T mylonitization distributing deformation over a wide zone. No ultramylonites are developed, but brecciation occurred during brittle-ductile deformation. Ninety percent of the rocks are plutons and dike rocks; migmatites are absent. This section probably represents a relatively deep crustal level (intrusion depth of the Tuanling tonalite ~20 km) with a high volume of intrusive rocks accommodating crustal extension. Quartz records high-T textures and complex kinematics; the samples are all dominated by prism <a> slip. The kinematics vary from pure shear in coarse-grained gneiss (DS78 and DS80) to distinctly noncoaxial in fine-grained, narrow, high-strain shear zones and shear bands (DS82a has relict, large grains showing recovery; DS82b,c are dynamically recrystallized small grains, and the shear band texture in DS82c may record a contribution of prism <c> glide). The westernmost transect (D90-D92) comprises transpressive sinistral shear (in contrast to the usual tensional character), locally overprinting an early, relict UHP fabric in amphibolite xenoliths and migmatites, with a premigmatization foliation (potassium feldspar granite leucosome). Shear criteria include en-échelon quartz veins, indicating deformation late in the history, and asymmetric north-vergent folds. The deformation at the western tip of the studied area (D105) shows north trending dextral and NE trending sinistral shear zones comprising generally coaxial NW-SE extension, reminiscent of structural geometries in the northeastern NOU.

4.4. UHP-HP Units: Central and Southern Dabie Shan

Cretaceous mesoscale faulting was widespread (Figure 11); the timing of this faulting is based on outcrops where faults overprint Cretaceous plutons or mineral fabrics with Cretaceous cooling ages (e.g., DS163, station D110). The faulting exhibits the clockwise stress field rotation typical for the Cretaceous event (Figure 6). N-S extension was accompanied by significant E-W contraction at several stations. The shear zones where low-T plastic deformation accompanied Cretaceous cooling indicate subhorizontal extension, locally with a noncoaxial top-to-SE shear component (Figure 11).

4.5. Northern Dabie Foreland

Deformation of the pre-Cretaceous basement complexes north of the XMF was complex and heterogeneous. Similar, albeit simpler structures occur in Cretaceous volcanic rocks (Figure 8). Variably oriented, though generally N-S, contraction was associated with two(?) stages of folding and, characteristically, with strong fold-axis-parallel approximately E-W extension. Contraction and extension directions seem to have rotated clockwise, with early NW-SE contraction associated with asymmetric folds and later NE-SW contraction related to flexural folding (Figure 8, D28). During this stage (ductile flow event and event 1 of Figure 6), dextral fault zones (D5, Figure 8) conjugate to the XMF developed. N-S and NE-SW extension, so prominent along the XMF (events 3 and 4, Figure 6), is sparsely recorded in the foreland. Early Cretaceous (K_1) volcanics (station D516, Figure 8) within the Hehuai basin north of the Dabie were deformed twice before the Tertiary overprint: Early E-W extension was followed by NW tilting and revived E-W extension.

4.6. Southern and Eastern Dabie Foreland

The largest set of our data stems from granodiorites and their sedimentary wall rocks (Figure 12). Deformation occurred during high- and low-T cooling dated at 143-136 Ma (Table 3). Tremolite fibers on mesoscopic fault planes in Early Triassic marble/limestone tie faulting to late-stage fluid activity in the skarns around the plutons. Early N(E)-S(W) shortening caused sinistral slip on NE trending and dextral slip on NW trending map-scale faults. Later, the slip sense reversed, and folding occurred, with fold-axis-parallel extension leading to boudinage (e.g., D121, Figure 12). The Lushan complex is an uplift of Yangtze basement southeast of the Dabie. Assuming that deformed late potassium feldspar granite veins in the Lushan are Cretaceous, as elsewhere in the Dabie and the southern foreland, low-T mylonites and brittle faults there record subhorizontal approximately E-W extension. Quartz + chlorite + epidote, low-grade transtensive shear and fault zones, bounding the complex to the east, are subparallel to the Tan-Lu. We collected a large data set on Cretaceous faulting in the foreland (S)E of the Dabie Shan; a few of these data are shown in Figure 12, and stress directions of stations close to the Dabie are summarized in Figure 6 ("eastern foreland fold-thrust belt" see *Schmid et al.* [2000] for a complete evaluation). Structures demonstrate an overall clockwise rotation of the subhorizontal compression and extension directions, and the deformation history is thus similar to the Dabie; however, the foreland has a clearer record of contraction.

4.7. Hong'an – Southern Tongbai Shan

Only reconnaissance data on Cretaceous deformation are available in Hong'an and Tongbai (Figure 13). In northeastern Hong'an, chloritized biotite orthogneiss, lacking white mica, and deformed pegmatite contrast with the UHP rocks of the Triassic Huwan detachment zone [*Webb et al.*, 1999a, 2000]; structures are subvertical, and displacement was sinistral transtensive. In the eastern Tongbai Shan is a broad dextral shear belt of orthogneiss, paragneiss, mylonite, and local ultramylonite of unknown width and along-strike length [*Webb et al.*, 2000]. To the west and south, these tectonites may be associated with sedimentary basins (K_2, according to *R.G.S. of Hubei*, [1990]), here speculatively interpreted as fault-related from the map-scale fault pattern (Figure 13). The northern area comprises voluminous

plutons and a gneiss-granite dike association reminiscent of the NOU (Figure 13), which contrasts with the UHP rocks of the Hong'an Shan to the east and the Paleozoic basement units north of the Triassic suture [*Hacker et al.*, this issue; *Zhai et al.*, 1998]. This belt seems to end abruptly in the east along fault/shear zones with unknown kinematics. We speculate that these are transtensional, with UHP rocks of the western Hong'an in the hanging wall and Cretaceous rocks in the footwall. Shear belt muscovite and biotite ages of 131 and 105 Ma [*Webb et al.*, 1999a], respectively, and zircon and hornblende ages of 132 and 130 Ma [*Ames et al.*, 1996; *Zhai et al.*, 1998], respectively, from a Cretaceous granite and a thermal aureole, demonstrate that magmatism, cooling, and deformation in the Tongbai were coeval with those in the NOU of the Dabie Shan.

At least locally, the shear belt was reactivated. Several rocks, deformed at the brittle-ductile transition, gave unexpectedly young $^{40}Ar/^{39}Ar$ ages (Figure 4a and Table 3). A pseudotachylite from a ductilely undeformed, but strongly faulted (sinistral, chloritized faults with millimeter-thick pseudotachylite), probably Cretaceous granite, D256c, was run in separate splits and suggests faulting at ~75 Ma. The individual step ages of D260c, biotite from a segregation vein in a ductile mylonite of the dextral shear belt, also scatter around 75 Ma, probably dating late-stage faulting. D253b biotite, from the faulted western edge of the Dawu dome (Figure 13), yielded a disturbed spectrum for which we adopt the total fusion age of 84 Ma. The two thermal events are best recorded by potassium feldspar, which indicates initial cooling prior to 90 Ma and reheating and cooling at ~75 Ma; these thermal events are accompanied by the two stages of deformation (dextral shear and sinistral faulting; see also Table 3 and *Webb et al.* [1999a]).

5. Tectonic Model and Exhumation

Figure 14a summarizes the proven and suspected structures of the ductile event and events 1-3 of the ductile to brittle deformation and their average strain/stress orientations. In detail, the incremental principal strain/stress axes rotated (Figure 6). However, we discuss these events together, as our dating does not allow more distinct age resolution. The rotation probably occurred in a progressive deformation field, as they are derived from a regionally consistent sequence of ductile to brittle deformation events active during regional cooling.

The syntectonic to posttectonic nature of the NOU orthogneisses testifies that gneissification was active from 137 to after 128 Ma. The occurrence of discrete shear zones, localizing deformation, implies that deformation continued thereafter and might locally have been active earlier. We argued in section 3.2. that the reheating of the UHP units at 150-130 Ma might have thermally weakened the Dabie crust to facilitate crustal extension locally; thus we tentatively adopt 140 Ma as the upper bound for the onset of large-scale deformation. The ductilely undeformed plutons forming the backbone of the NOU are as young as 125 Ma, demonstrating that deformation there was complete at that time. The Mozitang gabbro, which intruded at 129 Ma and cooled rapidly at 121 Ma from 500° to 300°C, may place a lower bound on deformation along the XMF. The gabbro depicts deformation during cooling from the melt stage to near-surface conditions. It is heterogeneously deformed and shows nearly undeformed portions, magmatically aligned hornblende, gneissic habit, mylonites with grainsize reduction of hornblende and plagioclase, chlorite-rich ultramylonites, faults planes with chlorite slickenlines, and local brecciation. From the hypersolidus to the brittle-ductile stage, the sense of displacement was transtensive. Together with the last occurrence of a structurally controlled cooling pattern in the Dabie (~120 Ma), the pulse of NOU-derived detrital grains in the foreland (123-119 Ma), and the regional initial K-feldspar cooling at ~118 Ma, this rapid cooling is taken to establish ~120 Ma as the lower bound for sinistral transtensional deformation.

During 140-120 Ma the XMF was principally a transtensional fault, and although based only on reconnaissance data, sinistral transtensional faulting probably occurred all along the northern Hong'an and Tongbai Shan. We cannot demonstrate that the Tan-Lu and the Shang-Ma faults were active at this time, as no high-grade mylonites of the appropriate strike were found along their Cenozoic traces. If these two faults were active, they would have been normal faults, probably with an early sinistral and a late dextral component imposed by the deformation fields documented elsewhere in Dabie. The southern boundary of the NOU is interpreted as a transtensional boundary subparallel to the XMF comprising several en-échelon, nearly normal shear segments. Speculatively, we assign the dextral motion along the southern Tongbai to this time period, forming a conjugate shear zone to the XMF. Together with the deformation along the northern Hong'an and Tongbai, these shear zones emphasize NW-SE stretch along the axis of the Qinling-Dabie orogen in the Early Cretaceous. Clearly, most of the crustal extension was accommodated during the 140-120 Ma period.

Next we argue that deformation migrated from SW to NE and that the XMF controlled the exhumation geometry. Suppose that a rolling hinge-isostatic rebound model (Figure 14b, e.g., *Wernicke and Axen* [1988]) applies, in which the NOU is exhumed as a distinctly asymmetric extensional structure. Footwall rocks (the NOU) flow SW along a subhorizontal detachment and undergo a subvertical simple shear (hanging wall toward the NW) along a ramp, the XMF. The fault flattens again where the footwall passes out from under the hanging wall, imposing shear of opposite sense. This conceptual model has the following implications for the NOU: (1) Foliations dip moderately to steeply along the XMF and flatten into the NOU. We constructed foliation trajectories along three NNW trending profiles in areas relatively unaffected by late-stage plutons; they show a convex upward shape (Figure 14c). (2) If injection, crystallization, and cooling of plutons are related to extension, the oldest plutons should crystallize shortly after initiation of deformation at relatively great depth (as heat has not yet been advected up strongly) and should occupy portions of the extensional terrane farthest away from the breakaway fault. Above we argued for a relatively early onset of deformation; our sparse geobarometry data indicate that the oldest intrusions generally were deepest (Figure 14d), and a plot of age versus distance from the XMF (Figure 14e) confirms that the plutons roughly are older toward the south (Figure 14e). (3) Late plutons should have crystallized relatively shallowly and close to the ramp, as the fastest advection of heat occurs there and rocks farther south would have cooled. Figure 14d suggests that the youngest intrusions reached relatively high crustal levels, and Figure 14c indicates that intrusion depths generally follow the foliation trajectories which were grossly subparallel to the isotherms. (4) Assuming that shear along the XMF controlled intrusion depth and that the plutons crystallized at approximately the same temperature, the age versus intrusion depth relationship should give an order-of-magnitude approximation of the tectonic exhumation rate. Figure 14d indicates that there may have been variable rates; the higher rates at ~126 Ma probably led to the

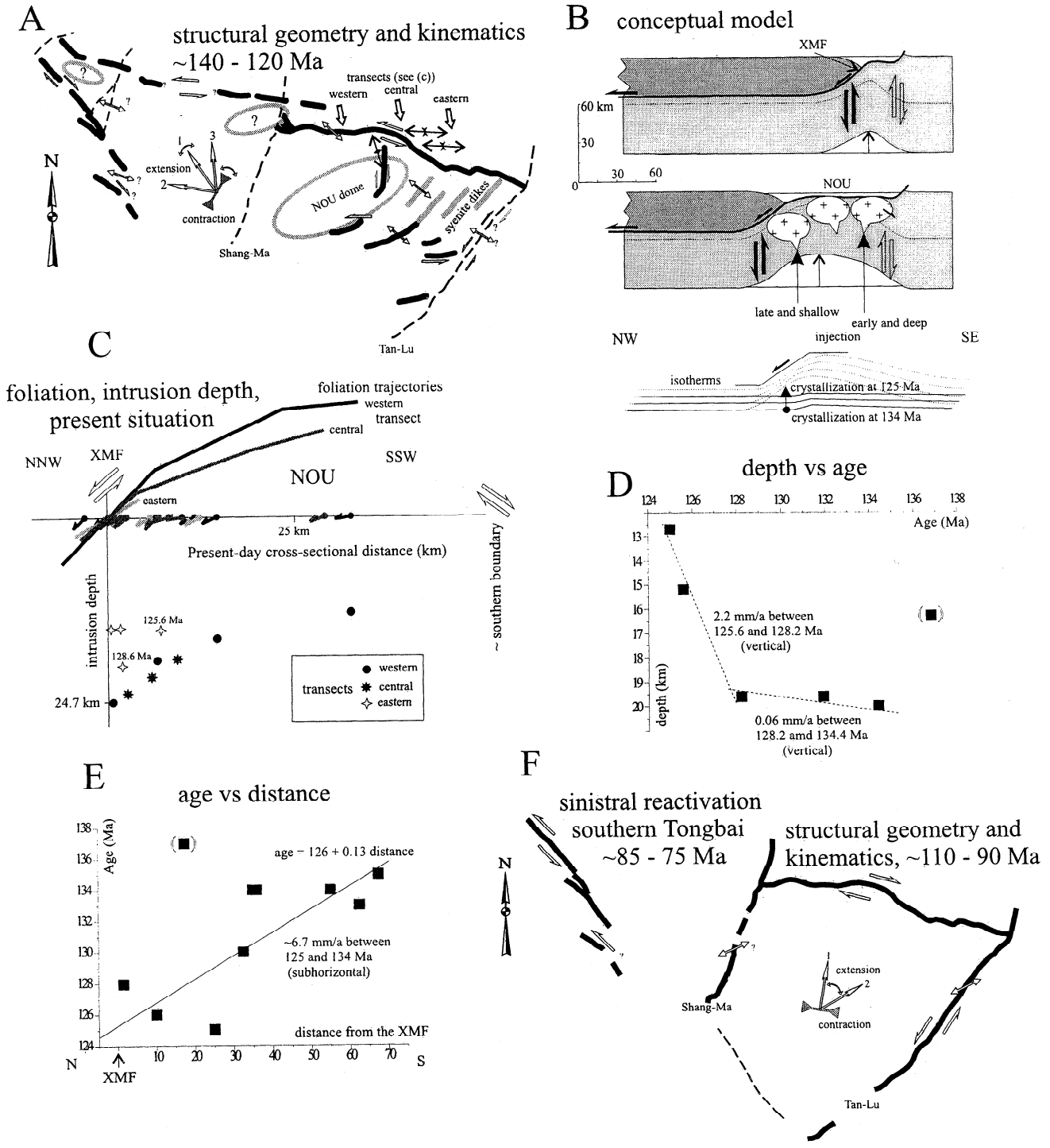

Figure 14. (a) Proven and suspected structures and their kinematics of the ductile event and events 1 to 3 of the ductile-to-brittle deformation (~140-120 Ma, see text), and their average strain/stress orientations (see Figure 6), summarized from our structural data (Figures 7-13). NOU, Northern Orthogneiss unit. Numbers 1-3 (older to younger) relate to the strain/stress field rotation deduced from the structural data. (b) Rolling hinge-isostatic rebound model (adopted from *Wernicke and Axen* [1988]) for structural geometry and exhumation of the Northern Orthogneiss unit (NOU) along the Xiaotian-Mozitang detachment fault (XMF) as a distinctly asymmetric extensional structure. Isotherm plot (lowermost diagram) illustrates change in crystallization depths in time due to advection of heat to shallower crustal levels by shear along the XMF. See text for discussion. (c) Foliation trajectories and intrusion depth of Northern Orthogneiss unit igneous rocks along three approximately NNW trending profiles from areas relatively unaffected by late-stage plutons (data from different profiles are shaded differently and marked west, central, and east; intrusion depth data are from Table 4, and the two crystallization ages are from *Hacker et al.* [1998]). (d) Crystallization ages of Northern Orthogneiss unit igneous rocks versus their intrusion depths (data are from Table 4 and U/Pb data summarized in Figure 3b and by *Hacker et al.* [1998]). The datum marked with a solid square in parentheses is excluded from the discussion due to its large uncertainty (±5.1 Ma) and its unusually large age difference from the hornblende $^{40}Ar/^{39}Ar$ age from the same sample (124 ± 1 Ma). (e) Crystallization age of Northern Orthogneiss unit igneous rocks versus their distance from the Xiaotian-Mozitang detachment fault (XMF). (f) As in Figure 14a, but for ~110-90 Ma and ~85-75 Ma (the latter ages only occur in the southern Tongbai Shan. See text for discussion.

episode of fast cooling at ~121 Ma along the XMF. (5) Assuming further that the age–distance relation (Figure 14c) was induced by slip along the XMF, an approximate rate of average subhorizontal displacement of 6-7 mm/yr is obtained. (6) Following the conceptual model further, the lower T, top-to-SE normal component of shearing/faulting, best defined along the southern margin of the NOU, may be related to the required opposite sense of shear (Figure 14b). (7) The zone close to the XMF has few undeformed plutons but shows intense deformation. Deformation concentrated at the northern margin of the NOU would have exhumed the plutons to the near surface by vertical thinning of their roofs. (8) The ~40 km normal displacement along the XMF obtained from the present geometry of the fault and differential exhumation across it comprises a minimum for subhorizontal extension during Cretaceous crustal thinning. Assuming that the NOU originated entirely in the Cretaceous yields a maximum value of ~70 km (100%) for subhorizontal crustal extension.

Between ~100 and 90 Ma the Dabie Shan was reactivated, and we relate the stress field summarized under event 4 (Figure 6) to this time. The XMF was dextral and conjugate to the sinistral Tan-Lu and Shang-Ma faults. We base our interpretation on the distinct reheating event concentrated along the Tan-Lu (and probably the Shang-Ma; Figure 5c) and the local observation of low-T ductile deformation and brecciation along the Tan-Lu. The reactivation is contemporaneous with the fault gouge dated at 90-110 Ma along a Tan-Lu strand far north of Dabie (see section 3.2.). Finally, the shear zone along the southern Tongbai Shan was active sinistrally between 85 and 75 Ma (Figure 14f).

The documented regional clockwise change in the orientation of the principal stresses (e.g., change of σ_3 along the XMF from early approximately E-W to late approximately NE-SW) very likely records a change in the regional stress field and not the rotation of a large crustal block. *Gilder and Courtillot* [1997] and *Gilder et al.* [1999] demonstrated that both the Sino-Korean and the Yangtze blocks lack paleomagnetically detectable internal block rotations since the Late Jurassic in the vicinity of the plate suture.

6. Time-Correlative Early Cretaceous Deformation in East China

Figure 15a summarizes recent data on the age and kinematics of Late Jurassic-Early Cretaceous deformation throughout eastern Asia. The most spectacular intracontinental deformation, the Yinshan fold belt, is slightly older (160-125 Ma) than widespread extension that is most spectacularly manifest in Cordilleran-type metamorphic core complexes from Mongolia to southeastern China [e.g., *Davis et al.*, 1996; *Webb et al.*, 1999b]. The extensional systems overprinting the Yinshanian thrusts and folds locally show an increase in cooling rates at ~118 Ma, possibly indicating rapid cooling after exhumation. As in the Tongbai and along the Tan-Lu, gouge ages (89-72 Ma; *Wang et al.* [1989] and *Davis et al.* [1996]) along the Hefangkou extensional detachment fault indicate late-stage reactivation. *Yin and Nie* [1996] and *Davis et al.* [1996, 1998] speculated that the enigmatic Yinshan belt originated from compressional intraplate stresses transmitted from the Siberian-Mongolia–Sino-Korean collision (Mongol-Okhotsk suture) superimposed onto thermally weakened crust caused by synchronous, westward Pacific subduction and attendant magmatism; they did not report a genetic association between the normal and thrust fault systems.

Further Early Cretaceous deformation supported by geochronology comprises the following: (1) *Reischmann et al.* [1990] dated the Shagou shear zone, a branch of the Shangdan fault zone in the Qinling belt, at ≥126 ± 9 Ma. (2) Cooling through 400°-300°C at 120-130 Ma may indicate Cretaceous deformation in the Longmen Shan [*Arne et al.*, 1997]. (3) Triassic deformation along the northeastern margin of Indochina was reactivated by dextral(?) strike-strike slip shear [*Lepvrier et al.*, 1997] with cooling through 400°-300°C at 130-90 Ma. (4) The western boundary of Indochina shows Late Jurassic-Early Cretaceous contraction, e.g., along the Pak Lay fold belt [e.g., *Stokes et al.*, 1996]. (5) *Webb et al.* [1999b] reported syn-kinematic biotite ages of 129-126 Ma from a southern Mongolian metamorphic core complex. (6) The Liaoning extensional detachment (east of Bohai Bay) cooled through 400°-300°C between 150 and 110 Ma [*Yin and Nie*, 1996]. (7) Normal faults in northern Jiangsu and southern Shandong (Jiaonan area), partly at the top of the Sulu UHP rocks, were active between 140 and 105 Ma [*Chen et al.*, 1992; *Yang et al.*, 2000]. (8) Final doming, and possibly formation of several core complexes in southeastern China, was Early Cretaceous [*Faure et al.*, 1996]. (9) Sedimentation of Late Jurassic-Early Cretaceous, mostly coarse clastics in several NE trending basins marks extension in eastern and northeastern China [e.g., *Watson et al.*, 1987].

7. Plate Tectonic Framework for Cretaceous Reactivation of the Qinling-Dabie Belt

Building on, but refining, the eastern Asian tectonic setting proposed by *Yin and Nie* [1996], we suggest that Cretaceous deformation in eastern Asia was the result of the combined effects of (1) the Siberia-Mongolia–Sino-Korean collision, (2) the Lhasa-West Burma(?Sibumasu)–Qiangtang-Indochina collision, (3) Pacific subduction, and (4) related magmatism.

1. The ocean separating Siberia from the combined Mongolia–Sino-Korean blocks closed in the Middle and Late Jurassic, forming the Mongol-Okhotsk suture. Crustal contraction probably lasted into the Early Cretaceous when the thickened fold-and-thrust belt was overprinted by normal faulting [e.g., *Zorin*, 1999; *Enkin et al.*, 1992].

2. The Lhasa–Qiangtang collision is well dated at latest Jurassic-earliest Cretaceous [e.g., *Allegre et al.*, 1984]; convergence continued until the early Late Cretaceous [*Murphy et al.*, 1997]. It is unclear whether the Sibumasu block was the eastern continuation of the Lhasa block [e.g., *Yin and Nie*, 1996] or was a separate block and collided earlier [e.g., *Enkin et al.*, 1992].

3. Figure 15b summarizes convergence vectors for northwestern Pacific Cretaceous subduction [*Engebretson et al.*, 1985]. Two events may have had an effect on the eastern Asia continental margin: (1) a change in the Early Cretaceous from a transcurrent to a convergent plate boundary with a high convergence velocity; possibly young oceanic lithosphere was subducted, as the spreading ridge between the Farallon and Izanagi plates probably was in the westernmost Pacific. (2) A change in the Late Cretaceous from a left-lateral convergent to frontal convergent plate boundary with reduced convergence rates.

4. Mesozoic calc-alkaline volcanic rocks and granites in southeastern China occur in belts and are between 145 and 85 Myr old (Figure 15c; *Zheng* [1985] and *Lapierre et al.*, [1997]). Although late Mesozoic granitoids occur in the entire region of

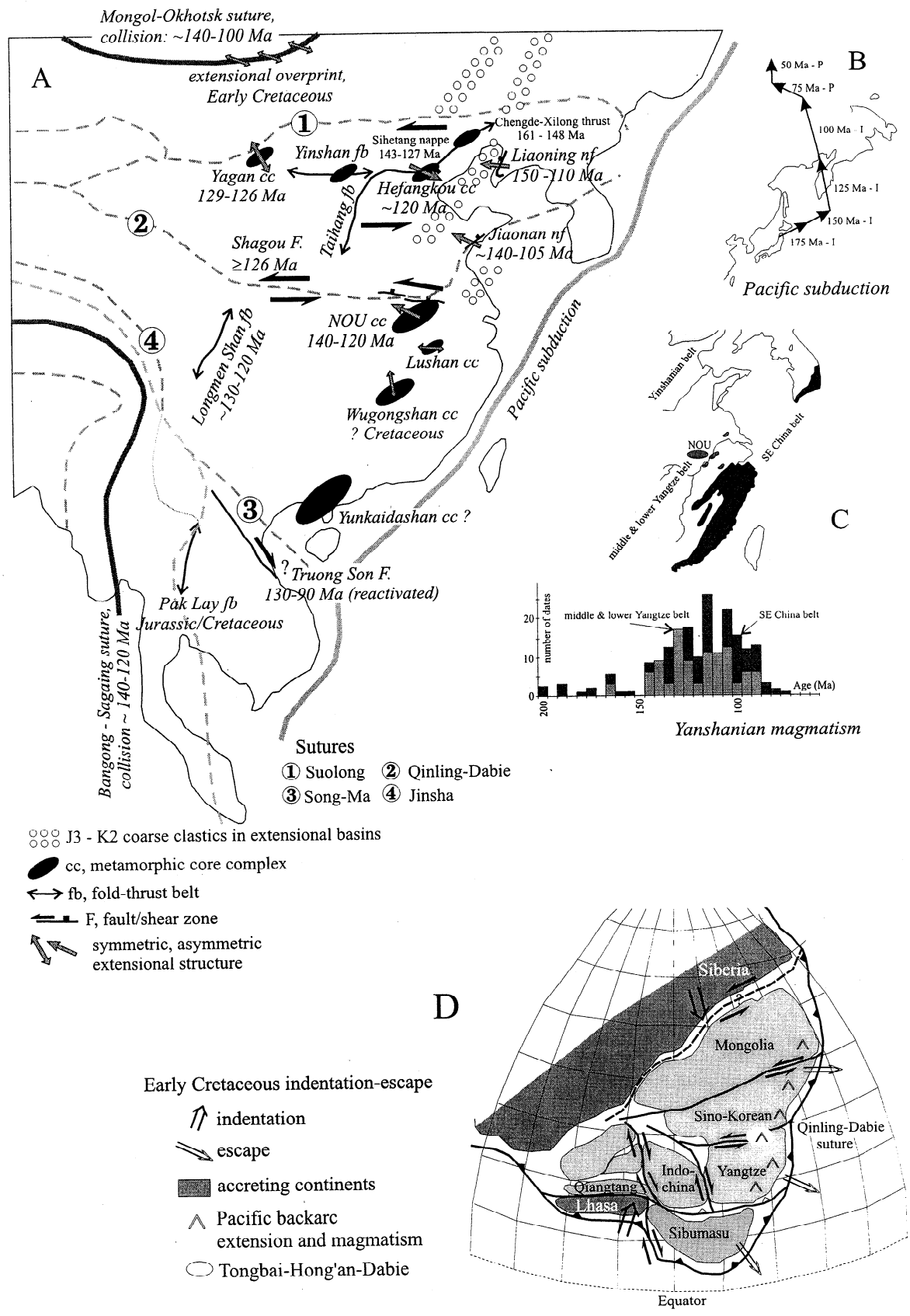

Figure 15. (a) Recent data on the age and kinematics of Late Jurassic-Early Cretaceous deformation in eastern Asia, after the references in the text. (b) Convergence vectors for the northwestern Pacific Cretaceous subduction [data from *Engebretson et al.*, 1985]. (c) Mesozoic calc-alkaline volcanic rocks and granites in southeastern China and their age distribution; data from *Zheng* [1985] and *Lapierre et al.* [1997]. (d) Possible Late Jurassic-Early Cretaceous tectonic scenario placed upon the Early Cretaceous paleomagnetic reconstruction of Asia [*Enkin et al.*, 1992]. Overall, this fits to an Early Cretaceous setting dominated by tectonic escape and Pacific backarc extension. See text for discussion.

southeastern China (but without firm age constraints), the principal occurrences are found in the Tongbai-Hong'an-Dabie area, in the eastern part of the Yangtze block, and in eastern Zhejiang. Isotopic features indicate that remelting of ancient lower continental crust may be the dominant source for these plutonic rocks [*Chen and Jahn,* 1998; *Ames et al.,* 1996].

Figure 15d places our data on reactivation of the Qinling-Dabie belt into a plate tectonic framework, based on the Early Cretaceous paleomagnetic reconstruction of Asia [*Enkin et al.,* 1992]. Overall, this fits to an Early Cretaceous setting dominated by tectonic escape and backarc extension and to a mid-Cretaceous setting dominated by Pacific subduction. Following *Yin and Nie* [1996] and *Davis et al.* [1998], the primary cause for the Yinshan fold belt probably was the Siberia-Mongolia–Sino-Korean collision. Contractional deformation in SE Asia probably resulted from the Lhasa-?Sibumasu–Qiangtang-Indochina collision. It has been demonstrated that in Cenozoic Asia and the Cenozoic Alps-Carpathians [*Tapponnier et al.,* 1986; *Ratschbacher et al.,* 1991], initial frontal shortening was followed by prolonged contraction with a component of eastward motion of triangular wedges, whose boundaries were mostly reactivated preexisting lithospheric heterogeneities. If this is true for the Early Cretaceous of Asia, the structures defining this extrusion would include proven or assumed sinistral slip components along the Suolong suture and the Qinling-Dabie suture, and dextral slip along the Song-Ma suture (Figure 15a; *Davis et al.* [1998], this paper and *Lepvrier et al.* [1997]). The interaction with Pacific backarc extension and the possible radial escape of the wedges to the weak subduction boundaries in the east and southeast imposed extension in eastern China, spectacularly manifest in the metamorphic core complexes, locally with documented sinistral transtension. The pivot for the escaping Yangtze block, for example, would be the junction between the Jinsha–Song-Ma and the Qinling-Dabie sutures.

Our model also explains why Pacific magmatism reached so far into the continental interior and why it did so particularly along west trending zones: It followed active deformation zones. It may also explain two prominent Hong'an-Dabie features. First, the change from highly oblique to orthogonal Pacific subduction in the Late Jurassic (Figure 15b) and the resultant magmatism with its spectacular onset at ~145 Ma in eastern China (Figure 15c) may have caused the documented reheating of the Hong'an-Dabie UHP units and may thus have facilitated crustal extension commencing at ~140 Ma. Rapid subduction of young ocean crust might have carried the heat source far into the continental interior. We suggest that Pacific subduction was the major source for the magmatic rocks of Hong'an-Dabie and/or it provided the heat source for partial melting of a Triassic-Jurassic lithospheric root, which might have existed before the Cretaceous extension and magmatism [cf. *Jahn et al.,* 1999]. Second, the XMF seems to be a first-order example of the reactivation of lithospheric heterogeneities. Here, we documented that the Huwan detachment zone was reactivated in the Cretaceous; in the northern Dabie this Triassic lithospheric normal fault zone exhuming the UHP continental crust [*Hacker et al.,* this issue] must have run between the central Dabie UHP units and the basement units of the Dabie foreland, the Foziling and Luzhenguang units, i.e., most probably along the XMF (Figure 1). Similarly, the Cenozoic Jinzhai fault reactivated the Triassic suture for a considerable stretch in the Tongbai-Hong'an-Dabie (Figure 1).

After the Early Cretaceous event, a compound of several plate boundary processes, later events probably were caused more by pure Pacific backarc extension, dominant since about the mid-Cretaceous. Then, continental-margin-parallel faults were reactivated or developed as normal faults. Oblique subduction may have imposed the sinistral slip components along, e.g., the Tan-Lu, Lishui-Haifong, and Changle-Nanao faults [e.g., *Faure et al.,* 1996], as predicted by the model of slip partitioning along oblique plate boundaries [*McCaffrey,* 1996]. The decrease in convergence may relate to a net reduction in horizontal compressional stress transmitted between the Izanagi–Pacific and Eurasian plates, which may have resulted in increased extension rates along the adjacent continental margin.

8. Conclusions

A minimum extension of 18% (≥5.4 km dip slip along and ≥4 km throw across the Tan-Lu) occurred across the Cenozoic foreland basin east of the Dabie, and this constrains Cenozoic denudation of the Dabie Shan to ≤5 km. The sinistral Jinzhai fault zone, crossing the northern margin of the Hong'an-Dabie, the normal Tan-Lu fault zone, marking the eastern edge of Dabie, and a sinistral fault zone in the southern Tongbai and Hong'an are the major Cenozoic features of the Tongbai-Hong'an-Dabie portion of the Qinling-Dabie orogenic belt. The documented Cenozoic faulting emphasizes the difference between strike-slip-dominated tectonics along the Qilian-Qinling-Dabie belt and dominant rifting in north China.

Cretaceous plutons comprise 47% of the surface exposure of Dabie, and almost the entire northern Dabie consists of Cretaceous plutons and orthogneisses constituting the Northern Orthogneiss unit (NOU). The Cretaceous overprint diminishes westward in the Hong'an area where Cretaceous granitoids are concentrated along the northern boundary (20% of surface exposure). The Cretaceous overprint precludes any major preservation of the lithospheric structure of the Triassic UHP orogen. The NOU contrasts with the UHP-HP units in southern Dabie and in Hong'an and is characterized by its intermediate-composition plutonic rock assemblage, its fault-bounded structural setting, and its Cretaceous age. Intrusion-deformation relationships indicate that at least some plutons at the core of the NOU were deformed in a hypersolidus state. Plutonism occurred in the northern Dabie from 137 to 125 Ma, and mineral cooling ages define a thermal dome around these zircon ages. This period also marks the last time that the UHP rocks were at temperatures >300°C. The Xiaotian-Mozitang fault (XMF) imposed the major control on cooling, and its structural effect vanished after 120 Ma. The rocks of the NOU were exhumed from an average depth of 18 km (5.1 kbar) and Cretaceous plutons intruded up to 15 km deeper in the UHP-HP units than in the NOU. The maximum Cretaceous exhumation was ~30 km. Isotherms and isobars are both normal to the principal extension direction of Cretaceous crustal extension, and thus exhumation, magmatism, and cooling were controlled by deformation.

Cretaceous structures are dominantly strike-slip and normal faults. The major crust-shaping event was the formation of the magmatic-metamorphic-structural dome of the NOU under general NW-SE subhorizontal extension and NE-SW contraction with the activation of the XMF detachment fault. The characteristic regional feature is a general clockwise change in the orientation of the subhorizontal strain/stress axes, i.e., a change in extension from early NW-SE to intermediate N-S to late, subordinately developed, NE-SW. Cretaceous mesoscale faulting was widespread also in the UHP units and the forelands.

Reheating of the UHP units at 150-130 Ma might have thermally weakened the Dabie crust to locally facilitate crustal extension. Together with constraints from the NOU, this establishes ~140 Ma as the upper bound for the onset of large-scale deformation. Together with the last occurrence of a structurally controlled cooling pattern in the Dabie (~120 Ma), a pulse of NOU-derived detrital grains in the foreland (123-119 Ma), and the regional initial K-feldspar cooling at ~118 Ma, rapid cooling along the XMF at ~121 Ma establishes ~120 Ma as the lower bound for the sinistral transtensional deformation.

A rolling hinge-isostatic rebound model is suggested, which fits the distinctly asymmetric exhumation of the NOU. Deformation migrated from SW to NE, and the XMF controlled the exhumation geometry of the NOU. Applying this model to the age, intrusion depth, and structural geometry data suggests variable exhumation rates as high as 2 mm/yr and a rate of subhorizontal extension of up to 6 mm/yr. Between ~100 and 90 Ma the Dabie was reactivated, and the XMF was presumably dextral and conjugate to the sinistral Tan-Lu and Shang-Ma faults. The reactivation was contemporaneous with fault gouge dated at 90-110 Ma along a Tan-Lu strand far to the north of the Dabie. A last pre-Cenozoic deformation occurred in southern Tongbai between 85 and 75 Ma; it was contemporaneous with late-stage deformation along the Yinshan belt in northern China and had a similar NW-SE extension direction.

Early Cretaceous deformation in eastern Asia, coeval with that in Hong'an-Dabie, occurred in the intracontinental Yinshan fold belt, along the Shagou shear zone in the Qinling belt, along the Longmen Shan at the eastern termination of the Tibet plateau, along the margins of the Indochina block, along the Liaoning extensional detachment east of Bohai Bay, at the top of the Sulu UHP rocks in northeastern China, within several core complexes from Mongolia to southeastern China, and within a number of basins in eastern and northeastern China. Refining earlier models, we suggest that Cretaceous deformation in eastern Asia was the result of the combined effects of (1) the Siberia-Mongolia–Sino-Korean blocks collision, (2) the Lhasa-West Burma (?Sibumasu)–Qiangtang-Indochina collision, (3) Pacific subduction, and (4) related magmatism. This overall plate tectonic framework indicates an Early Cretaceous tectonic setting dominated by eastward tectonic escape and Pacific backarc extension and a mid-Cretaceous setting dominated by Pacific subduction. The change from transcurrent to frontal convergent Pacific subduction in the Late Jurassic and the resultant magmatism with its onset at ~145 Ma in eastern China may have caused the reheating of the Hong'an-Dabie UHP units and thus facilitated crustal extension. The XMF and Jinzhai fault zones provide first-order examples of reactivated lithospheric heterogeneities. The Triassic Huwan detachment zone, which exhumed the UHP continental crust, coincides in the Dabie with the NOU, and most probably with the XMF. Similarly, the Cenozoic Jinzhai fault reactivated the Triassic suture for a considerable stretch in the Tongbai-Hong'an-Dabie.

Appendix 1: Diffusion-Domain K-Feldspar Thermochronology

We ran modified 1997 versions of *Lovera's* [1992] modeling routines. A minimum of four age steps from a spectrum were fit with a line to define activation energy E and frequency factor D_0 [*Lovera et al.*, 1997]; more steps were added if the fit improved. The number of domains was limited to a minimum of three and a maximum of eight. The diffusion-domain theory predicts constant or monotonically increasing age spectra, and spectra that do not fit this ideal must be adjusted. Step ages were assigned 2σ analytical uncertainties, except for step ages younger than previous steps, for which the uncertainties were expanded until adjacent steps were concordant. In addition, multiple isothermal, low-temperature steps designed to identify Cl-correlated excess ^{40}Ar [*Harrison et al.*, 1994] were all assigned the age of the youngest step in the group. Steps above melting (>1100°C) that yielded spurious ages were either ignored or made the same as the final 1100°C step, and steps with low radiogenic yields (<95%) and anomalously old ages were adjusted to provide a smoothly increasing trend. Whereas steps collected at temperatures >1100°C are not modeled by the program, adjusting anomalously old step ages with low radiogenic yields has no phenomenological justification. Fifty monotonic and nonmonotonic cooling histories were generated using age spectrum modeling routines; unless otherwise noted, we only show cooling histories that provide a good fit to the data. Cooling histories were calculated from initial ages 50-100 Ma older than the oldest step.

Appendix 2: Methods of Fault Slip Analysis and Definition of Stress Tensor Groups

In the course of our structural studies, fault slip data were collected from outcrops of known or assumed stratigraphic position. Each station is an outcrop of up to quarry size with uniform lithology. Sense of slip along the faults was deduced from kinematic indicators, e.g., offset markers, fibrous minerals (mostly calcite and quartz) grown behind fault steps, Riedel shears, tension gashes, and slickenlines [e.g., *Petit et al.*, 1983]. Because errors in slip sense determination may have severe effects on the calculation of principal stress axes, a confidence level was assigned to each slip sense datum. These levels are recorded in the style of the arrowheads expressing the slip direction of the hanging wall block in the fault slip data diagrams, thus allowing judgment of the quality of the database. Surface morphology of the slickensides (e.g., fiber- or stylolite-coated or polished) and fault size, classified qualitatively based on an estimate of the displacement and the lateral extent of the fault, were recorded. The aim was to discriminate first-order faults and to enable a comparison of faults measured in outcrops with those inferred from mapping. Indications of multiple slip were recorded, and the relative chronology was used for separation of heterogeneous raw data fault sets into subsets. Overprinting relationships such as consistent fault superposition, overgrowths of differently oriented fibers, or fibers with changing growth direction guided the assignment of the subsets to relative age groups. The raw data usually contain several fault slip sets with incompatible slip sense but with consistent fault superposition, which were used as the geological constraint for separation. Note, however, that the subsets may contain incompatible data. The latter are included in the stereograms but excluded from the calculations of the stress axes. The derivation of an absolute chronology of faulting events is based on the relationship of faulting to the known age of a rock (e.g., Tables 1 and 5) or to the absolute age of its last metamorphism; our geochronological data are summarized in this paper and its companion [*Hacker et al.*, this issue].

We used the computer program package of *Sperner et al.* [1993] and *Sperner and Ratschbacher* [1994] for fault slip analysis to calculate the orientation of principal stress axes and the reduced stress tensors [e.g., *Angelier*, 1984]. Out of this package

we obtained stress axes by the "pressure-tension (P-B-T) axes" method [*Turner*, 1953] and calculated stress tensors by the "numerical dynamic analysis" of *Spang* [1972] and the "grid search" technique of *Hardcastle* [1989]. In addition to stress orientation the computation of the reduced stress tensor determines the ratio R, which expresses the relationship between the magnitudes of the principal stresses. Extreme values of R correspond to stress ellipsoids with $\sigma_2 = \sigma_3$ ($R = 0$) or $\sigma_1 = \sigma_2$ ($R = 1$). The quality and the quantity of field data determined the selection of the method used for calculation. The P-B-T axes method was used with scarce data and where insufficient time was available in the field for careful analysis of fault and striae characteristics. A comparison of methods is given by *Ratschbacher et al.* [1993]. The distance-weighting method of *Lee and Angelier* [1994] was employed to produce regional stress trajectories from multiple local stress orientation determinations.

Acknowledgments. This research was funded by DFG grants Ra442/4, Ra442/9, and Ra442/14 and NSF grant EAR-9417958. K-feldspar modeling made use of Frank Spera's IBM 43P computer in the Magma Dynamics Laboratory at UCSB. We thank Dave Rowley, the Stanford Asia group, Jens and Robert Schmid, Ines Gaitzsch, and numerous Chinese colleagues for discussion and field guidence. Hagen Deckert and Johannes Pic are thanked for transferring some data into computer graphics, and Gerold Zeilinger and Jürgen Elias contributed by U-stage work. Jens Schmid provided a helpful presubmission review. Bor-ming Jahn is thanked for sending a stimulating "in press" paper. Last but not least a "thank you" is given to the journal reviewers Denis Gapais, Roberta Rudnick, and An Yin for their educating comments!

References

Allègre, C.J., et al., Structure and evolution of the Himalaya-Tibet orogenic belt, *Nature, 307*, 17-22, 1984.

Ames, L., G. Zhou, and B. Xiong, Geochronology and geochemistry of ultrahigh-pressure metamorphism with implications for collision of the Sino–Korean and Yangtze cratons, central China, *Tectonics, 15*, 472-489, 1996.

Angelier, J., Tectonic analysis of fault slip data sets, *J. Geophys. Res., 89*, 5835-5848, 1984.

Angelier, J., Fault slip analysis and paleostress reconstruction, in *Continental Deformation*, edited by P.L. Hancock, pp. 53-100, Pergamon Press, Tarrytown, N.Y., 1994.

Arne, D., B. Worley, Ch. Wilson, S.F. Chen, D. Foster, Z.L. Luo, S.G. Liu, and P. Dirks, Differential exhumation in response to episodic thrusting along the eastern margin of the Tibet plateau, *Tectonophysics, 280*, 239-256, 1997.

Bellier, O., P. Vergely, J.L. Mercier, C.Z. Ning, N.G. Deng, M.C. Yi, and C.X. Long, Analyse tectonique et sedimentaire dans les monts Li Shan (province du Shaanxi – Chine du Nord): datation des regimes tectoniques extensifs dans le graben de la Weihe, *Bull. Soc. Geol. Fr., 162*, 101-112, 1991.

Blumenfeld, P., D. Mainprice, and J.-L. Bouchez, C-slip in quartz from subsolidus deformed granite, *Tectonophysics, 127*, 97-115, 1986.

Blundy, J.D., and T.J.B. Holland, Calcic amphibole equilibria and a new amphibole plagioclase geothermometer, *Contrib. Mineral. Petrol., 104*, 208-224, 1990.

Bouchez, J.L., C. Delas, G. Gleizes, and A. Nedelec, Submagmatic micro-fractures in granites, *Geology, 20*, 35-38, 1992.

Chen, J., and B. Jahn, Crustal evolution of southeastern China: Nd and Sr isotopic evidence, *Tectonophysics, 284*, 101-133, 1998.

Chen, W., Q. Li, D. Li, and X. Wang, Geochronological implications of K/Ar isotope system of fault gouge: A preliminary study, *Phys. Chem. Earth, 17*, 17-23, 1989.

Chen, W., T.M. Harrison, M.T. Heizler, R. Liu, B. Ma, and J. Li, The cooling history of melange zone in north Jiangsu–south Shandong region: Evidence from multiple diffusion domain ^{40}Ar-^{39}Ar thermal geochronology, *Acta Pet. Sin., 8*, 1–17, 1992.

Davis, G.A., X. Qian, Y. Zheng, H. Yu, C. Wang, Mao T.H., G.E. Gehrels, S. Muhammad, and J.E. Fryxell, Mesozoic deformation and plutonism in the Yunmeng Shan: A Chinese metamorphic core complex north of Beijing, China, in *The Tectonic Evolution of Asia*, edited by A. Yin and T.M. Harrison, pp. 253-280, Cambridge Univ. Press, New York, 1996.

Davis, G.A., C. Wang, Y. Zheng, J. Zhang, Ch. Zhang, and G.E. Gehrels, The enigmatic Yinshan fold-and-thrust belt of northern China: New views on its intraplate contractional styles, *Geology, 26*, 43-46, 1998.

Dell'Angelo, L.N., and J. Tullis, Fabric development in experimentally sheared quartzites, *Tectonophysics, 169*, 1-21, 1989.

Eide, L., M.O. McWilliams, and J.G. Liou, ^{40}Ar/^{39}Ar geochronologic constraints on the exhumation of HP-UHP metamorphic rocks in east-central China, *Geology, 22*, 601–604, 1994.

Engebretson, D.C., A. Cox, and R.G. Gordon, Relative motion between oceanic anc continental plates in the Pacific basin, *Spec. Pap. Geol. Soc. Am., 206*, 1-55, 1985.

Enkin, R.J., Z. Yang, Y. Chen, and V. Courtillot, Paleomagnetic constraints on the geodynamic history of major blocks of China from Permian to Present, *J. Geophys. Res., 97*, 13,953-13,989, 1992.

Faure, M., Y. Sun, L. Shu, P. Monie, and J. Charvet, Extensional tectonics within a subduction-type orogen: The case study of the Wugongshan dome (Jiangxi Province, southeastern China), *Tectonophysics, 263*, 77-106, 1996.

Fletcher, C.J.N., W.R. Fitches, C.C. Rundle, and J.A. Evans, Geological and isotopic constraints on the timing of movement in the Tan-Lu fault zone, northeastern China, *J. Southeast Asian Earth Sci., 11*, 15-22, 1995.

Gilder, S.A., and V. Courtillot, Timing of the North-South China collision from new middle to late Mesozoic paleomagnetic data from the North China Block, *J. Geophys. Res., 102*, 17,713-17,727, 1997.

Gilder, S.A., P.H. Leloup, V. Courtillot, Y. Chen, R.S. Coe, X. Zhao, W. Xiao, N. Halim, J.-P. Cogné, and R. Zhu, Tectonic evolution of the Tancheng-Lujiang (Tan-Lu) fault via Middle Triassic to Early Cenozoic paleomagnetic data, *J. Geophys. Res., 104*, 15,365-15,390, 1999.

Hacker, B.R., and Q.C. Wang, Ar/Ar geochronology of ultrahigh-pressure metamorphism in central China, *Tectonics, 14*, 994–1006, 1995.

Hacker, B.R., L. Ratschbacher, L. Webb, and S. Dong, What brought them up? Exhumation of the Dabie Shan ultrahigh-pressure rocks, *Geology, 23*, 743-746, 1995.

Hacker, B.R., X. Wang, E.A. Eide, and L. Ratschbacher, Qinling–Dabie ultrahigh-pressure collisional orogen, in *The Tectonic Evolution of Asia*, edited by A. Yin and T.M. Harrison, pp. 345-370, Cambridge Univ. Press, New York, 1996.

Hacker, B.R., L. Ratschbacher, L. Webb, T. Ireland, D. Walker, and S. Dong, U/Pb zircon ages constrain the architecture of the ultrahigh-pressure Qinling–Dabie Orogen, China, *Earth Planet. Sci. Lett., 161*, 215–230, 1998.

Hacker, B.R., L. Ratschbacher, L.E. Webb, M. McWilliams, T. Ireland, S. Dong, A. Calvert, H.-R. Wenk, and D. Chateigner, Exhumation of the ultrahigh-pressure continental crust in east central China: Late Triassic–Early Jurassic tectonic unroofing, *J. Geophys. Res.*, this issue.

Han, J., S. Zhu, and S. Xu, The generation and evolution of the Hehui basin, in *Sedimentary Basins of the World*, vol. 1, edited by X. Zhu, pp. 125-135, Elsevier Sci., New York, 1989.

Hardcastle, K.C., Possible paleostress tensor configurations derived from strike-slip data in eastern Vermont and western New Hampshire, *Tectonics, 8*, 265-284, 1989.

Harrison, T.M., M.T. Heizler, O.M. Lovera, C. Wenji, and M. Grove, A chlorine disinfectant for excess argon released from K-feldspar during step heating, *Earth Planet. Sci. Lett., 123*, 95-104, 1994.

Hibbard, M.J., Deformation of incompletely crystallized magma systems: Granite gneisses and their tectonic implications, *J. Geol., 95*, 543-561, 1987.

Hollister, L.S., G.C. Grissom, E.K. Peters, H. Stowell, and V.B. Sisson, Confirmation of the empirical correlation of Al in hornblende with pressure of solidification of calcalkaline plutons, *Am. Mineral., 72*, 231-239, 1987.

Jahn, B., F. Wu, Ch.-H. Lo, and Ch.-H. Tsai, Crust-mantle interaction induced by deep subduction of the continental crust: Geochemical and Sr-Nd isotopic evidence from post-collisional mafic-ultramafic intrusions of the northern Dabie complex, central China, *Chem. Geol., 157*, 119-146, 1999.

Lapierre, H., B.M. Jahn, J. Charvet, and Y.W. Yu, Mesozoic felsic arc magmatism and continental olivine tholeiites in Zhejiang province and their relationship with the tectonic activity in southeastern China, *Tectonophysics, 274*, 321-338, 1997.

Lee, J.C., and J. Angelier, Paleostress trajectory maps based on the results of local determinations: The "LISSAGE" program, *Comput. Geosci., 20,* 161-191, 1994.

Lepvrier, C., H. Maluski, N. Van Vuong, D. Roques, V. Axente, and C. Rangin, Indosinian NW-trending shear zones within the Truong Son belt (Vietnam): $^{40}Ar/^{39}Ar$ Triassic ages and Cretaceous to Cenozoic overprints, *Tectonophysics, 283,* 105-127, 1997.

Li, S.G., S.R. Hart, S.G. Zheng, D.L. Liu, G.W. Zhang, and A.L. Guo, Timing of collision between the north and south China blocks: The Sm-Nd isotopic age evidence, *Sci. China Ser. A, 32,* 1393-1400, 1989.

Li, S., et al., Collision of the North China and Yangtze blocks and formation of coesite-bearing eclogites: Timing and processes, *Chem. Geol., 109,* 89–111, 1993.

Lin, A., T. Miyata, T. Wan, Tectonic characteristics of the central segment of the Tancheng-Lujiang fault zone, Shandong Peninsula, eastern China, *Tectonophysics, 293,* 85-104, 1998.

Liou, J.G., R.Y. Zhang, E.A. Eide, S. Maruyama, X. Wang, and W.G. Ernst, Metamorphism and tectonics of high-P and ultrahigh-P belts in Dabie-Sulu Regions, eastern central China, in *The Tectonic Evolution of Asia*, edited by A. Yin and T.M. Harrison, pp. 300-343, Cambridge Univ. Press, New York, 1996.

Lu, Y., J. Ren, S. Li, X. Cui, and B. Li, Depositional sequences of the Yitong graben and its response to transform-extensional processes, *Tectonophysics,* in press, 2000.

Lovera, O.M., Computer program to model $^{40}Ar/^{39}Ar$ diffusion data from multidomain samples, *Comput. Geosci., 18,* 789-813, 1992.

Lovera, O.M., M. Grove, T.M. Harrison, and K.I. Mahon, Systematic analysis of K-feldspar $^{40}Ar/^{39}Ar$ step heating results; I, Significance of activation energy determinations, *Geochim. Cosmochim. Acta, 61,* 3171-3192, 1989.

Ma, Ch., C. Ehlers, K. Yang, CH. Xu, and A. Lindroos, Regional exhumation and thermal history of the Dabieshan high-pressure and ultrahigh-pressure metamorphic zone, central China: Evidence from $^{40}Ar/^{39}Ar$, fission track dating and thermobarometry, *Tectonophysics,* in press, 2000.

Ma, X.Y. (Ed.), *Lithospheric Dynamic Map of China*, Geol. Press, Beijing, 1986.

McCaffrey, R., Slip partitioning at convergent plate boundaries of SE Asia, in *Tectonic Evolution of Southeast Asia*, edited by R. Hall and D. Bundell, *Geol. Soc. Spec. Publ., 106,* 3-18, 1996.

Metcalfe, I., Pre-Cretaceous evolution of SE Asian terranes, in *Tectonic Evolution of Southeast Asia*, edited by R. Hall and D. Bundell, Geol. Soc. Spec. Pub., 106, 97-122, 1996.

Molnar, P., and P. Tapponnier, Cenozoic tectonics of Asia: The effects of a continental collision, *Science, 189,* 419-426, 1975.

Murphy, M.A., A. Yin, T.M. Harrison, S.B. Dürr, Z. Chen, F.J. Ryerson, W.S.F. Kidd, X. Wang, and X. Zhou, Did the Indo-Asian collision alone create the Tibetan plateau? *Geology, 25,* 719-722, 1997.

Okay, A.I., Petrology of a diamond and coesite-bearing metamorphic terrain: Dabie Shan, China, *Eur. J. Mineral., 5,* 659–675, 1993.

Okay, A.I., A.M.C. Sengör, and M. Satir, Tectonics of an ultrahigh-pressure metamorphic terrane: the Dabie Shan/Tongbai Shan orogen, China, *Tectonics, 12,* 1320–1334, 1993.

Oberhänsli, R., R. Schmid, L. Franz, R. Ryberg, A. Schulze, L. Ratschbacher, and B.R. Hacker, Seismic highlights structure of the Dabie ultrahigh-pressure orogen of China, *Eos Trans. AGU, 79(45),* Fall Meet. Suppl., 795, 1998.

Peltzer, G., P. Tapponnier, Z.T. Zhang, and Z.Q. Xu, Neogene and Quaternary faulting in along the Qinling Shan, *Nature, 317,* 500-505, 1985.

Petit, J.-P., F. Proust, and P. Tapponnier, Critères de sens de mouvement sur les miroirs de failles enroches non calcaires, *Bull. Soc. Géol. Fr., VII/25,* 589-608, 1983.

Ratschbacher, L., O. Merle, Ph. Davy, and P. Cobbold, Lateral extrusion in the Eastern Alps, part I, boundary conditions and experiments scaled for gravity, *Tectonics*, 10, 245-256, 1991.

Ratschbacher, L., W. Frisch, H.-G. Linzer, B. Sperner, M. Meschede, K. Decker, M. Nemcok, J. Nemcok, and R. Grygar, The Pieniny Klippen belt in the Western Carpathians of northeastern Slovakia: Structural evidence for transpression, *Tectonophysics, 226,* 471-483, 1993.

Regional Geological Survey of Anhui (R.G.S. Anhui), Regional geology of Anhui Province (in Chinese), scale 1:200,000, Geol. Publ. House, Beijing, 1975.

Regional Geological Survey of Anhui (R.G.S. Anhui), Regional geology of Anhui Province (in Chinese), scale 1:500,000, Geol. Publ. House, Beijing, 1987.

Regional Geological Survey of Henan (R.G.S. Henan), Regional geology of Henan Province (in Chinese), scale 1:500,000, Geol. Publ. House, Beijing, 1989.

Regional Geological Survey of Hubei (R.G.S. Hubei), Regional geology of Anhui Province (in Chinese), scale 1:500,000, Geol. Publ. House, Beijing, 1990.

Reischmann, T., U. Altenberger, A. Kröner, G. Zhang, Y. Sun, and Z. Yu, Mechanism and time of deformation and metamorphism of mylonitic orthogneiss from the Shagou shear zone, Qinling belt, China, *Tectonophysics, 185,* 91-109, 1990.

Roddick, J.C., The application of isochron diagrams in ^{40}Ar-^{39}Ar dating: A discussion, *Earth Planet. Sci. Lett., 41,* 233–244, 1978.

Rowley, D.B., and F. Xue, Modeling the exhumation of ultra-high pressure metamorphic assemblages: Observations from the Dabie/Tongbai region, China, *Geol. Soc. Am. Abstr.Programs, 28,* 249, 1996.

Rowley, D.B., F. Xue, R.D. Tucker, Z.X. Peng, J. Baker, and A. Davis, Ages of ultrahigh pressure metamorphism and protolith orthogneisses from the eastern Dabie Shan: U/Pb zircon geochronology, *Earth Planet. Sci. Lett., 151,* 191–203, 1997.

Schmid, J.C., L. Ratschbacher, B.R. Hacker, I. Gaitzsch, and S. Dong, How did the foreland react? Yangtze foreland fold-and-thrust belt deformation related to exhumation of the Dabie Shan ultrahigh-pressure continental crust (eastern China), *Terra Nova,* in press, 2000.

Schmid, S.M., and M. Casey, Complete fabric analysis of some commonly observed quartz c-axis patterns, in Mineral and Rock Deformation: Laboratory Studies, *Geophys. Monogr. Ser.* vol. 36, pp. 263-286, edited by B.E. Hobbs and H.C. Heard, AGU, Washington, D.C., 1986.

Schmidt, M.W., Amphibole composition in tonalite as a function of pressure: an experimental calibration of the Al-in-hornblende barometer, *Contrib. Mineral. Petrol., 110,* 304-310, 1992.

Simpson, C., and S. M. Schmid, An evaluation of criteria to deduce the sense of movement in sheared rocks, *Geol. Soc. Am. Bull.*, 94, 1281-1288, 1983.

Spang, J.H., Numerical method for dynamic analysis of calcite twin lamellae, *Geol. Soc. Am. Bull., 83,* 467-472, 1972.

Sperner, B., and L. Ratschbacher, A Turbo Pascal program package for graphical presentation and stress analysis of calcite deformation, *Z. Dtsch. Geol. Ges., 145,* 414-423, 1994.

Sperner, B., L. Ratschbacher, and R. Ott, Fault-striae analysis: A TURBO PASCAL program package for graphical presentation and reduced stress tensor calculation, *Comput. Geosci., 19,* 1361-1388, 1993.

Stokes, R.B., P.F. Lovatt Smith, and K. Soumphonphakdy, Timing of the Shan-Tai-Indochina collision: New evidence from the Pak Lay foldbelt of the Lao PDR, in *Tectonic Evolution of Southeast Asia,* edited by R. Hall and D. Bundell, *Geol. Soc. Spec. Publ., 106,* 225-232, 1996.

Tapponnier, P., and P. Molnar, Active faulting and tectonics in China, *J. Geophys. Res., 82,* 2905-2930, 1977.

Tapponnier, P., G. Peltzer, and R. Armijo, On the mechanics of the collision between India and Asia, in *Collision Tectonics,* edited by M.P. Coward and A.C. Ries, *Geol. Soc. Spec. Publ., 19,* 115-157, 1986.

Tsai, C.-H., and J.G. Liou, Eclogite facies relics and inferred ultrahigh-pressure metamorphism in the North Dabie Complex, central-eastern China, *Am. Mineral., 85,* 1-8, 2000.

Tullis, J., J.M. Christie, and D.T. Griggs, Microstructures and preferred orientations of experimentally deformed quartzites, *Geol. Soc. Amer. Bull., 84,* 297-314, 1973.

Turner, F.J., Nature and dynamic interpretation of deformation lamellae in calcite of three marbles, *Am. J. Sci., 251,* 276-298, 1953.

Wang, Y., H. Zhendouo, and Y. Zheng, The characteristics and K/Ar age of clay minerals in the fault gouges in the Yunmeng Mountains, Beijing, China, *Phys. Chem. Earth, 17,* 25-32, 1989.

Watson, M.P., A.B. Hayward, D.N. Parkinson, and Z.M. Zhang, Plate tectonic history, basin development and petroleum source rock deposition onshore China, *Mar. Pet. Geol., 4,* 205-225, 1987.

Webb, L., B.R. Hacker, L. Ratschbacher, and S.W. Dong, Structures and kinematics of exhumation: Ultrahigh-pressure rocks in the Hong'an block of the Qinling–Dabie ultrahigh-pressure orogen, E. China, *Geol. Soc. Am. Abstr. Programs, 27,* A69, 1996.

Webb, L.E., B.R. Hacker, L. Ratschbacher, and S. Dong, Thermochronologic constraints on deformation and cooling history of high- and

ultrahigh-pressure rocks in the Qinling-Dabie orogen, eastern China, *Tectonics, 18*, 621-638, 1999a.

Webb, L.E., S.A. Graham, C.L. Johnson, G. Badarch, and M.S. Hendrix, Occurrence, age, and implications of the Yagan-Onch Hayrhan metamorphic core complex, southern Mongolia, *Geology, 27*, 143-146, 1999b.

Webb, L.E., L. Ratschbacher, B.R. Hacker, and S. Dong, Mesozoic tectonics in the Hong'an and Tongbai Shan of the Qinling-Dabie collisional orogen, China: Implications for the exhumation of ultrahigh-pressure rocks, in *Paleozoic and Mesozoic Tectonic Evolution of Central Asia: From Continental Assembly to Intracontinental Deformation*, edited by M.S. Hendrix and G.A. Davis, *Spec. Pap. Geol. Soc. Am.*, in press, 2000.

Wendt, I., and C. Carl, The statistical distribution of the mean squared weighted deviation, *Chem. Geol., 86*, 275–285, 1991.

Wenk, H.-R., G. Canova, A. Molinari, and U.F. Kocks, Viscoplastic modeling of texture development in quartzite, *J. Geophys. Res., 94*, 17,895-17,906, 1989.

Wernicke, B., and G. J. Axen, On the role of isostasy in the evolution of normal fault sytems, *Geology, 16*, 848-851, 1988.

Xue, F., A. Kröner, T. Reischmann, and F. Lerch, Palaeozoic pre- and post-collision calc-alkaline magmatism in the Qinling orogenic belt, central China, as documented by zircon ages on granitoid rocks, *J. Geol. Soc. London, 153*, 409–417, 1996.

Xue, F., D.B. Rowley, R.D. Tucker, and Z.X. Peng, U-Pb zircon ages of granitoid rocks in the north Dabie complex, eastern Dabie Shan, China, *J. Geol., 105*, 744–753, 1997.

Yang, T., H. Xu, J. Zhang, and M. Song, Extension and exhumation of the Jiaonan UHP terrane, eastern China, *Tectonophysics*, in press, 2000.

Yang, Z., Y.Q. Cheng, and H.Z. Wang, *The Geology of China*, Clarendon, Oxford, England, 1986.

Yin, A., and S. Nie, An indentation model for the North and South China collision and the development of the Tanlu and Honam fault systems, eastern Asia, *Tectonics, 12*, 801–813, 1993.

Yin, A., and S. Nie, A Phanerozoic palinspastic reconstruction of China and its neighboring regions, in *The Tectonic Evolution of Asia*, edited by A. Yin and T.M. Harrison, pp. 442-485, Cambridge Univ. Press, New York, 1996.

Zhai, X., H.W. Dai, B.R. Hacker, and Z. You, Paleozoic metamorphism in the Qinling orogen, Tongbai Mountains, central China, *Geology, 26*, 371-374, 1998.

Zhang, D., and G. Sun, Emplacement age of the Tiantangzhai granite massif, Dabie Mountains and its geological significance (in Chinese), *Acta Petrol. Mineral., 6*, 31, 1990.

Zhang, R.Y., J.G. Liou, and C.H. Tsai, Petrogenesis of a high-pressure metamorphic terrane: A new tectonic interpretation for the north Dabieshan, central China. *J. Metamorph. Geol., 14*, 319-333, 1996.

Zhang, Y.Q., P. Vergely, and J.L. Mercier, Active faulting in and along the Qinling Range (China) inferred from SPOT imagery analysis and extrusion tectonics of southern China, *Tectonophysics, 243*, 69-95, 1995.

Zhang, Y.Q., J.L. Mercier, and P. Vergely, Extension in the graben systems around the Ordos (China), and its contribution to the extrusion tectonics of south China with respect to Gobi-Mongolia, *Tectonophysics, 285*, 41-75, 1998.

Zheng, X., Meso-Cenozoic volcanic rocks in east China and adjacent areas with relation to plate tectonics, *Tectonophysics, 112*, 533-550, 1985.

Zorin, Y.A., Geodynamics of the western part of the Mongologia-Okhotsk collisional belt, Trans-Baikal region (Russia) and Mongolia, *Tectonophysics, 306*, 33-56, 1999.

A. Calvert and B.R. Hacker, Department of Geology, University of California, Santa Barbara, CA 93106-9630. (hacker@geol.ucsb.edu)

D. Chateigner, Laboratoire de Physique de l'Etat Condensé, Université du Maine, av. O. Messiaen, BP535 F-72085, Le Mans Cedex 9, France.

S. Dong, Chinese Academy of Geological Sciences, No. II, Ming Zhu Xueyang Road, 100081, Beijing, People's Republic of China. (swdong@cags.com.cn)

T. Ireland and M. McWilliams, Department of Geology and Environmental Sciences, Stanford University, Stanford, CA 94305-2115. (tri@geo.stanford.de; mac@pangea.stanford.edu)

L. Ratschbacher, Institut für Geologie, Technische Universität Bergakademie Freiberg, Bernhard-von-Cotta-Str. 2, D-09596 Freiberg/Sachsen, Germany. (lothar@geo.tu-freiberg.de)

L.E. Webb, Department of Mineralogy, University of Geneva, 13 rue de Maraichers, CH-1211 Geneva 4, Switzerland. (laura.webb@terre.unige.ch)

H.-R. Wenk, Department of Geology, University of California, Berkeley, CA 94720-4767. (wenk@seismo.berkeley.edu)

(Received June 28, 1999; revised January 13, 2000;
accepted February 2, 2000.)